PAC30 Proposal: PR-06-103

Kaon Production on the Deuteron Using Polarized Photons

P. Nadel-Turoński,[1] B.L. Berman,[2] Y. Ilieva,[2] A. Tkabladze,[2]
C. Bennhold, G. Feldman, E. Munévar, A. Waluyo
The George Washington University, Washington, DC 20052

D.G. Ireland,[2] K. Livingston, B. McKinnon, D. Protopopescu
University of Glasgow, Glasgow G12 8QQ, United Kingdom

F.J. Klein, J. Santoro
The Catholic University of America, Washington, DC 20064

V. Burkert, L. Guo, J.-M. Laget, S. Stepanyan
Thomas Jefferson National Accelerator Facility, Newport News, VA 23606

E. Pasyuk
Arizona State University, Tempe, AZ 85287

I. Niculescu
James Madison University, Harrisonburg, VA 22807

S. Anefalos Pereira
Laboratori Nazionali di Frascati, Frascati I-00044, Italy

P.L. Cole, D.S. Dale, T.A. Forest
Idaho State University, Pocatello, ID 83209

P. Mattione, G. Mutchler
Rice University, Houston, TX 77005

+ The CLAS Collaboration

July 7, 2006

[1]Spokesperson and Contact Person: turonski@jlab.org
[2]Co-Spokespersons

Abstract

We propose a new CLAS experiment that will study kaon production on the deuteron using circularly and linearly polarized photon beams. The main goals are to search for "missing" baryon resonances, to improve our understanding of known ones, and to investigate the interaction of polarized hyperons with nucleons. The self-analyzing decays of Λ and Σ hyperons, combined with a 40-cm-long LD_2 target, will allow measurement of 8 polarization observables at a high rate and with a low background.

High-statistics polarization data on strange decays of N^* states photoproduced on the neutron will provide stringent constraints for the new coupled-channels calculations aimed at resolving the ambiguities inherent in previous approaches, and are especially important for resonances that have significant neutron helicity amplitudes or that do not couple strongly to pions. In particular, the large sensitivity of the $\vec{\gamma}n \to K^0\vec{\Lambda}$ channel to the much-debated "missing" $D_{13}(1900)$ resonance implies that the proposed experiment will resolve the controversy regarding its existence.

Polarization observables are also sensitive to the rescattering predictions of different $\vec{Y}-N$ interaction potentials, making the proposed experiment a natural complement to studies of bound states in hypernuclei. Understanding the rescattering is also required for a reliable interpretation of the quasifree processes. This issue will be addressed through calculations and a direct comparison of the proton channels in the proposed experiment with earlier experiments on the free proton, using linearly (g8b) and circularly (g1c) polarized photons.

We have excellent theoretical support for all aspects of the experiment. Our beam time request is for 15 days with circular and 33 days with linear photon polarization. The experiment does not require any new hardware and is flexible in terms of beam energies and polarizations, making it easy to schedule. In addition, the general nature of the setup will make it possible to use the data for the analysis of many reaction channels that are not covered by this proposal.

Contents

1 Introduction and Motivation

Understanding the structure of the nucleon is a major goal of the research program at Jefferson Lab. Measurement of the spectrum of excited baryons and their decay amplitudes is an important part of this effort, and constitutes a DOE milestone. Of particular interest is the search for "missing" resonances, predicted by the $SU(6) \times O(3)$ symmetry of constituent quark models [1], but not found experimentally. In contrast, they do not appear in di-quark models [2], which have fewer degrees of freedom. It is thus essential to establish whether the difficulty in finding the "missing" states truly reflects the presence of a strongly correlated quark pair inside the nucleon. To distinguish between the two cases, one does not need to find all of the states in the "missing" multiplets. A few clear observations from different multiplets that are incompatible with the di-quark model predictions would suffice.

In recent years, there have been several major developments in N^* physics. On the theory side, the introduction of coupled-channels analyses [3, 4, 5, 6] that include pion, eta, and kaon production shows much promise in resolving the ambiguities present when the resonance parameters are extracted from partial-wave analysis or from earlier (isobaric) models [7, 8, 9, 10, 11, 12, 13, 14]. Within the coupled-channels framework, data of reasonable quality in many channels provide a better constraint than precise data in only a few. This makes it imperative to focus not only on pion photoproduction on the proton, but also to investigate other N^* decay channels. Strange N^* decays in particular offer the possibility of finding resonances that do not couple strongly to pions [15, 16, 17]. The PAC comment to our Letter of Intent [18] states that "the proposed hyperon channels would provide a very valuable input to coupled-channel analyses that provide the best hope for ultimately discovering as yet unidentified baryon resonances predicted by quark models, or ruling out their existence".

Another new development is the possibility to measure polarization observables as well as cross sections in high-statistics experiments, which is important since the full power of

coupled-channels analyses can only be seen when there are several observables available for each channel. In an exclusive measurement with polarized photons, in addition to obtaining the beam asymmetry (Σ), the self-analyzing Λ and Σ decays give access to the hyperon recoil polarization (P), target asymmetry (T), and four polarization-transfer observables ($O_{x'}$, $O_{z'}$, $C_{x'}$, and $C_{z'}$) [19, 20, 21]. Together with the unpolarized differential cross section (σ_0), this gives 8 observables out of 16 possible. As discussed in section 2.1, however, these observables are not independent, and the remaining ones would have a limited impact on coupled-channels analyses.

We thus propose an experiment using circularly and linearly polarized photon beams and a liquid-deuterium target. This configuration has several advantages compared with HD or frozen-spin (FROST) targets.

1. A 40-cm-long, undiluted LD_2 target (6.5 g/cm^2) gives a luminosity that is more than an order of magnitude higher for a given set of running conditions than can be achieved with a 5-cm-long polarized target. This is important since target polarization is irrelevant to the measurement of σ_0, P, Σ, $O_{x'}$, $O_{z'}$, $C_{x'}$, and $C_{z'}$, and in the case of linear photon polarization, the beam current is limited by the photon tagger and not by the CLAS.

2. The systematic uncertainties are reduced by avoiding complications with deuteron tensor polarization and backgrounds from high-Z materials, such as the deuterated butanol of a frozen-spin target or the aluminum cooling wires inside the cell of an HD target, constituting up to 10% of the target mass and requiring empty-target background subtraction.

3. All hardware has been used in previous experiments and is immediately available. The experiment can begin taking data in the Fall of 2006.

The most urgent need of the coupled-channels analyses is for data on the elementary processes, *i.e.*, $\gamma n \to K^0\Lambda$, $\gamma n \to K^0\Sigma^0$, and $\gamma n \to K^+\Sigma^-$. For the Σ, the neutron channels are important in order to take full advantage of the isospin symmetry of the triplet, thereby adding significant constraints on the coupling constants of the model [22]. These channels

are, however, somewhat more complicated to interpret theoretically as they also couple to Δ^* ($I = \frac{3}{2}$) states. The Λ channel is more straightforward. At low ($W = \sqrt{s}$), only the $S_{11}(1650), P_{11}(1710)$, and $P_{13}(1720)$ N^* ($I = \frac{1}{2}$) resonances[3] contribute significantly. However, in contrast to the Σ channels, where different predictions are at least in reasonable agreement with each other, the scarce published calculations for the $K^0\Lambda$ channel span an order of magnitude in total cross section [8]. This is mainly due to the poorly understood 3^{rd} D_{13} resonance that should dominate at higher W. The only candidate for such a state in the $1.8 < W < 2.2$ GeV range that is listed by the Particle Data Group (PDG) [23] is the two-star $D_{13}(2080)$, which has been observed in pion experiments. Any other would constitute a missing resonance. Thus, when proton data from SAPHIR [24, 25] showed an enhancement at $W \sim 1.9$ GeV, it was identified by Bennhold *et al.* as the missing $D_{13}(1900)$ resonance [26, 27]. This structure was also seen in later CLAS experiments [28, 29].

A 3^{rd} D_{13} state around 1900 MeV can, however, only be called a "missing" N^* resonance if there were a 4^{th} one at 2080 MeV. The latest GW coupled-channels results, based on proton data, allow for a 4^{th} resonance, but do not confirm it. The data from this proposed experiment should settle this issue. The outcome is important since the GW analysis demonstrates that the current proton data can be well described using all resonances with a PDG rating of two stars or more, but no one-star or "missing" resonances. This assumes, however, that the $D_{13}(1900)$ and the previously reported $D_{13}(2080)$ are the same resonance. Should both be found, it would provide strong support for the constituent-quark models. The predictions of these models, and the whole issue of the "missing" N^* resonances, have recently been called into question by the coupled-channels analyses of both the GW and Giessen groups. In particular, the $P_{13}(1900)$ would be expected to play an important role in $K\Lambda$ photoproduction. The analysis of the proton data also rule out any 3^{rd} or 4^{th} P_{13} N^* resonance. Yet, the P_{13} channel is the one where most quark models have predicted at least 3 or 4 extra states beyond the $P_{13}(1720)$ and $P_{13}(1900)$. Likewise, neither analysis found a

[3]notation: $L_{2I,2J}(\sqrt{s})$

3^{rd} S_{11} or P_{11} resonances. By resolving the $D_{13}(1900)$ / $D_{13}(2080)$ controversy, the proposed experiment thus has the potential to be an important step towards ruling out the existence of "missing" N^* resonances, and at the same time to firmly establish a two-star resonance.

In the comment to our Letter of Intent, the PAC also points out that while "the emphasis of the proposed experiment is hyperon production from the neutron, with the goal of searching for *missing resonances* that couple weakly to pion channels. In fact, both neutron and proton data are essential to the extraction of photo-couplings of even existing N^* resonances."

Going beyond the elementary amplitudes, substantial partial N^* decay widths are predicted for strange channels where either the kaon or the hyperon is in an excited state [17]. These channels will eventually have to be included in a complete model, but currently photoproduction data on the proton are scarce and there are no neutron data. We hope to remedy this by measuring N^* decays into low-lying K^*Y and KY^* final states. This will, of course, make it possible to study hyperon resonances as well. A point of common interest is that some N^* resonances have been suggested to be "molecular" $\bar{K}N$ bound states. This is also the case for the spin-$\frac{1}{2}$ $\Lambda(1405)$, which is predicted by potential models to have the same mass as its spin-$\frac{3}{2}$ partner, the $\Lambda(1520)$. If the mass difference indeed were due to a "molecular" structure, this would also have implications for the understanding of N^* states.

Studying the quasifree reactions on the neutron is more complicated than for the proton due to the initial- and final-state interactions in the target deuteron. These have to be understood in order to select the best kinematics. The investigation such effects thus becomes an important part of the proposed experiment. This will be achieved by directly comparing our results for the proton channels with those on the free proton from the recent g8b experiment, which was performed using the same equipment under nearly identical conditions, as well as with the results of the circularly polarized g1c experiment. Once the final-state interactions in the proton channels are well understood, the same models can be applied to the neutron.

Moreover, final-state interactions also offer new physics opportunities [30, 31, 32]. One example is the search for color transparency, which prompted Laget to develop a new rescattering model [33]. His approach has recently allowed us to make the first direct observation of $\Sigma^-(1385)$ scattering on the proton [34]. We also intend to investigate the less exotic, but perhaps more important, $\vec{\Lambda} - N$ interaction, where a recent calculation shows the sensitivity of polarization observables to the predictions of various modern Λ - N potentials [35]. $\vec{\Lambda} - N$ scattering would thus be a natural complement to hypernuclear experiments. $K - N$ rescattering will, of course, be measured as well.

2 Theory

2.1 Polarization observables

This section lists the polarization observables for kaon photoproduction and discusses some of their properties. A more detailed treatment can be found in Refs [19], [21], and [36].

In total, 16 polarization observables can be defined. They can be divided into two groups: single- and double-polarization observables. In contrast to electroproduction, there are no triple-polarization observables (requiring beam, target, and recoil polarization) in kaon photoproduction.

Single	σ_0	P	Σ	T
Beam-Recoil	$C_{x'}$	$C_{z'}$	$O_{x'}$	$O_{z'}$
Target-Recoil	$T_{x'}$	$T_{z'}$	$L_{x'}$	$L_{z'}$
Beam-Target	E	F	G	H
Beam-Target-Recoil	——	none	——	

Table 1: Polarization observables in kaon photoproduction.

The recoil observables can be measured by taking advantage of the fact that the Λ and Σ hyperons are self-analyzing. It is important to note that not only can all of the first eight observables be measured without a polarized target but, with the exception of the target asymmetry T, they do not in any way benefit from one. The observables are not independent, but related by a set of inequalities and six simple equations [36].

$$E^2 + F^2 + G^2 + H^2 = 1 + P^2 - \Sigma^2 - T^2, \quad (1)$$

$$FG - EH = P - \Sigma T, \quad (2)$$

$$T_{x'}^2 + T_{z'}^2 + L_{x'}^2 + L_{z'}^2 = 1 + \Sigma^2 - P^2 - T^2, \quad (3)$$

$$T_{x'}L_{z'} - T_{z'}L_{x'} = \Sigma - PT, \quad (4)$$

$$C_{x'}^2 + C_{z'}^2 + O_{x'}^2 + O_{z'}^2 = 1 + T^2 - P^2 - \Sigma^2, \quad (5)$$

$$C_{z'}O_{x'} - C_{x'}O_{z'} = T - P\Sigma. \quad (6)$$

For example, if the recoil polarization P, the beam asymmetry Σ, and the four beam-recoil observables are known, one can calculate T. In a similar way, the target-recoil and beam-target observables are constrained by the single-polarization observables, which can be measured with smaller uncertainties. Since the beam polarization is usually much higher and better known than the target polarization, the beam-recoil observables can be obtained with significantly higher accuracy than the target-recoil ones. Of course, if one is not restricted to using a polarized target, the first 8 observables can be measured with a luminosity that is an order of magnitude higher for equivalent running conditions, and with smaller systematic uncertainties. For coupled-channels calculations, lower uncertainties and better kinematic coverage are the most important. This is why we decided to use a polarized beam and a thick LD_2 target. The eight observables can then be extracted from the expression for the polarized cross section [21, 36].

$$\begin{aligned} \frac{d\sigma}{d\Omega} = \sigma_0 \{ & 1 - P_{lin}\Sigma \cos 2\varphi \\ & + P_{x'} \left(-P_{lin}O_{x'} \sin 2\varphi - P_{\odot}C_{x'}\right) \\ & - P_{y'} \left(-P + P_{lin}T \cos 2\varphi\right) \\ & - P_{z'} \left(P_{lin}O_{z'} \sin 2\varphi + P_{\odot}C_{z'}\right)\} \end{aligned} \quad (7)$$

Here P_{lin} and $P_{\odot}$ are respectively the degrees of transverse linear and right-handed circular photon polarization, and φ is the angle between the photon polarization vector and the reaction plane. The orientations of the primed axes are shown in Fig. 1. In the case of circular polarization, the asymmetries for $C_{x'}$ and $C_{z'}$ are constructed using the beam helicity information rather than the φ dependence [37]. The target asymmetry (T) is the most problematic, since it has the same φ dependence as Σ and the same $P_{y'}$ ($= \alpha \cos\Theta_{y'}$) depen-

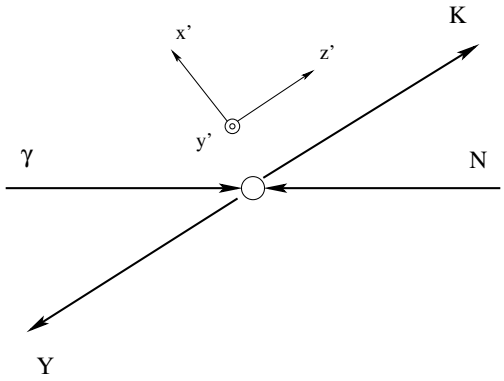

Figure 1: Definition of the primed coordinate system. The angle φ between the photon polarization vector and the reaction plane is shown in Fig. 27 below.

dence as P. Thus, the uncertainties from Σ and P will propagate into the determination of T.

In order to perform a complete measurement determining all amplitudes up to an overall phase and eliminate the discrete ambiguities, two additional double-polarization observables would be required [19]. This is, however, a very challenging task, considering that full model independence requires full kinematic coverage with good uncertainties. Thus, although our primary goal is to provide precise data for coupled-channels analyses, this proposed experiment will be of great benefit for such an endeavor. The better statistical and systematic uncertainties that can be reached over a wider kinematic range for σ_0, P, Σ, $O_{x'}$, $O_{z'}$, $C_{x'}$, and $C_{z'}$, will significantly reduce the model dependence.

2.2 Coupled-channels calculations

Baryon resonances are identified by their quantum numbers, such as orbital angular momentum, spin, isospin, and parity. These quantum numbers determine the partial waves responsible for their excitation. Baryon resonances are categorized by their appearance in a given partial wave. An example of such a sequence are the $D_{13}(1520)$, $D_{13}(1700)$, and $D_{13}(2080)$ resonances listed by the Particle Data Group (PDG) [23]. For the first resonance in each partial wave, different analyses usually agree to within 20% regarding properties

such as mass, decay width, and helicity amplitudes. In contrast, only rough agreement is found for the mass of the second resonance, and in most cases there is a wide variation in the extracted decay widths and helicity amplitudes. In most partial waves, the situation is even worse for the third resonance.

As part of the effort to investigate the baryon resonances, Waluyo and Bennhold have made significant progress in developing a new coupled-channels "Chiral-Symmetry-Inspired" (CSI) model [6]. It is based on the work by Feuster and Mosel [38], but the driving terms of the original model, which are defined through traditional effective Lagrangians, have been replaced by ones with new background and resonance parts. The new background is obtained from a potential that takes into account the requirements of $SU(3)$ chiral dynamics. This involves expanding the chiral Lagrangian to a given order, and includes contact terms permitted to that order. At the same time, the resonance contributions have been updated using the modern covariant resonance Lagrangians derived by Pascalutsa [39]. This fixes the incorrect spin degree of freedom and discards the ambiguous off-shell terms inherent in the old Rarita-Schwinger types of Lagrangians, which are still used in other analyses.

Having these modifications in place, new background amplitudes are reconstructed from the standard s, t, and u Born terms, σ and a_0 scalar-meson resonances, ρ, ω, and K^* vector-meson resonances, as well as Weinberg-Tomozawa and higher-order chiral contact terms. The new resonance amplitudes are constructed from the s- and u-channel pole diagrams where spin-$\frac{1}{2}$, $\frac{3}{2}$, and $\frac{5}{2}$ baryon resonances propagate in the intermediate states. This is the first coupled-channels model where baryon resonances are included using modern hadronic and electromagnetic interaction Lagrangians.

The CSI model includes five asymptotic states of πN, $2\pi N$, ηN, $K\Lambda$, and $K\Sigma$. The 2π system is for the moment approximated using the scalar-isovector ζ particle. The Bethe-Salpeter equation is solved in the K-matrix approximation. To ensure that the CSI model is gauge-invariant, the gauge-invariance restoration scheme of Davidson and Workman [40] has been implemented. The model is used to investigate baryon resonance states through meson

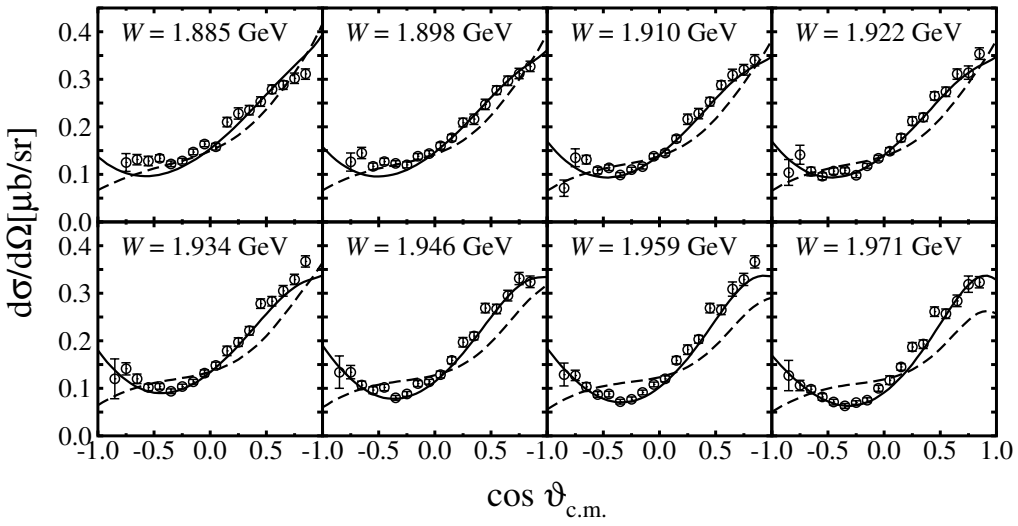

Figure 2: Differential cross sections for $\gamma p \to K^+\Lambda$ at high W, given as function of the kaon angle in the cm frame. The solid and dashed lines show, respectively, the calculation using the CSI model with and without the $D_{13}(1900)$ resonance. Data are from McNabb *et al.* [28].

hadro- and photoproduction reactions, and is currently implemented in the energy region of $W < 2$ GeV, but should soon be extended up to 2.3 GeV. As input, it uses the most recent high-quality photoproduction data provided by the CLAS collaboration [28, 29, 41]. Fits to the $\gamma p \to K^+\Lambda$ differential cross-section data [28, 42] at high W are shown in Fig. 2. Additional proton results can be found in the Appendix.

From a theoretical point of view, polarization observables provide an advantage over the differential cross section for projecting out the role of a baryon resonance in a specific channel, since they contain interferences of electromagnetic multipoles. For example, the double-polarization observable $O_{x'}$ can be written in terms of the helicity amplitudes for meson photoproduction:

$$O_{x'} = \frac{\mathrm{Im}[H_1^* H_2 - H_3^* H_4]}{\frac{1}{2}(|H_1|^2 + |H_2|^2 + |H_3|^2 + |H_4|^2)}, \tag{8}$$

The helicity amplitudes can then be expressed in terms of CGLN amplitudes [21, 43]:

$$\begin{aligned} H_1 &= \frac{-1}{\sqrt{2}}\sin\theta(F_3 + F_4\cos\theta), \\ H_2 &= \frac{-1}{\sqrt{2}}(2F_1 - 2F_2\cos\theta + F_4\sin^2\theta), \\ H_3 &= \frac{-1}{\sqrt{2}}F_4\sin^2\theta, \\ H_4 &= \frac{1}{\sqrt{2}}(2F_2 + F_3 + F_4\cos\theta). \end{aligned} \tag{9}$$

The CGLN amplitudes can, in turn, be expanded in terms of electromagnetic multipoles:

$$\begin{aligned} F_1 &= \sum_{l\leq 0}\{(M_{l+} + E_{l+})P'_{l+1} + [(l+1)M_{l-} + E_{l-}]P'_{l-1}\}, \\ F_2 &= \sum_{l\leq 1}[(l+1)M_{l+} + lE_{l-}]P'_l, \\ F_3 &= \sum_{l\leq 1}[(E_{l+} - M_{l+})P''_{l+1} + (E_{l-} + M_{l-}]P''_{l-1}]\}, \\ F_4 &= \sum_{l\leq 2}(M_{l+} - E_{l+} - M_{l-} - E_{l-})P''_l. \end{aligned} \tag{10}$$

In the energy range of $1.8 < W < 2.0$ GeV, four possible missing-resonance states were investigated using the CSI model and the available proton data. They are the S_{11}, P_{11}, P_{13}, and D_{13}. Each would constitute the third state in its respective partial wave. No evidence was seen for the first three. A possible D_{13} state was found with a mass of 1961 MeV and a total width of 313 MeV. Its properties, and a comparison with the values from other analyses, are shown in Tables 2 and 3. Should it be confirmed, the $D_{13}(1900)$ missing resonance would fall into the PDG [23] 2-star category, where a resonance state is found in different analyses with rough agreement of mass values, but with disagreement with respect to other properties, such as decay width or helicity amplitudes. Until the neutron data are available, all these parameters have to be regarded as preliminary.

Polarization observables are also important because the extracted resonance parameters

$D_{13}(1900)$	Mass	Γ_{tot}	$\beta_{\pi N}$	$\beta_{2\pi N}$	$\beta_{\eta N}$	$\beta_{K\Lambda}$	$\beta_{K\Sigma}$
CSI model	1961	313	7	48	0.5	15	31
Penner and Mosel [3]	1946(1)	859(7)	12(2)	59(8)	7(2)	0.2(0.2)	0.7(0.4)
Vrana *et al.* [44]	1940	412	10	75	14	0	-

Table 2: Preliminary properties of the $D_{13}(1900)$ resonance extracted from proton data. The mass and total width are given in MeV, and the decay ratios β are in %. Penner and Mosel also find some branching into ωN.

depend on the choice of hadronic form factors [38], which are necessary to reproduce the high-energy part of the data even in a single-channel analysis. Where there are no data, this translates into a systematic uncertainty in the predicted cross section. The CSI model considers three functional forms that (i) are only functions of q^2, (ii) have no poles on the real axis, and (iii) for which $F(m^2) = 1$ at $q^2 = m^2$ [6]. While various functional forms can reproduce the cross section, addition observables will restrict the choice, making the extracted resonance parameters more reliable.

Until now, the evidence for the $D_{13}(1900)$ comes from the available $K\Lambda$ and $K\Sigma$ photoproduction differential cross-section data on the proton [24, 28, 42]. Although current coupled-channels analyses [3, 6] give a fairly good description of the proton data, most of the extracted properties of the missing $D_{13}(1900)$ resonance vary widely. New data are thus needed to provide more stringent constraints for the extraction of its properties or to rule out its existence. A careful look at the helicity amplitudes of the $D_{13}(1900)$ resonance, shown in Table 3, suggests which new data sets are needed. The values of $A^n_{\frac{1}{2}}$ and $A^n_{\frac{3}{2}}$ are large,

$D_{13}(1900)$	$A^p_{1/2}$	$A^p_{3/2}$	$A^n_{1/2}$	$A^n_{3/2}$
CSI model	+21	-1	+130	+123
Penner and Mosel [3]	+12	-10	+23	-9

Table 3: Preliminary electromagnetic helicity amplitudes, in 10^{-3} GeV$^{-1/2}$, for the $D_{13}(1900)$ resonance extracted from proton data. The superscript p or n indicates the proton or neutron helicity amplitude.

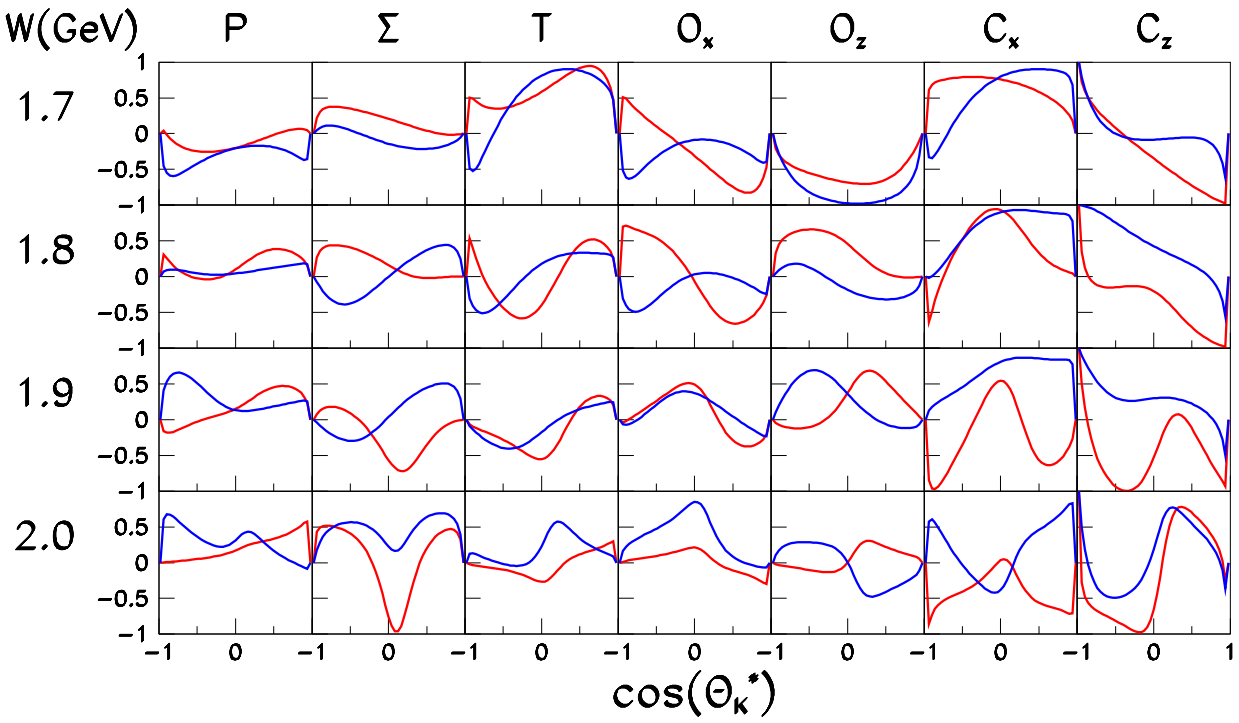

Figure 3: The predictions of the CSI model for the seven observables in the $\vec{\gamma}n \to K^0\Lambda$ channel that will be measured in this proposed experiment in addition to the unpolarized cross section. The red and blue curves are the predictions with and without the missing $D_{13}(1900)$ resonance, respectively.

indicating that a large sensitivity to the $D_{13}(1900)$ is present in the neutron channel of $K\Lambda$ photoproduction, namely, the $\vec{\gamma}n \to K^0\Lambda$ reaction.

The Σ channels are not sensitive to the D_{13} resonances, but in order to take full advantage of the isospin symmetry of the Σ, data are needed for $K\Sigma^-$ as well as for $K\Sigma^+$ and $K\Sigma^0$. The first of these can be studied only with a neutron target. The symmetry is important since, in contrast to the Λ, the Σ channels in general, and the Σ^0 in particular, also couple to Δ^* $(I = \frac{3}{2})$ states. The data will thus allow a reliable measurement of N^* $(I = \frac{1}{2})$ resonances other than the $S_{11}(1650), P_{11}(1710)$, and $P_{13}(1720)$, which dominate at low W.

The current predictions of the CSI model for the observables in our beam-recoil polarization experiment for the $K^0\Lambda$ reaction are shown in Fig. 3, with and without the $D_{13}(1900)$. The predictions for the $K^+\Sigma^-$ channel are shown in Fig. 4. The full results of the CSI model

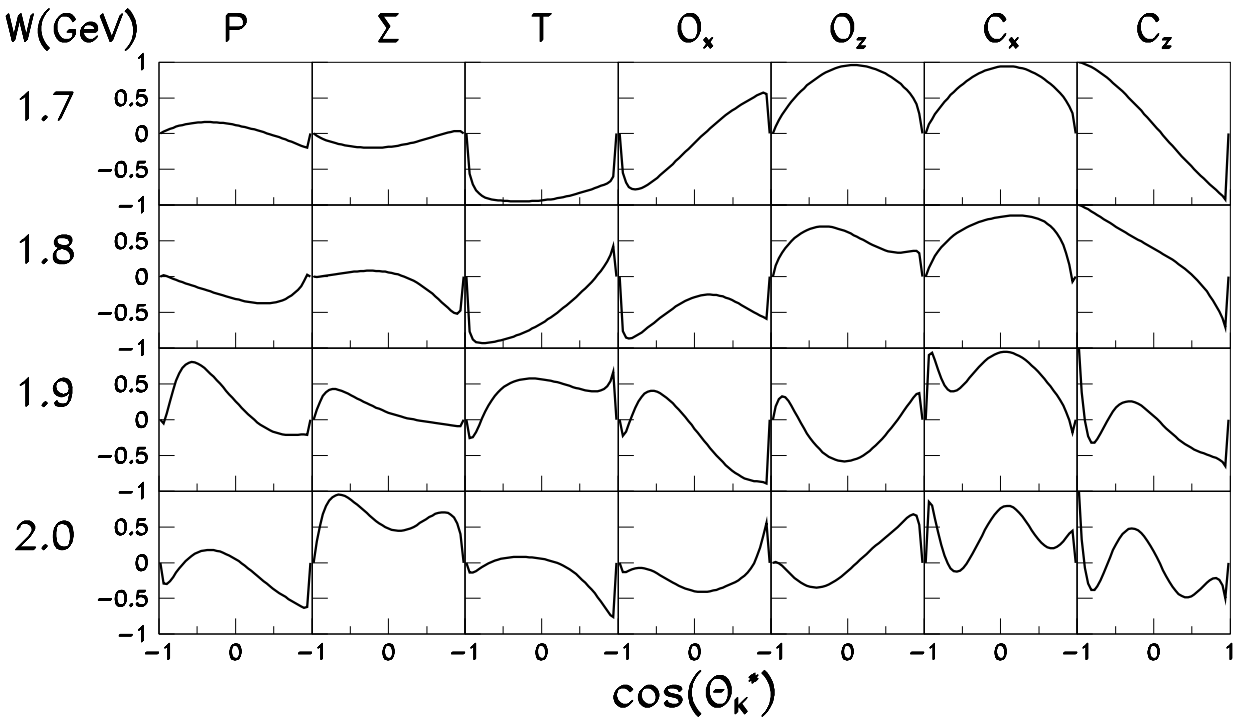

Figure 4: The predictions of the CSI model for the seven observables in the $\vec{\gamma}n \to K^+\Sigma^-$ channel that will be measured in the proposed experiment in addition to this unpolarized cross section.

for both the Λ and Σ channels have been incorporated into a new event generator [45] for calculating the experimental acceptances..

From the point of view of coupled-channels analyses, a measurement of the remaining independent observables (see section 2.1) would have a limited impact unless the uncertainties were comparable in all kinematic bins $(E_\gamma, cos(\theta_K^{cm}))$ with those that can be obtained using polarized photon beams and the hyperon recoil polarization.

It is important to note the analysis of the $K^0\Lambda$ channel will not be a simple comparison of the data with the predictions with and without the $D_{13}(1900)$ resonance. Instead, all of the 520 data points measured for each channel in the proposed experiment (at least 400 of which will have small uncertainties for $\vec{\gamma}n \to K^0\Lambda$) will be used to make a new global fit to all channels. This fit will be strongly constrained, allowing extraction of the resonance parameters for, among others, the $D_{13}(1900)$ and $D_{13}(2080)$ resonances with a

high confidence level.

It is also important to stress that the sensitivity of polarization observables, and their importance in unambiguously projecting out the properties of known, and possibly missing, resonances, does not depend on the details of the CSI model. In the analysis of the data we will also use models from two other theoretical groups with whom we have strong collaborative links: Gent (Belgium) and KVI, Groningen (The Netherlands).

The Gent model, developed by Janssen *et al.* [11, 12, 13], is an effective field theory which takes into account contributing tree-level diagrams only. In addition to the s-channel resonance diagrams of interest, t-channel K* and Y exchange is included as well as standard Born terms. The advantage of a tree-level approach lies in its simplicity; the number of parameters required to be determined by fits to the data is generally much smaller than for coupled-channels approaches. Despite the reduction in fitting parameters, however, it has been shown [46] that the interpretation of current data using this approach is plagued by ambiguities. It might nevertheless be argued that, with uncertainty surrounding the choice of gauge restoration scheme and form factor parametrization, it may be useful to also compare the data with a simpler model describing its gross features. It is, however, clear that coupled-channels effects are important, and will have to be taken into account in a full interpretation of data. For instance, Chang *et al.* [47] showed that the contribution of an intermediate πN channel to $\gamma p \to KY$ cross-sections is of the order of 20%.

Corthals *et al.* [48] have further developed the Gent model by including a new method of constraining the background in $\gamma p \to KY$ reactions. High-energy data ($E_\gamma > 4$ GeV) are used to fix the parameters of the background processes, and a Regge-model approach is used to extrapolate this background to the resonance region. The general shape of the cross section as a function of photon energy is quite well described by this Regge model, as demonstrated earlier by Guidal *et al.* [49]. But by definition, the Regge model cannot account for any features which appear as strong s-channel resonances, and therefore a limited number of s-channel resonances are also included. This gives rise to a Regge-Plus-Resonance

(RPR) model. It is argued in [48] that even though the notion of duality might suggest a problem with double counting in the kinematics of the resonance region, this is not likely to be a big problem. At any rate, this new method of dealing with the background has many advantages over previous attempts that relied on heavy interference with Born terms, and were not applicable at photon energies above 2 GeV. It also reduces the number of free parameters to a handful of coupling constants for the s-channel resonances. An additional feature of the Gent model is that it can be used to calculate strangeness electroproduction.

At KVI, Usov and Scholten [50] have recently developed a coupled-channels model for strangeness photoproduction. This model is similar to the CSI model in that a K matrix with an effective Lagrangian is used to preserve many symmetries of a full-field theoretical approach, while accounting for coupled channels. The final states included in this model are $K\Lambda$, $K\Sigma$, ϕN, ηN, ρN, and γN. Coupling among these channels is taken into account explicitly in the K matrix, and coupling to other channels is modeled by an explicit dissipative part in the kernel. In Ref. [50] it is asserted that the effects of channel coupling are not just a smooth change of the energy dependence of the cross section, but that they can also give rise to structures in the cross section that might otherwise be incorrectly attributed to resonances. Consequently, a more thorough measurement of a range of observables in several isospin channels, such as the one that we are proposing, will be essential in resolving whether additional resonances are required to explain the data.

The KVI group is currently working on a data-fitting scheme similar to that applied to the Gent model [46]. Thus, by the time the data taken by the measurements we propose are ready for interpretation, we will be able to perform a quantitative comparison among the various models, thereby strengthening any conclusions we may be able to draw.

Both the Gent and the KVI theory groups also have a strong tradition in nuclear-structure physics and are thus well placed to bring their experience to bear on the problem of dealing with rescattering effects in the deuteron as well.

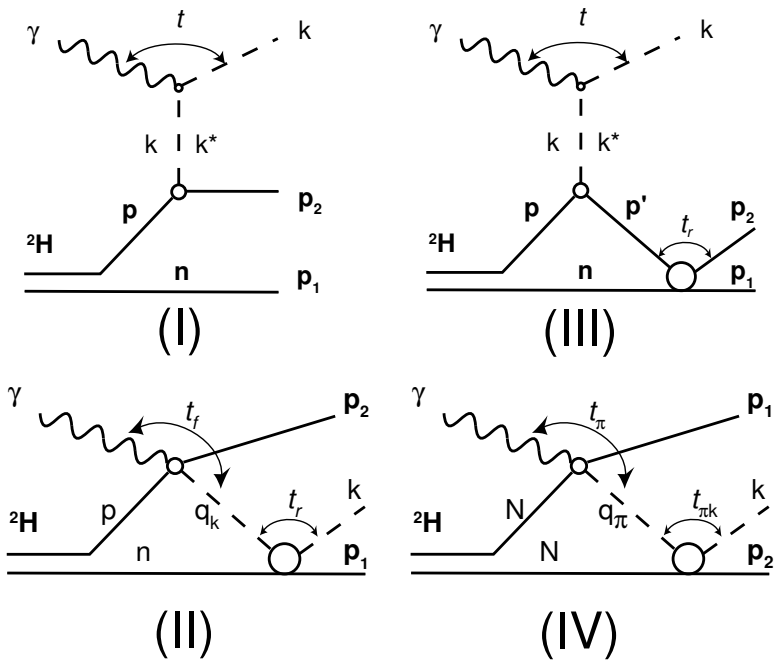

Figure 5: The relevant graphs in the $\gamma d \to nK^+\Lambda$ reaction. I: Quasifree kaon photoproduction. II: Kaon-nucleon rescattering. III: Lambda-nucleon rescattering. IV: Intermediate-state interactions.

2.3 Rescattering

The dominant processes in the photoproduction of kaons from the deuteron are shown in Fig. 5. The detailed expressions for the corresponding amplitudes are given in Ref. [33]. Here, we give only a brief sketch of the underlying physics and an update of the choice of the parametrization of the elementary amplitudes at lower energies. As an example, we consider the $\gamma d \to nK^+\Lambda$ reaction, but the extension to the $\gamma d \to pK^0\Lambda$ or $\gamma d \to nK^+\Lambda^*(1520)$ channels, as well as the Σ production channels, is straightforward. Event generators for both $K^+\Lambda$ and $K^0\Lambda$ are ready.

Graph I represents the quasifree production of the K^+ on the proton, the neutron being a spectator. It dominates at low values of the spectator neutron momentum p_n, where the cross section takes the simple form [33, 51]:

$$\frac{d\sigma}{d\vec{p_n}d\Omega_k} = (1 + \beta_n \cos\theta_n)\rho(|\vec{p_n}|)\frac{d\sigma}{d\Omega_k}(\gamma p \to \Lambda K^+) \tag{11}$$

where $\beta_n = p_n/E_n$ and θ_n are the velocity and the angle of the spectator nucleon. This is nothing but the relation between the yield and the elementary cross section for the production of a kaon on a nucleon which moves with the velocity $-\vec{\beta_n}$. The number of target nucleons is $\rho(|\vec{p_n}|)d\vec{p_n}$, where $\rho(|\vec{p_n}|)$ is the momentum distribution of the proton in the deuteron (which we take from the Paris potential), while $(1 + \beta_n \cos\theta_n)$ is the flux of photons seen by the moving target nucleon.

When the neutron momentum increases, its momentum distribution decreases very quickly, and kaon-nucleon (graph II) as well as lambda-nucleon (graph III) rescatterings become dominant above $p_n \sim 300$ MeV/c. Since the available energy in each rescattering vertex is larger than the sum of the masses of the two particles which rescatter, both can be on-shell in the intermediate state. This induces a logarithmic singularity in each rescattering integral [33, 51]. Its effect is maximal on the cross section when the minimum momentum p_{min} of the spectator nucleon in the loop, for which the two particles which rescatter are on-shell, vanishes.

At the top of the corresponding peaks, the physical picture is the following. The Λ, or the K, is produced on a nucleon at rest and rescatters on the second nucleon, also at rest in the deuteron, which then recoils with the observed momentum p_n. Here, the rescattering amplitude is on solid ground, since it depends on on-shell elementary matrix elements and relies on the low-momentum components of the deuteron wave function. This is a good place to study the interactions with nucleons of short-lived particles (such as the various hyperons) or to look for elusive narrow resonant states (*e.g.*, in the K^+n channel).

Graph IV represents the case where the kaon is produced by the rescattering of an intermediate pion. This graph has not yet been included in the model, but will contribute to the rescattering cross section shown in Fig. 16 in section 3.4. Experimentally, it can be studied using the same minimum-momentum approach as graphs II and III.

Figure 6 shows various observables which emphasize the kaon-nucleon rescattering sector. The endpoint energy of the real photon beam has been set to $E_\gamma = 2$ GeV. The panels show

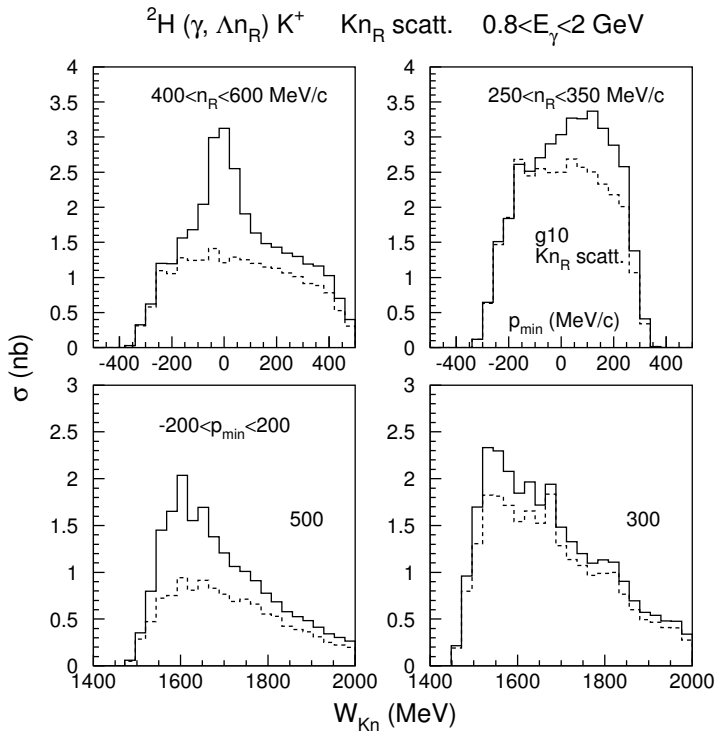

Figure 6: The kaon-nucleon rescattering sector. The solid line is the full calculation and the dashed line is the quasifree contribution. The upper plots show the minimum initial momentum (p_{min}) of the spectator nucleon for two different cuts on the final momentum. The lower plots show W_{Kn} for final spectator momenta (n_R) of 500 and 300 MeV, with a 400-MeV cut around zero for its initial minimum momentum.

cross sections integrated over the various bins within the CLAS fiducial acceptance. The top panels show the distribution of the minimum momentum $p_{min}(nK)$ of the spectator neutron, in the kaon-nucleon scattering loop, for which the pion can propagate on-shell. On the left, the cut $400 < n_R < 600$ MeV/c has been applied on the momentum p_n of the slow nucleon: the kaon-nucleon rescattering peak clearly appears at $p_{min} = 0$. On the right, the cut $250 < n_R < 350$ MeV/c has been applied; rescattering effects are small here, and the shape of the distribution reflects the kinematics and the detector acceptance. This is a good reference point that emphasizes the quasifree process. A further cut -200 < $p_{min}(nK)$ < 200 MeV/c has been applied in the bottom parts of Fig. 6, which emphasize kaon-nucleon rescattering. The distribution of the mass W_{Kn} of the K^+n system is plotted on the left for the high-recoil-momentum and on the right for the low-recoil-momentum bands.

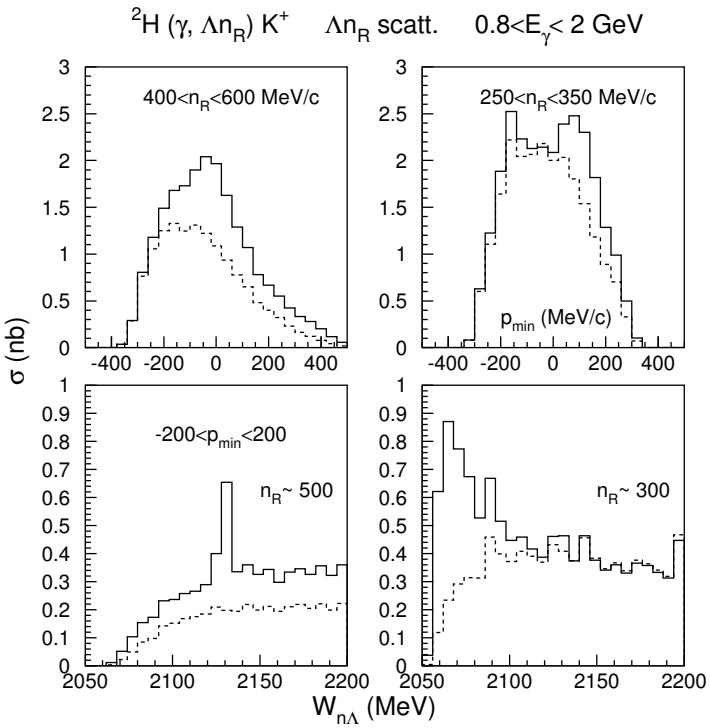

Figure 7: The lambda-nucleon rescattering sector. The solid line is the full calculation and the dashed line is the quasifree contribution. The upper plots show the minimum initial momentum (p_{min}) of the spectator nucleon for two different cuts on the final momentum. The lower plots show W_{Kn} for final spectator momenta (n_R) of 500 and 300 MeV, with a 400-MeV cut around zero for its initial minimum momentum.

Figure 7 shows the same observables in the Λ-n rescattering sector. Now, the minimum momentum $p_{min}(n\Lambda)$ is the lowest value of the momentum of the spectator neutron for which the Λ can propagate on-shell in the Λ-N scattering loop. For the low-recoil-momentum ($\sim$ 300 MeV/c) band (bottom right), strong S-wave rescattering enhances the distribution of the mass $W_{\Lambda n}$ of the Λn system near the Λ production threshold, but the quasifree process contributes less for recoil momenta above $\sim$ 300 MeV/c. For the high-recoil-momentum ($\sim$ 500 MeV/c) band (bottom left), the CLAS acceptance suppresses the kinematical region near the Λ production threshold, but the contribution from the quasifree process is nevertheless smaller here. The cusp in the Λn scattering amplitude clearly appears at the Σ production threshold; it comes from the coupling between the Λ and the Σ channels.

Contrary to Ref. [33], which contains high-energy descriptions of the elementary scat-

tering amplitudes, we will here focus on the low-energy phase-shift expansions discussed in Ref. [52]. This approach has already led to a good description of kaon production in pp scattering [53, 54], but was not able to disentangle the Λ and Σ channels. This becomes possible with the CLAS, which opens up the possibility to map out (for the first time) the hyperon-nucleon amplitudes in the vicinity of the Σ threshold and above. This will provide a strong constraint on the models that try to describe the interaction between hadrons.

In Fig. 6, Λn rescattering gives a contribution under the K^+n rescattering peak. In a similar way, K^+n rescattering gives a contribution under the Λn rescattering peak shown in Fig. 7. These contaminations can be removed by cutting out the overlapping region in the joint distribution of the rescattering singularities, which is shown in Fig. 8.

In all of these histograms, the model has been folded with the CLAS geometrical acceptance and physical cuts have been performed according to the method that is described in

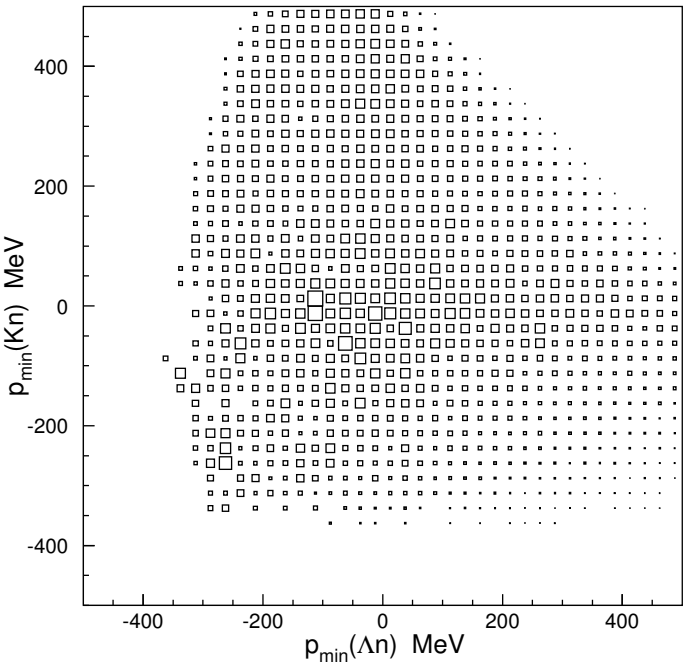

Figure 8: The joint distributions of the logarithmic singularities for K^+n and Λn rescattering. The K-n and Λ-n projections, for different cuts on the final spectator momentum, are shown in Figs. 6 and 7.

Ref. [33]. Only the geometrical fiducial cut of the kaon has been taken into account. This is the most important cut since it defines the momentum transfer between the photon and the kaon. Neither the in-flight decay of the kaon nor the $\Lambda \to p\pi^-$ decay have been taken into account here; they can be handled by the Monte Carlo simulation, and are expected to lead to an almost constant overall reduction factor.

The new event generators allow the model to be folded with the full acceptance and efficiency of the CLAS. Besides normalization effects, the mass resolution effects will be important in trying to sort out the narrow structure of the cusp at the Σ production threshold.

3 Experiment

3.1 Previous experiments

There are currently no published data for the elementary strangeness photoproduction channels on the deuteron. This section will therefore only mention a few other experiments that show a relevant degree of similarity. More importantly, it illustrates why CEBAF/CLAS *before* the 12-GeV upgrade is the only place in the world where the proposed experiment can be performed.

For the proton there are several published results, notably by the SAPHIR [24, 25] and CLAS [28, 29, 37, 42, 55] collaborations - the latter using the g1c data set. The published total cross section are shown in Fig. 9, and the $C_{x'}$ and $C_{z'}$ polarization transfer observables in Fig. 10. Figure 11 shows beam asymmetry measurements from g8a, which was the commissioning experiment for the coherent bremsstrahlung facility in Hall B. The program on the proton continues at JLab with the g8b experiment, currently in the last stages of calibration, and the FROST program.

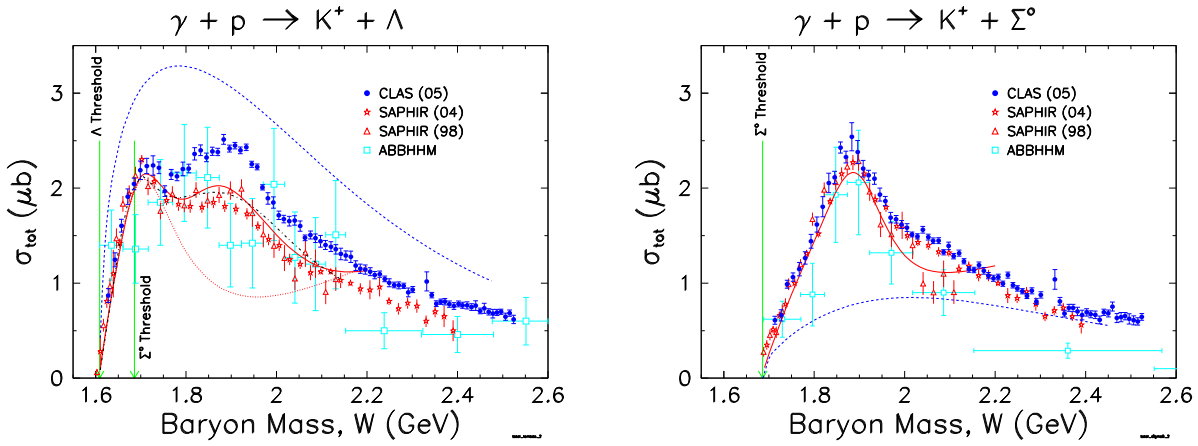

Figure 9: Total cross sections for Λ and Σ^0 photoproduction on the proton [29]. The enhancement near $W = 1.9$ GeV that has been identified with the missing $D_{13}(1900)$ resonance can be seen clearly in the left panel.

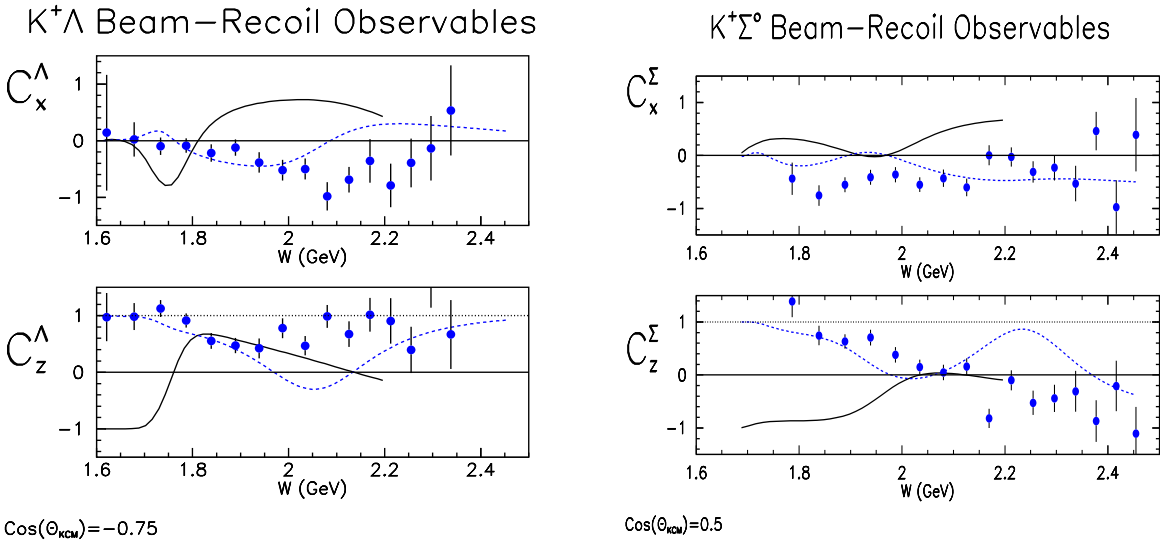

Figure 10: Polarization-transfer observables have been measured in CLAS for both the Λ and Σ^0 channels on the proton using a circularly polarized photon beam [37].

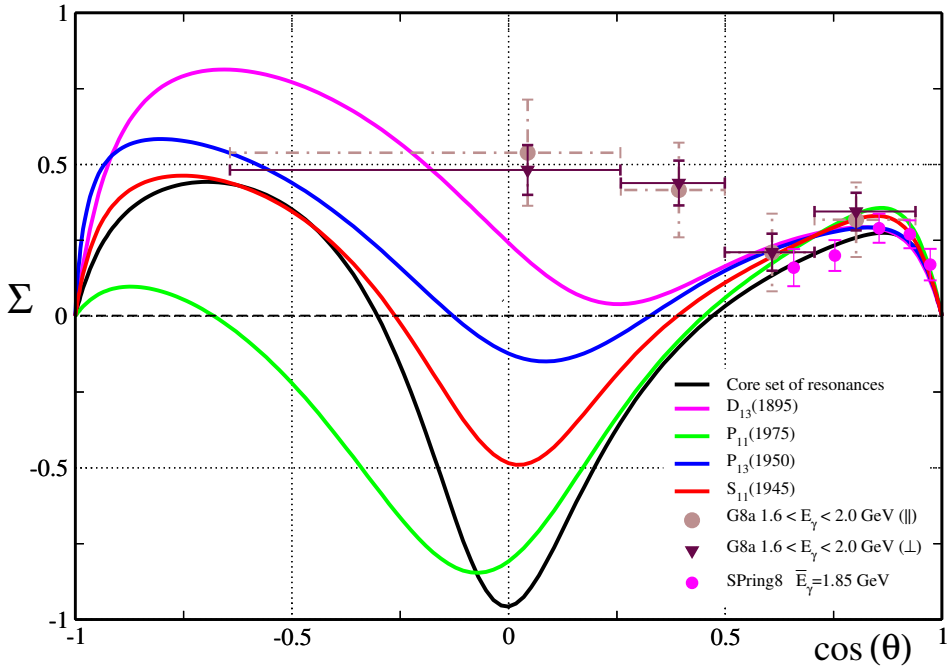

Figure 11: Beam asymmetry Σ for the $\gamma p \to K^+\Lambda$ channel. The figure illustrates the importance of large acceptance. Even the rather poor data from the commissioning of the coherent bremsstrahlung facility in Hall B (g8a) are more important for constraining models than the current data from Spring-8. Calculations are by Ireland, Janssen, and Ryckebusch [46].

3.1.1 Deuteron experiments at Jefferson Lab

There are two real-photon data sets from CLAS using a deuteron target: g2 and g10. Another, eg3, is soon to become available. The latter is, however, an unpolarized high-energy ($E_e \sim 6$ GeV), and high-current (*i.e.*, high-background) experiment aimed at measuring excited and exotic (pentaquark) Ξ states. Since only the part of the tagger covering photon energies above 4.5 GeV was in the trigger, the data are not suitable for N^* physics.

One of the four approved experiments from the g2 run period, and the only one dealing with strangeness, was E-89-045 [56]. It envisaged both inclusive and exclusive measurements of the cross sections for the six elementary strangeness production channels on the nucleon as well as the investigation of the hyperon-nucleon interaction.

There are inclusive [57] and exclusive [58] cross-section analyses in progress for the $\gamma n \to K^+\Sigma^-$ channel using the g2 data. The recent high-statistics (10 billion triggers) g10 experiment [59], has also made it possible to start exclusive analyses for the $\gamma n \to K^0_s\Lambda$ and $\gamma n \to K^0_s\Sigma^0$ neutron channels [60], as well as the $K^+\Sigma^-$ [61], aimed at extracting the differential cross sections and the recoil polarization.

Unfortunately, neither of these two data sets allows further polarization studies. In the case of g2, which did use a circularly polarized photon beam, the main obstacle is insufficient statistics. Today, progress in operation of the accelerator also allows higher electron-beam polarization (80 - 85%), which translates into higher (circular) photon polarization. During the g10 run period, however, a polarized electron beam was not requested and was not delivered.

For linearly polarized photon beams, there are currently no CLAS data on the deuteron. The recent g8b run did, however, clearly demonstrate the capabilities of the coherent-bremsstrahlung facility in Hall B, reaching 92% linear polarization with the coherent photon peak at 1.3 GeV. In this kind of experiment, the capability of CEBAF and the CLAS before the 12 GeV upgrade are unique. No other laboratory offers a comparable combination of en-

ergy, luminosity, polarization, and charged-particle acceptance that is required for exclusive measurements.

3.1.2 Deuteron experiments at other facilities

Other photon facilities include GRAAL in Grenoble and MAMI in Mainz, which have (or will have) beam energies of 1.5 GeV (in the latter case after the planned upgrade). This is below the threshold of most third-tier N^* resonances, including the $D_{13}(1900)$.

The ELSA facility in Bonn [62] uses the same coherent-bremsstrahlung method to produce linearly polarized beams that is employed at JLab, but its maximum electron energy is considerably lower (nominally 3.5 GeV). Since the degree of linear photon polarization increases with the ratio of E_e/E_γ, the facility in Hall B is significantly better for higher photon energies. More importantly, the current detector configuration at ELSA is intended for neutral particles, and can therefore be seen as complementary to the CLAS.

LEPS at Spring-8 [63] has highly polarized back-scattered photon beams (up to 2.4 GeV using a 351-nm laser). Recently, beam polarization asymmetries for the $\vec{\gamma}p \to K^+\Lambda$ and $\vec{\gamma}p \to K^+\Sigma^0$ channels were published [64]. Preliminary results from an inclusive measurement of the differential cross section (σ_0) and beam asymmetry (Σ) in the $\vec{\gamma}n \to K^+\Sigma^-$ channel are now also available [65]. It will be interesting to compare them with the corresponding CLAS analysis [57]. In contrast to the CLAS, however, the detector acceptance is limited to very forward angles, which is not suited for exclusive measurements, and gives very poor kinematic coverage. Therefore, polarization observables that involve the hyperon recoil polarization ($P, T, O_{x'}, O_{z'}, C_{x'}, C_{z'}, T_{x'}, T_{z'}, L_{x'}, L_{z'}$) cannot be measured. Neither is it possible to separate rescattering events from quasifree ones. Thus, this facility cannot be used for studying the physics presented in this proposal; such data can be helpful only in determining the total cross section.

3.2 N^* decays to $K\vec{\Lambda}$ and $K\vec{\Sigma}$

The photon polarization will allow us to extract new observables, but much of the basic analysis will be similar to that for the exclusive cross-section measurements of the $\gamma n \to K^0\Lambda$, $\gamma n \to K^0\Sigma^0$, and $\gamma n \to K^+\Sigma^-$ reactions. We thus have a good handle on channel selection and identification of the quasifree events. The analysis of the $K^+\Sigma^-$ channel requires the detection of a K^+ and a π^-, as well as a neutron in the electromagnetic calorimeter. A detailed description of the analysis of this reaction, using the g2 data set, is available in the form of a CLAS analysis note [58].

The unpolarized K^0 channels for the neutron are part of a CLAS Approved Analysis (CAA-HS06-01) using the g10 data set [60]. Here, all four final-state particles from the charged decays of $K^0_s \to \pi^+\pi^-$ and $\Lambda \to p\pi^-$ are detected in CLAS. For pions and protons, particle identification is straightforward. The energy-loss corrections are calculated from the decay vertices, which are also used to determine the primary reaction vertex.

Figure 12 shows the $p\pi^-$ and $\pi^+\pi^-$ invariant masses, used for channel selection, with only particle-ID cuts. The standard g10 tagger [66], momentum, and beam-energy corrections have been applied, and the plots include both possible π^- assignments. Events that fall within 3σ of the $K^0_s\Lambda$ peak for both cases are shown in the superimposed histograms in the left panels (after multiplication by 100). Half of them constitute a combinatoric background, which is on average less than 0.1%. Cuts on missing mass, as well as vertex position and time, dramatically reduce all background, practically eliminating the ambiguous events from all kinematic bins.

The quality of the event selection and vertex reconstruction can be judged by how well the K^0_s and Λ lifetimes are reproduced for lifetimes above the range dominated by the CLAS resolution. The fits in Fig. 13 show that the decay constant for the Λ matches exactly the value listed by the Particle Data Group (PDG) [23], and the K^0_s falls within 0.1 ns^{-1} of the PDG value.

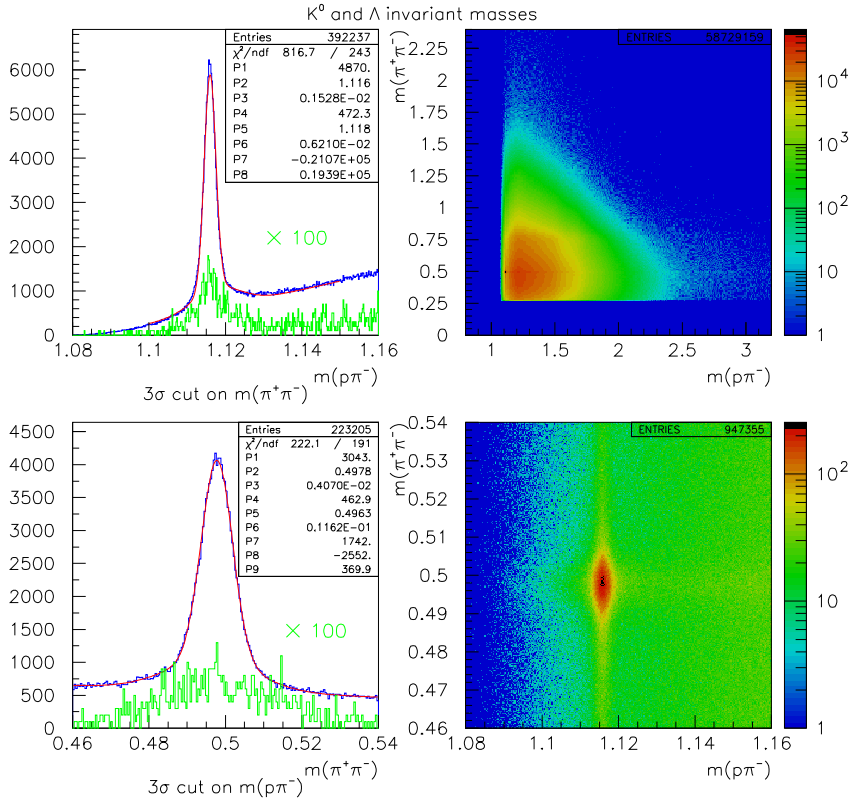

Figure 12: Combinatoric background. The invariant masses of $\pi^+\pi^-$ and $p\pi^-$ from the low-torus-field part of g10 shows the $K^0_s\Lambda$ peak (right) and its projections (left). Only particle-ID cuts have been applied. In the panels on the right the invariant masses are summed over both possible π^- assignments. Ambiguous events that, for both cases, fall within 3σ of the $K^0_s\Lambda$ peak are shown (multiplied by 100) in the superimposed (green) histograms on the left. Half of these events constitute a combinatoric background, which is less than 0.1%, and is eliminated by missing-mass cuts.

Since the Σ^0 decays into $\Lambda\gamma$ with a branching ratio of 100%, it is essential to separate a Λ from the Σ^0 decay from one produced directly. When using a proton target, this can be done using the kaon missing mass. Owing to Fermi motion, this is no longer possible for deuterium. Figure 14 shows, however, that by combining the kaon missing mass, as it would appear in an inclusive measurement, with the missing mass of $K^0_s\Lambda$, one can see that the Λ and Σ^0 peaks are clearly separated. The projections on the $K^0_s\Lambda$-axis, in the same figure, show the background to be very small. A double-Gaussian fit gives a good description of the $K^0_s\Lambda$ missing-mass distribution, making it possible to determine the Σ^0 tail under the

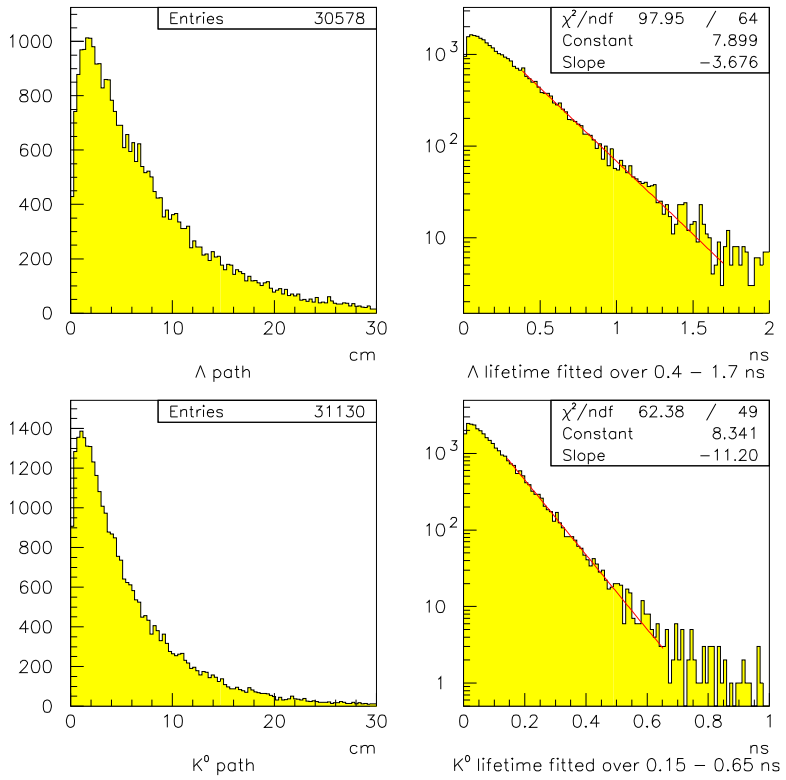

Figure 13: K_s^0 and Λ paths and lifetimes. As expected from the CLAS resolution, there is a slight deficit of events with short path lengths. The agreement of the fits with the PDG values [23], 11.2 ns^{-1} for the K_s^0 and 3.8 ns^{-1} for the Λ, are good, indicating a satisfactory event selection and vertex reconstruction.

Λ peak with good accuracy. In principle, the fit could be improved by taking into account the background from events with an additional π^0 (the threshold is at 1.07 GeV due to the slight shift in the proton missing mass). But since this component is increasing with the $K_s^0\Lambda$ missing mass, and yet the number of events in the upper tail of the Σ^0 peak is close to zero, one can conclude that it gives a negligible correction in the region of the Σ^0, and none for the Λ. The yields for both channels can be reliably extracted from a simultaneous fit to both peaks in the $K_s^0\Lambda$ missing-mass distribution, without the complication of having to detect the γ from the Σ decay in the electromagnetic calorimeter. The latter would introduce significant statistical and systematic uncertainties due to, respectively, a reduced and altered

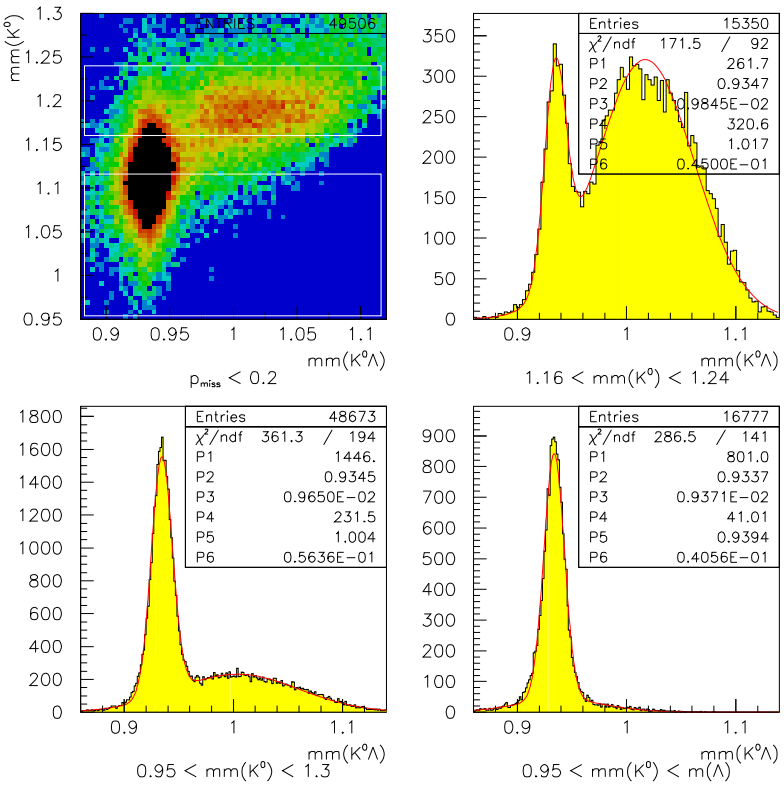

Figure 14: A good $\Lambda - \Sigma^0$ separation can be achieved using the missing mass of the kaon (the hyperon mass) and $K^0_s\Lambda$ (the spectator-proton mass). An undetected γ from Σ^0 decay makes the latter distribution broader, peaking to the right of the Λ (top left). The projection (bottom left) shows that the data are well described by a double-Gaussian fit. The background is small. On the right are projections for two K^0_s missing-mass ranges indicated in the top left panel, the lower showing that a clean Λ signal can be extracted with a reasonable loss in statistics. In addition to the cuts on the K^0_s and Λ invariant masses, these histograms require that $p_{spectator} < 0.2$ GeV (see Fig. 15).

acceptance. Due to a higher background, the uncertainty in the yield extraction from the Σ^0 invariant mass would also be higher. The lower right panel in Fig. 14 also shows that by imposing a cut on the K^0 missing mass, one can define a subset containing at least half of the $K^0_s\Lambda$ events where there is no Σ^0 contamination. This gives three options for the extraction of polarization observables for the $K^0\Lambda$ channel. One can use the reduced set, which gives a larger statistical uncertainty. One can treat the Σ^0 admixture as a systematic uncertainty. Or, since this admixture will be well known, the mixed data can be used as input for the

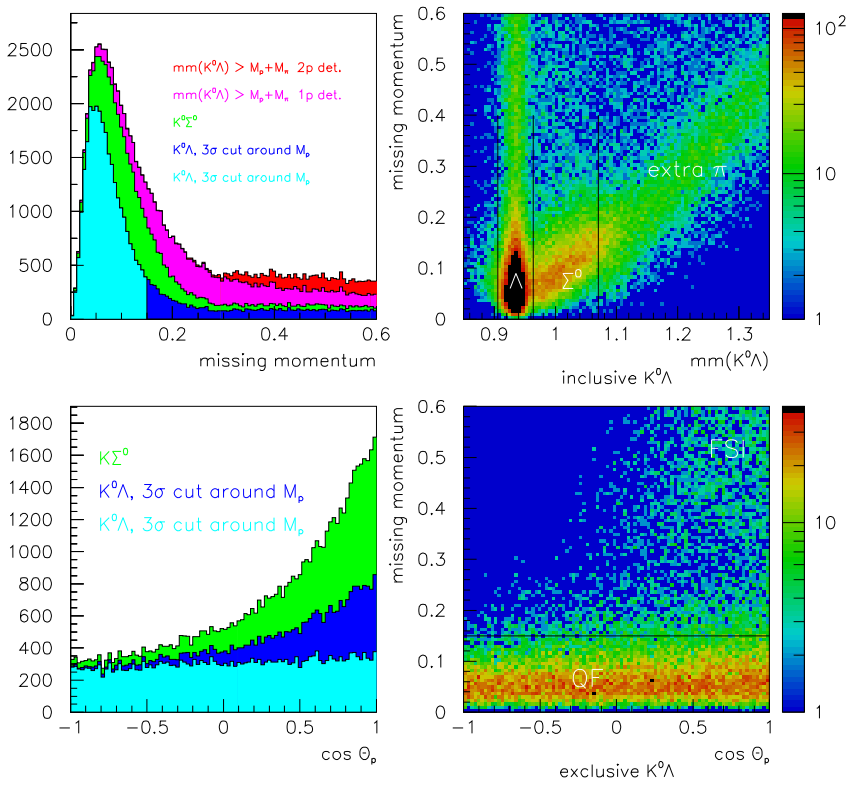

Figure 15: Spectator-proton selection. *Top left:* missing (proton) momentum. *Bottom left:* spectator-proton angular distribution. The distribution of low-momentum spectators is isotropic in the lab frame for exclusive $K^0_s\Lambda$ events. The undetected photon emitted from forward-moving Σ^0s makes the missing protons from those events appear to be forward peaked. *Top right:* $p_{missing}$ vs. mm($K^0_s\Lambda$), showing exclusive $K^0_s\Lambda$ events on the left, a band with extra pions on the right, and $K^0_s\Sigma^0$ events in the middle. *Bottom right:* Exclusive $K^0_s\Lambda$ events with spectators in the lower band and protons that have undergone final-state interactions in the at high momenta and forward angles. *Color coding on the left:* exclusive $K^0_s\Lambda$ (blue and cyan), $K^0_s\Sigma^0$ (green), and inclusive $K^0_s\Lambda$ with one (magenta) or both (red) protons detected.

coupled-channels analysis. The approach will be chosen depending on the statistics and the ratio between the Λ and Σ^0 cross sections in each bin. One should also note that the problem of Λ-Σ^0 separation does not occur in the $K^+\Sigma^-$ channel. In total, there are about 30,000 $K^0_s\Lambda$ and 20,000 $K^0_s\Sigma^0$ quasifree events in the low-torus-field part of g10.

While the ultimate goal is to have a unified description of both the elementary processes and final-state interactions, currently it is important to select kinematics that enhance the

quasifree process. The most straightforward way is to remove events with spectator momenta in the tail of the Fermi distribution. The lower right panel in Fig. 15 shows that final-state interactions involving the spectator proton dominate above 300 MeV/c (which is also the CLAS proton detection threshold). A cut at 150 MeV/c is, however, a more prudent choice. The upper left panel shows that the loss in statistics is modest, and the resulting $\cos\theta_{lab}$) distribution (lower panel) is almost flat. An isotropic distribution of the reconstructed spectators is, of course, what we expect from Fermi motion alone. In fact, the situation is better than Fig. 15 suggests, since a cut on only the $K^0_s\Lambda$ missing mass includes a small tail of Σ^0 events. These are forward-peaked, as the undetected photon comes from the decay of a forward-moving Σ^0. A naïve extrapolation from the high-momentum tail of the missing-momentum distribution nevertheless indicates some remaining events below the quasifree peak. This is, however, a worst-case scenario. The calculations shown in Fig. 16 indicate that the cross section for rescattering with almost zero momentum transfer is small.

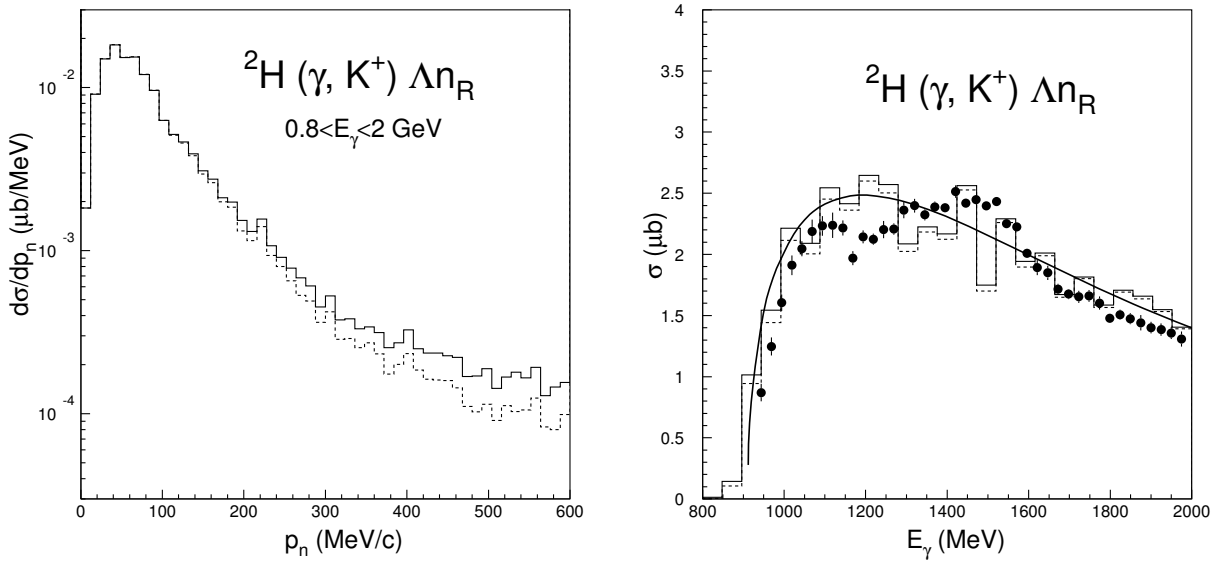

Figure 16: Rescattering contributions for the $\gamma p(n) \to K^+\Lambda(n)$ channel calculated using the model described in section 2.3. The solid line is the full calculation. The dashed shows the quasifree cross section. The left panel shows the rescattering as a function of the final spectator momentum, and the right as a function of E_γ. The latter also includes data points from McNabb *et al.* and a fit to the full calculation.

It is also not clear if such interactions would have any impact on the angular distributions used to extract the polarization observables. In order to minimize final-state interactions one can add cuts on the polar angle of the missing momentum, or the p_{min} of the spectator (see section 2.3). More importantly, varying the cuts on these parameters will provide yet another way of determining the systematic uncertainty due to rescattering of low-momentum spectators, in addition to model calculations and comparisons of our proton channels with measurements on a free proton target using the g8b (linear polarization) and g1c (circular polarization) data sets. The part with linearly polarized photons will be analyzed in a consistent fashion by the same group (Ireland, Livingston, *et al.*) that is analyzing kaon production in g8b. The analysis of the g1c data already has been completed by the CMU group [37]. In the extraction of polarization observables, asymmetries are constructed from yields. When the contribution from final-state interactions is known, it can be subtracted in each bin separately. The resulting uncertainty (see section 4.5) is thus not the fraction of rescattered events, but only the uncertainty in the subtraction.

A specific request that was made by one of the PAC readers of our Letter of Intent [18] was to investigate any correlations in the azimuthal angle φ between the spectator nucleon and the kaon or the lambda. As shown in Fig. 17, the φ-distributions of the K and Λ reflect the structure of the CLAS sectors, although not as sharply as for particles detected directly through their decay products, while that of the reconstructed spectator is flat. The differences in φ do, however, suggest that the Λ prefers to move in the φ-direction of the original target nucleon, while the kaon and the spectator nucleon tend to move in the opposite direction. This behavior is qualitatively well reproduced by a phase-space Monte Carlo calculation using realistic Fermi motion, based on the Paris potential, but without any final-state interactions. Results using the Argonne potential were similar. In reality, the cross section is more forward-peaked for the kaon (and *vice versa* for the Λ). The simulation thus gives larger transverse momenta for both strange particles, and somewhat different acceptances. In CLAS, the relative uncertainty in the measurement of small transverse

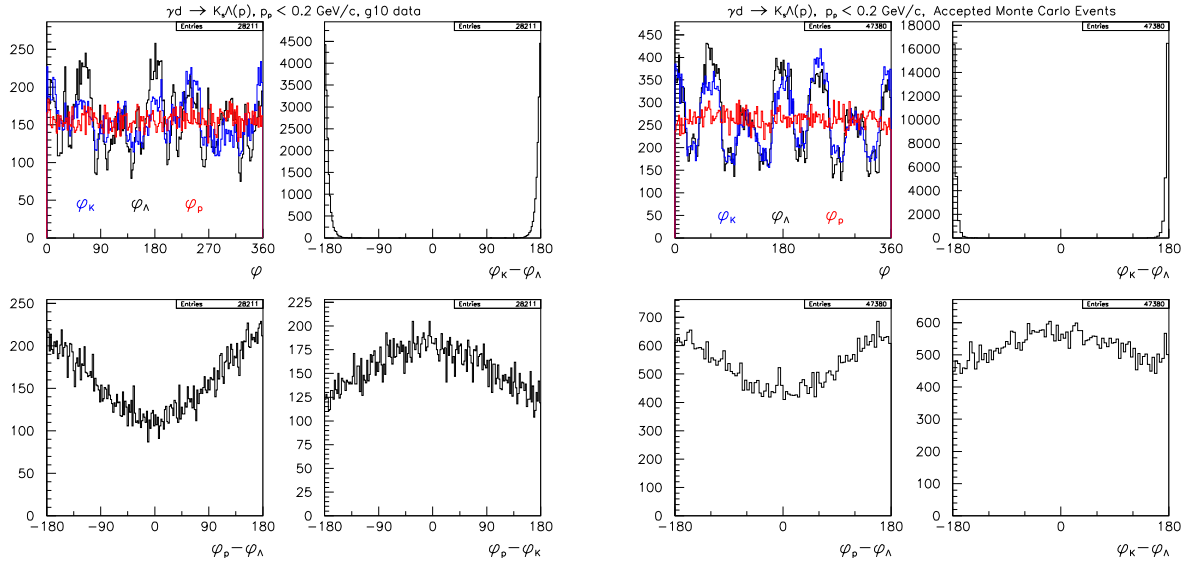

Figure 17: The distribution in φ is flat for the spectator protons ($p < 0.2$ GeV/c), and the K^0_s and Λ go back to back. Both the g10 data (left) and a phase-space Monte Carlo with Fermi motion, but without final-state interactions (right), show similar correlations in φ between the K^0_s, the Λ, and the spectator proton.

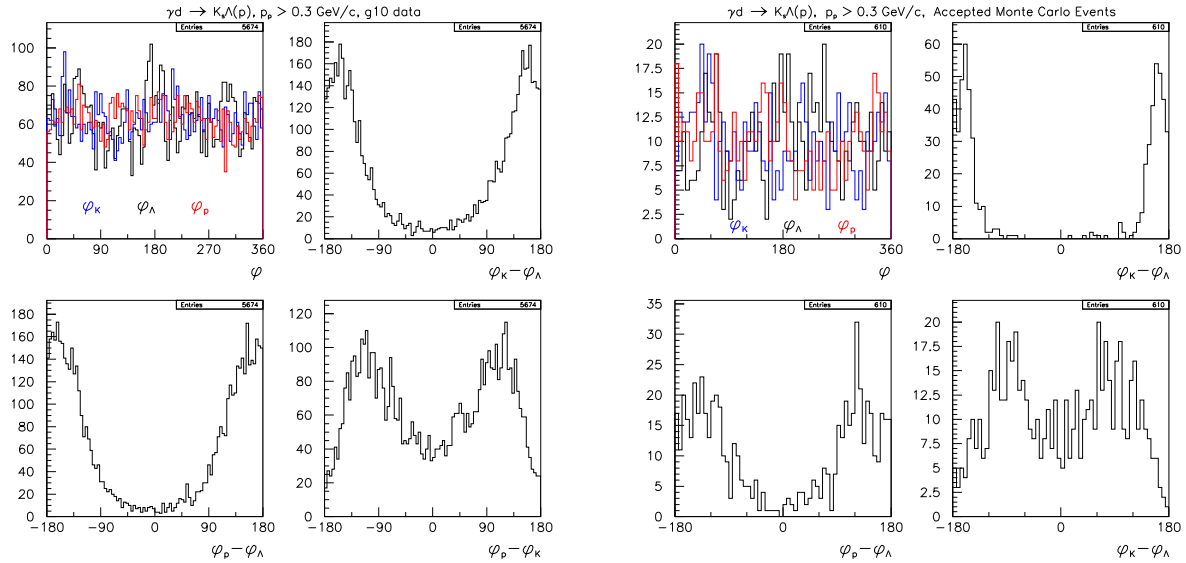

Figure 18: At high spectator momenta ($p > 0.3$ GeV/c), where one would expect the g10 data (left) to be dominated by final-state interactions, they are still in good agreement with the Monte Carlo (right). This suggests that rescattering is not a major factor in the observed φ-correlations.

momenta is large. Since the spectator is reconstructed from the missing momentum, it will be assigned any error in the measurement. At high spectator momenta, where one would expect the data to be dominated by final-state interactions, the correlations look very different (Fig. 18). This is, however, also reproduced by the Monte Carlo, which suggests that correlations in φ are not very sensitive to rescattering.

Our conclusion from this study is therefore that there is no reason to doubt the conventional wisdom, supported by calculations (see, *e.g.*, Fig. 16), that the contribution to the cross section from final-state interactions involving low-momentum spectators is relatively small. The same applies to any initial-state interactions, which also transfer momentum to the spectator nucleon. Instead, we are confident that the observed φ-correlations are due to a combination of kinematics, acceptance, and uncertainty in the measurement of the transverse momentum.

The raw $K_s^0\Lambda$ and $K_s^0\Sigma^0$ yields for the low-field part of the g10 data are shown in Fig. 19. Although corrections for acceptance and photon flux can change the shape of these spectra, the figure shows how the events are distributed, thus serving as a guideline for the circularly polarized part of the measurement, which will have a similar photon spectrum. The $1.7 < W < 2.3$ GeV region is well covered, but there is a significant difference in statistics between upper and lower ends. This has to be kept in mind when comparing with the yields for linearly polarized photons, where the time allocated for each photon energy can be adjusted individually. In order to have the same statistics in the high-energy bins for both polarizations, the total yield has to be higher when using circularly polarized photons.

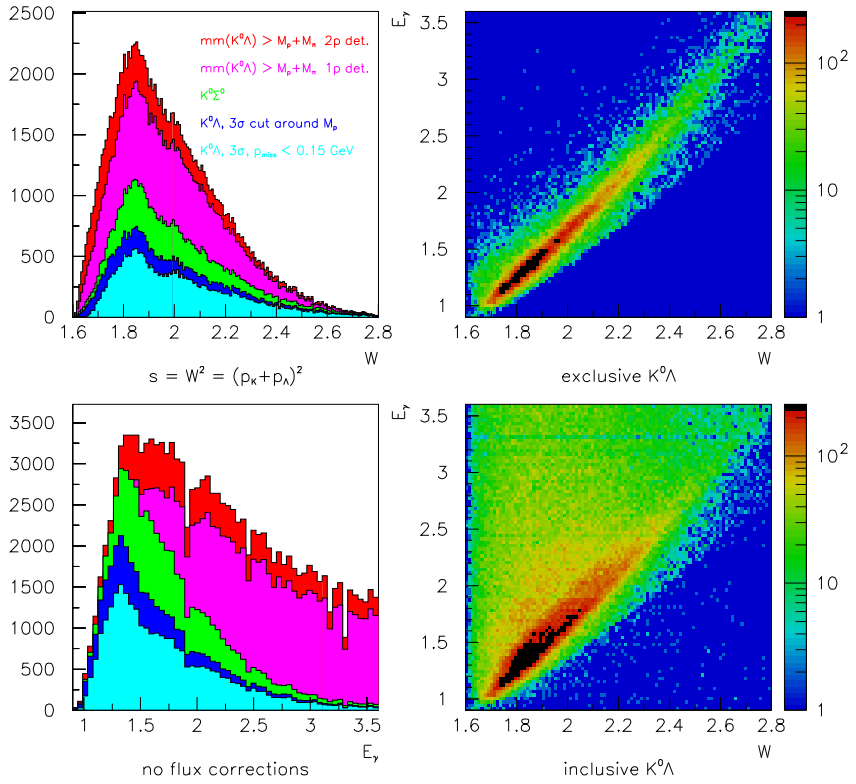

Figure 19: Preliminary total yields from the low-field part of g10, not corrected for photon flux or CLAS acceptance. They are plotted as functions of $W = \sqrt{s}$, calculated from the final state (top left), and E_γ (bottom left). On the right are $W - E_\gamma$ correlations for inclusive (bottom) and exclusive (top) $K^0_s\Lambda$ events. Color coding, and missing mass cuts, on the left are as in Fig. 15: exclusive $K^0_s\Lambda$ (blue and cyan), $K^0_s\Sigma^0$ (green), and inclusive $K^0_s\Lambda$ with one (magenta) or both (red) protons detected. All have 3σ cuts on the invariant masses of the Λ and the K^0_s.

3.3 N^* decays to $K^*\vec{Y}$ and $K\vec{Y}^*$

So far, coupled-channels analyses for N^* physics have mostly been performed using pion, eta, and kaon production. In the future, more constraints can be added by including K^*Y and KY^* channels. A study of N^* decays by Capstick and Roberts [17], using a quark-pair creation model, has predicted that some low-lying negative-parity states, including several missing nucleon resonances, could couple strongly to the K^*Y and KY^* channels. There are several ongoing analyses using existing CLAS g10 and g11 data, for the $\gamma p \rightarrow \ K^{*+}\Lambda$,

$\gamma p \to K^{*0}\Sigma^+$, $\gamma p \to K^+\Sigma^0(1385)$ [67], and $\gamma n \to K^+\Sigma^-(1385)$ [60] channels. The $K^+\pi^-\pi^-p$ final state of the last one is well suited for exclusive measurements in CLAS, but since neither g10 nor g11 used polarized photons, no polarization observables other than the cross section and recoil polarization (P) can be determined. The analysis of the proton channels has already resulted in preliminary total cross sections [68]. The systematic uncertainty due to normalization and model dependence of the yield extraction is estimated to be about 20%. The KY^* and K^*Y cross sections do not seem to be negligible compared with that for $K^+\Lambda$, suggesting that these channels should be incorporated into future coupled-channels analyses. These preliminary results are likely to change with further studies of the systematics, but they can serve as a guide for the statistics that we can expect in our proposed experiment.

Although no theoretical calculation is yet available for the sensitivity of polarization observables to the nucleon resonances for the K^*Y and KY^* channels, there is no reason to assume that it should be smaller than for the KY case. There is, however, a theoretical interest to include these reactions in the coupled-channels analyses. The first calculations of the background contributions are already available [69].

For the K^*Y channels, Capstick and Roberts predict that the two-star state $N[\frac{3}{2}^-]_1(2080)$ and the weakly established $N[\frac{1}{2}^-]_1(2090)$ state couple to $K\Lambda$ and $K^*\Lambda$ with comparable strength. It has been pointed out that the t-channel vector-meson exchange and the seagull term are proportional to the charge of the outgoing K^* meson [70]. The suppression of t-channel background processes makes neutral K^* production seem very promising. Here, a deuteron target is advantageous since it allows the study of the reaction $\vec{\gamma}n \to K^{*0}\Lambda \to K^+\pi^-\pi^-p$. As noted for the $K^+\Sigma^-(1385)$, this final state is well suited for the CLAS. An exclusive measurement of the K^{*0} channel on the proton would, on the other hand, require the detection of either the neutron or π^0 from the decay of the Σ^+. Missing-mass techniques can be used for the cross section, but are not suitable for the determination of polarization observables.

Currently, only a few KY^* cross-section measurements have been made, all using proton

targets. There are, however, several N^* states, including the $N[\frac{1}{2}^-]_5(2070)$ (established in pion production) and the $\Delta[\frac{3}{2}^-]_3(2145)$, that are predicted to couple strongly to KY^* channels, in particular the $K\Sigma(1385)$. The low-lying KY^* channels should also be important for lighter missing resonances, such as the $N[\frac{5}{2}^+]_2(1980)$ and $\Delta[\frac{3}{2}^+]_3(1985)$, which are below the K^*Y threshold. As for the K^{*0}, preliminary differential-cross-section results for the $\gamma p \to K^+\Sigma^0(1385)$ reaction, obtained using the g11 data set, show a smaller contribution from t-channel processes than is the case for the $K^{*+}\Lambda$ channel.

3.4 Rescattering

Rescattering can be studied using the Laget approach [33], which predicts a strong enhancement close to zero for the calculated minimum possible momentum of the "spectator" proton before the rescattering, assuming that both hadrons propagate on shell. Figure 20 shows the preliminary p_{min} distribution that we presented at NSTAR 2005 [34, 71]. What appears to be a $\Sigma^-(1385)$ rescattering peak can be clearly seen at zero. The statistics in the plot are modest, since it was required that all five final-state particles be detected in CLAS, as well as that $-t > 0.5$ GeV^2 and $0.4 < p_{spectator} < 0.6$ GeV. It demonstrates, however, that a reasonably clean sample of events can be selected for which the hyperon was rescattered on the spectator nucleon. Events where the kaon was rescattered can be removed in a similar

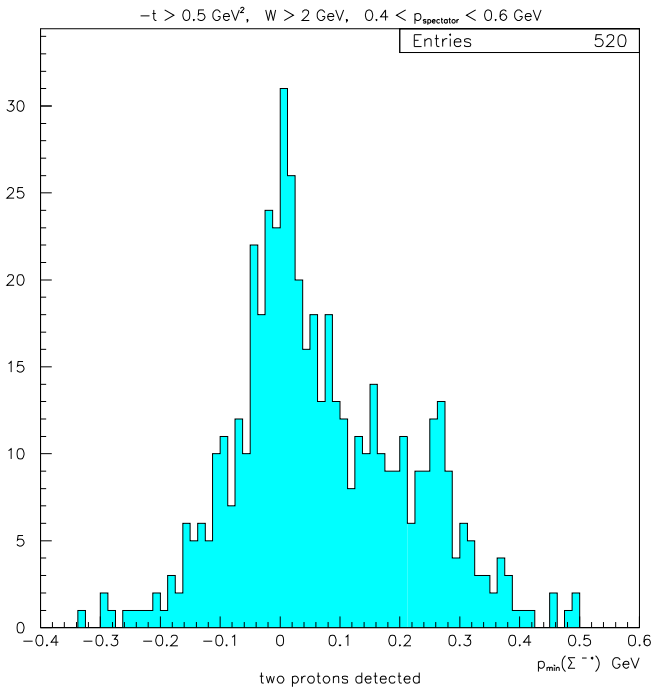

Figure 20: The $\Sigma^-(1385)$ rescattering peak can be seen in the minimum momentum $p_{min}(\Sigma p)$ that the spectator proton could have had before the rescattering (see section 2.3). The statistics are modest because a -$t > 0.5$ GeV^2 cut has been applied and the detection of all final-state particles is required. In this particular histogram, possible K^{*0} background has not been eliminated.

way, which is made easier by the fact that the background under the kaon peak is smaller. This also applies to the less exotic, but perhaps more important, $\Lambda - N$ scattering.

The statistics can be increased by looking at event topologies where either the spectator nucleon or the kaon is not detected, but reconstructed from kinematics. The latter is particularly attractive when dealing with the K^0, only a third of which decay into $\pi^+\pi^-$. When not rescattered, the angular distribution for the kaons also tends to be strongly forward-peaked, whereas that for true spectator protons is isotropic in the lab frame (see Fig. 15). Although rescattering changes this picture somewhat, the acceptance for these protons remains significantly larger than that for both pions from the K^0_s decay. Nevertheless, the number of events in the tail of the spectator-nucleon momentum distribution will always be smaller than for the quasifree case (where the spectator momentum usually is below the detection threshold).

The ability to select rescattering events also opens up the possibility of studying polarization degrees of freedom. As predicted in [49], measurements on the free nucleon show a significant hyperon recoil polarization at moderate momentum transfer (t). Rescattering effects in the deuteron are thus very well suited for investigating the $\vec{Y} - N$ interaction. Even without cuts on the reconstructed initial minimum spectator momentum, calculations demonstrate a high sensitivity of polarization observables to various interaction potentials and partial waves [35]. Obtaining good polarization data with a large-acceptance detector, required for exclusive measurements, would thus open a new window on this field, not accessible through the study of bound hypernuclear states.

4 Running Conditions

This proposal requests two separate running conditions, one with linearly and one with circularly polarized photons. The former is required for the measurement of four observables (Σ, T, $O_{x'}$, $O_{z'}$). The latter adds $C_{x'}$ and $C_{z'}$. Both can be used to measure σ_0 and P.

The circular measurement can make effective use of low-energy beams ($\sim$ 2.4 GeV), and thus can run concurrently with experiments like G0. In contrast, the preferred beam energy for a linear measurement would be 4-5 GeV, although some data could be taken at 3 GeV. Neither measurement requires any new hardware or non-standard running conditions. A summary of the running conditions is given in Table 4.

Running condition	Circular polarization	Linear polarization
main torus current	-1500 A	-1500 A
trigger	two-sector	two-sector, no tagger
tagger rate	16 MHz	47 MHz
photon flux	14 MHz	10 MHz
beam current	18 nA	10 nA
radiator	10^{-4} r.l.	diamond (50 μm)
target	LD_2	LD_2
target length	40 cm	40 cm
target position	-20 cm	-20 cm

Table 4: Summary of running conditions.

4.1 Linear photon polarization

4.1.1 Photon energies

The data to be taken with linear photon polarization are naturally divided into energy bins corresponding to different positions of the relatively narrow coherent-photon peak. The six

settings that interest us the most are when the upper edge of the coherent peak is located at 1.3, 1.5, 1.7, 1.9, 2.1, and 2.3 GeV, covering the $1.7 < W < 2.3$ GeV range. Another advantage of selecting these particular points is that they were used in the g8 experiments (the first five in g8b), making it straightforward to compare reactions on a free proton with one bound in the deuteron.

4.1.2 Beam energy and photon polarization

Figure 21 shows the level of linear polarization as a function of the selected position of the coherent-photon peak for 5- and 3-GeV electron beams based on the analytic bremsstrahlung calculation by Natter *et al.* [72]. The photon polarization is largest for the highest electron energies and the lowest photon energies. On the other hand, it is critical that the position of the beam on the diamond radiator be stable, which is easier to achieve when the electron energy is slightly below maximum. The optimum electron beam energy would thus be around 5 GeV.

Figure 21 also shows the photon spectra (the relative intensity is called "enhancement" in the figure) for each photon energy bite. A comparison with g8b data is shown in Fig. 22. As the edge of the coherent peak is moved to higher E_γ, the width of the peak increases. With a 5-GeV electron beam, the polarization is reasonably constant over a 200-MeV region, but decreases rapidly in the tail of the distribution. The relative change in intensity for this bin between the first (1.3 GeV) and last (2.3 GeV) settings is almost a factor of two. At 3 GeV, the polarization drops off faster - more than 10% over 100 MeV. More beam time is thus required, especially for the bins at higher E_γ, in order to have a constant flux. The 10% decrease in maximum polarization also increases the need for statistics at 3 GeV. In both cases, some of the beam time will also have to be allocated for runs with an amorphous radiator.

In general, one would avoid running with anything but the highest possible polarization.

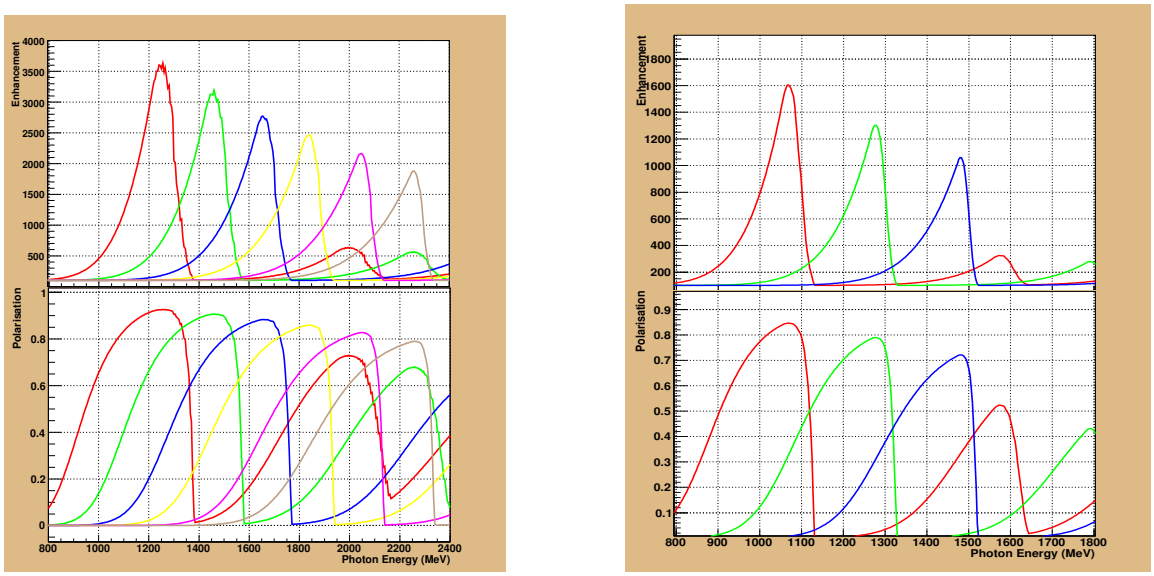

Figure 21: Calculated linear photon polarization and enhancement (*i.e.*, photon flux in arbitrary units) as a function of E_γ for 5 GeV (left) and 3 GeV (right) electron beams. The colors correspond to various settings of the goniometer, which is used to shift the edge of the coherent-photon peak.

Otherwise it will, at best, take longer to achieve the desired result. Our request is thus made for a 5-GeV electron beam. However, should beam time be available at lower energies, it might nevertheless be preferable to run part of the experiment under such conditions. Scheduling flexibility is a major advantage of the proposed experiment. The polarization calculations show that one should avoid running with an electron beam energy that is less than twice the desired maximum photon energy. A 3-GeV beam would thus be acceptable for the two lowest energy settings, which would then have a maximum polarization comparable with the highest setting, with the coherent edge at 2.3 GeV.

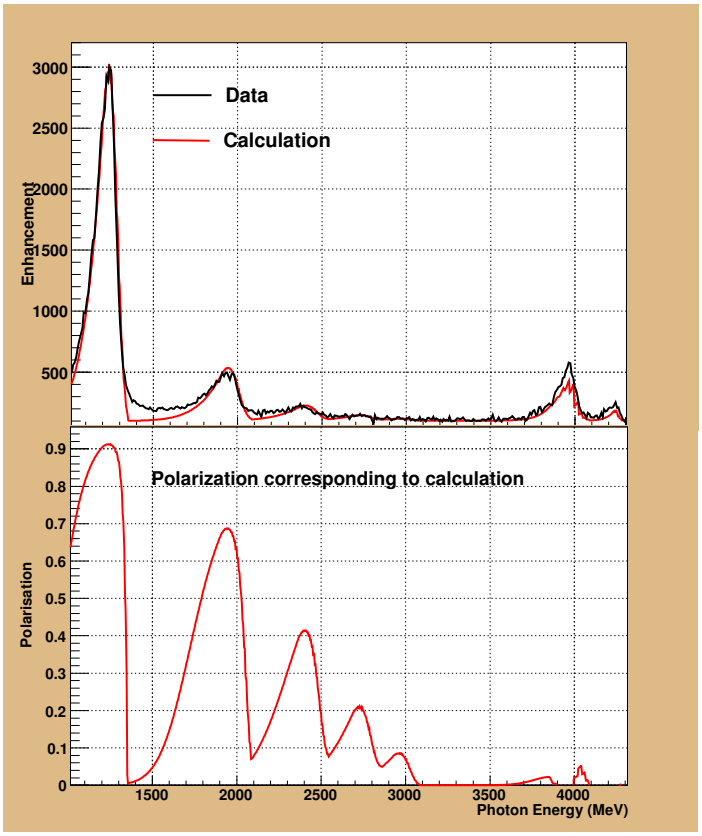

Figure 22: Comparison of a coherent bremsstrahlung calculation with g8b data.

4.1.3 Inner calorimeter

Moving the target upstream will also make it possible to use the inner calorimeter (IC) that was built for the e1-DVCS experiment. This would extend the acceptance for forward-going particles, both charged and neutral (*e.g.*, the K_L^0), to smaller angles. It is not feasible to use it in a regular bremsstrahlung experiment (like our run with circular polarization), since the hadronic rate would be very small compared with the electromagnetic background, which is mainly caused by the low-energy part of the photon spectrum. For linear polarization, however, the narrow photon peak that is produced by the diamond radiator has only a small low-energy tail. While not required for the proposed experiment, the IC would provide a useful additional feature.

4.1.4 Trigger

The g8b experiment, using a one-sector trigger with a single-track level-2 requirement, was limited by the tagger, but the data-acquisition system was operating close to its maximum capacity. In our case, the hadronic rate will be approximately doubled by substituting deuterium for hydrogen, requiring a more restrictive two-sector trigger (using the start counter), with a possible level-2 requirement. A significantly pre-scaled single-track trigger will make it possible to evaluate any trigger inefficiencies for events with two particles. For multi-track events this correction would be small. While not required for any of the reaction channels in the proposed experiment, it is possible to add a pre-scaled one charged + one neutral trigger for the benefit of other analyses. The rate in the tagger will be too high to have it in the trigger.

4.1.5 Tagger

Figure 23 shows the tagger-rate distribution for the $1.3 < E_\gamma < 1.5$ GeV bin from the g8b run when the total rate on the tagger was 45 MHz (22 ns^{-1}). This corresponds to a collimated rate (photon flux) on the target of 9.6 MHz in the coherent peak. The substitution of deuterium for hydrogen will not increase the electromagnetic background, and the hadronic background in CLAS will remain small. The new multi-hit TDCs allow each T-counter to register many photons for each trigger. However, since most of the photons are close in energy, it will be difficult to select the correct one if two or more arrive within the same beam bucket (2 ns). Such events can, however, be easily identified. At the proposed rate (one electron in the tagger every 22 ns) the number of such accidentals will be acceptable.

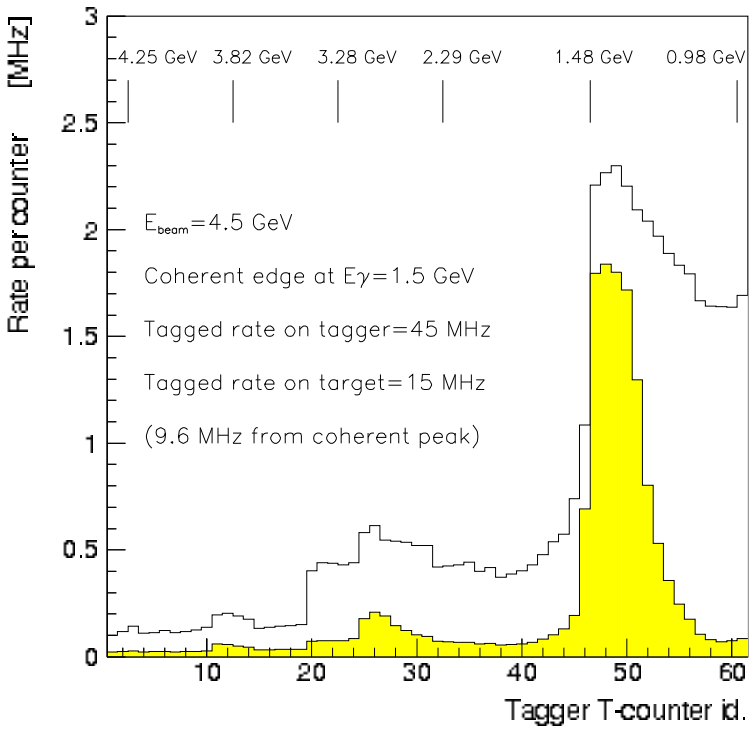

Figure 23: The rate per T-counter in the tagger for running conditions corresponding to g8b with the coherent peak at 1.3 - 1.5 GeV before and after collimation (yellow).

4.2 Circular photon polarization

4.2.1 Beam energy and photon polarization

For circularly polarized photons, the polarization is highest when the ratio of the bremsstrahlung photon energy to the electron energy is the highest, as shown in Fig. 24 [73]. Our focus is to have sufficient statistics and good polarization for W between 1.8 and 2.3 GeV ($1.3 < E_\gamma < 2.3$ GeV). The optimal electron beam energy is thus 2.4 GeV, although energies up to 3 GeV would be acceptable. The maximum longitudinal electron-beam polarization at JLab is 80-85%. Using the lower value as a conservative estimate, a 2.4-GeV electron beam would give 75% polarization at $E_\gamma = 1.9$ GeV and 45% at $E_\gamma = 1.1$ GeV.

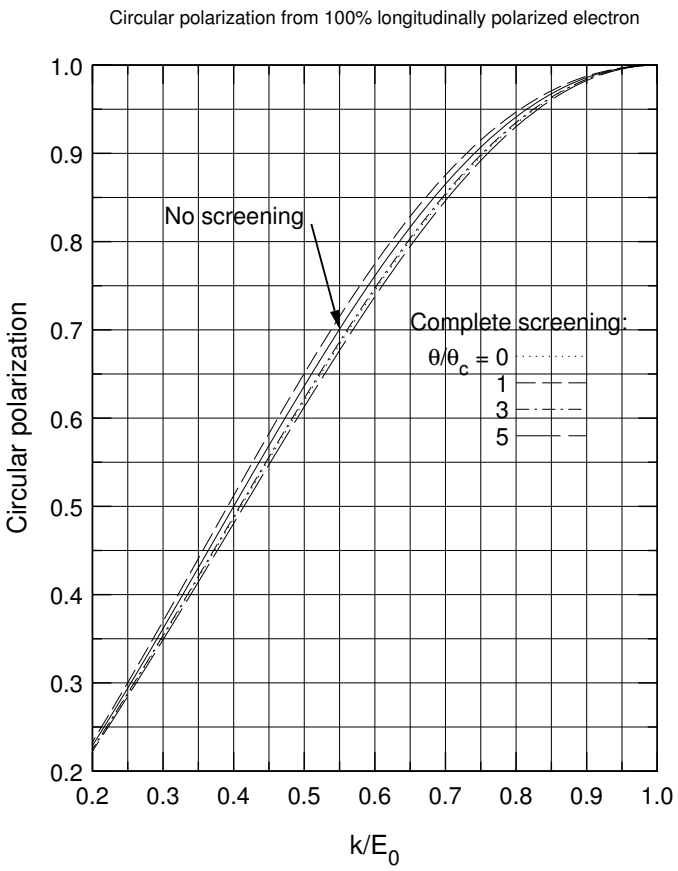

Figure 24: Circular photon polarization as function of E_γ/E_e. The photon polarization is also proportional to the longitudinal electron-beam polarization, which can reach 80-85% at JLab.

4.2.2 Trigger and Tagger

A two-sector trigger with a two-track level-2 requirement will be used. With a 2.4-GeV electron beam, the tagger covers photon energies in the 0.5 - 2.3 GeV range. The Λ threshold is at 0.91 GeV. Since the photon flux is the highest at the lowest energies, the dead time can be markedly reduced by excluding the tagger T-counters 42 to 61 from the trigger. If the tagger were to be put in the trigger, the total rate would have to be kept much lower since the trigger gate is 20 ns long (compared with the 2-ns separation between bunches).

4.3 Rate estimate

Since there are not yet any published strangeness photoproduction data on the neutron to constrain the theory, model-dependent cross sections have very large uncertainties. One of the PAC readers of our Letter of Intent thus strongly recommended trying to obtain model-independent rates, which could serve as a basis for a realistic beam-time request. Our method is to scale the actual CLAS yields from the low-field part of the g10 run period [60] by the ratios of the photon flux, target length, and acceptance for each bin in the proposed experiment, for both photon polarizations. Monte Carlo simulations are then used to obtain the acceptance ratio, which carries a much smaller uncertainty than a simulation of the acceptance itself.

4.3.1 Binning

Using linearly polarized photons, the six settings for the coherent peak form a natural binning in E_γ. Data from each setting will be divided into ten bins in $\cos(\theta_K^{cm})$. Since the variation of the polarization observables is greater in $\cos(\theta_K^{cm})$ than in E_γ, this makes a balanced binning that is equally suitable for circular polarization. The latter will also allow for a threshold bin (0.9 - 1.1 GeV). In total, 520 data points ($6 \times 80 + 1 \times 40$)will be measured for each channel, at least 400 of which will have sufficiently small uncertainties to make a significant impact on coupled-channels calculations.

4.3.2 Acceptance

The measurement of all of the exclusive processes listed in this proposal requires detection of one or two negatively charged particles, such as the π^- from Λ decay, together with positively charged particles. In order to maximize the acceptance, the data need to be taken with a low main torus field. This was done for half of the g10 data set, where a torus current of 2250 A was used. In g8b, 1930 A was used. From the e1c 2.567-GeV data, taken with both 2250 A and 1500 A settings, we know that the acceptance is significantly better for the

$cos(\theta_K^{cm})$ / E_γ (GeV)	-0.7	-0.5	-0.3	-0.1	0.1	0.3	0.5	0.7	0.9
1.1 - 1.3	0.8	1.1	1.2	1.3	1.5	1.3	1.4	1.2	1.2
1.3 - 1.5	1.0	1.3	1.5	1.5	1.6	1.5	1.6	1.8	1.2
1.5 - 1.7	1.2	1.6	1.7	1.6	1.6	1.6	1.5	1.7	1.3
1.7 - 1.9	1.7	1.8	1.8	1.5	1.6	1.5	1.4	1.5	1.4
1.9 - 2.1	1.9	1.7	1.8	1.5	1.5	1.4	1.5	1.5	1.9
2.1 - 2.3	2.1	2.0	1.8	1.5	1.5	1.3	1.3	1.4	1.2

Table 5: Acceptance ratios (-1500 A / 1500 A) for the $\gamma n \to K_s^0\Lambda$ reaction, showing the advantage of using a field with reversed polarity. The Monte Carlo used 2 million generated events for each setting.

latter, with a modest ($< 30\%$) increase in sigma for the invariant (and missing) mass of the Λ. For completeness, simulations were also made for 1920 A and 1700 A. The $\gamma n \to K_s^0\Lambda$ acceptance was further increased by reversing the polarity of the field, which was beneficial for low-momentum pions from the hyperon decays. The improvement due to the field reversal is shown for each kinematic bin in Table 5. Due to the low Monte Carlo statistics in the most backward $cos(\theta_K^{cm}) = -0.9$ bin, the corresponding values for $cos(\theta_K^{cm}) = -0.7$ were used.

The acceptance will be further increased by moving our 40-cm-long LD_2 target upstream by 20 cm, as was done in g8b. In g10, a 24-cm-long target was moved 25 cm upstream. The full acceptance ratios for the $\gamma n \to K_s^0\Lambda$ channel between the proposed running conditions and those for g10 are shown in Table 6. Eight million events were generated for each Monte Carlo. Despite the better statistics, the uncertainties in the $cos(\theta_K^{cm}) = -0.9$ and $cos(\theta_K^{cm}) = -0.7$ bins are still considerable; but due to the small number of events there, the rate estimate for each E_γ bin is not significantly affected.

4.3.3 Linear polarization

For the linearly polarized part of the proposed experiment, the rates can be obtained from the g10 rates, multiplied by the ratios of the target lengths ($\frac{40}{24}$), acceptances in each bin (see

$cos(\theta_K^{cm})$ / E_γ (GeV)	-0.7	-0.5	-0.3	-0.1	0.1	0.3	0.5	0.7	0.9
1.1 - 1.3	13	8.7	6.2	6.0	4.9	5.0	5.1	6.8	9.7
1.3 - 1.5	8	6.9	5.4	4.7	4.2	4.0	4.3	5.8	7.8
1.5 - 1.7	11	7.2	4.9	3.9	3.4	3.4	3.5	5.1	7.9
1.7 - 1.9	15	6.5	4.3	3.3	3.1	2.7	3.1	3.4	7.6
1.9 - 2.1	17	5.6	4.0	3.0	2.7	2.5	2.8	3.9	7.1
2.1 - 2.3	19	5.9	3.6	2.8	2.5	2.4	2.5	3.5	5.2

Table 6: Acceptance ratios for the $\gamma n \to K_s^0 \Lambda$ channel for the proposed running conditions with respect to the g10 experiment. The larger ratios for the most forward and backward bins show a much improved kinematic coverage.

Table 6), and the photon flux. In the low-field part of g10, with 15 allocated beam days, the integrated photon flux for $1.1 < E_\gamma < 2.3$ GeV was 2.4×10^{13}. The ratio is taken between the proposed photon flux over each coherent-peak setting and the fraction of the g10 flux in the corresponding E_γ bin.

We evaluated two options for our flux. One was to use values from the FROST proposals (5 MHz in the eta proposal and 6 MHz in the kaon proposal). The other was to use values from the g8b run. During most of the latter experiment, when running at 10 nA with the 50-μm diamond radiator, a flux of 10 MHz was reached. Towards the end, tests were made with even higher rates. The g8b experiment is still being calibrated, and no data are yet available to evaluate the effects in terms of K^+ identification or Λ - Σ^0 separation. The total rate on the target is not a linear function of the flux in the tagger, and a higher rate will create significantly more accidentals (see section 4.1). We have used 10 MHz for our estimates, although this may be somewhat optimistic for the higher E_γ bins where the coherent peak has a larger tail, increasing the total rate in the tagger.

The tagger is the limiting factor for our event rate. Due to strong collimation, the accidentals in CLAS will not be a problem. The g8b experiment was run with a single-track trigger. The nucleon density for LD_2 is somewhat higher than for LH_2 ($\rho = 162\ mg/cm^3$

vs 71 mg/cm^3, giving a target thickness of 6.5 g/cm^2). The charge is the same, however, and we do not expect an increase in the electromagnetic background. The less significant hadronic background will increase, but by less than a factor of two because the neutron cross sections are lower than those for the proton. With the lower torus field, more tracks may reach region 2 of the drift chamber, but this is not a limiting factor.

A fraction of the beam time allocated for linear polarization, 20% in our estimate, will have to be run with an amorphous carbon radiator, for normalization purposes. The remaining time will be divided equally between two settings (PERP and PARA) where the beam polarization is rotated by 90° in φ. The time required for the runs with the amorphous radiator has been included in the estimates of our statistical uncertainties (see Figs. 30 and 31 below), but not in the rates presented in Table 7 below.

4.3.4 Circular polarization

The part of the proposed experiment using circular polarization can be compared directly with g10. Our assumption for the rate estimate is that we will run at the same luminosity. Using the same radiator, this means that due to our longer target ($\frac{40}{24}$), the beam current will be 40% lower. The new rates are thus simply the g10 rates multiplied by the acceptance ratio for each bin (see Table 6). Both the yields predicted for this experiment, corresponding to 15 allocated beam days, and the yields from the low-field part of g10 are shown in Fig. 25.

The g10 run used little collimation of the photon beam, keeping down the total rate in the tagger. Should the electromagnetic (e^+e^-) background in CLAS turn out to be larger than expected, it is possible to make the collimation more restrictive. If, on the other hand, the background turns out to be lower than expected, it will be possible to increase the beam current somewhat. With a lower torus field it is likely that the occupancies in Region 2 of the drift chambers will be higher, but the crucial point is to keep the Region-1 occupancies at a reasonable level. In terms of background, we will also benefit from the lower photon endpoint energy (2.3 vs 3.6 GeV). During the low-field part of g10, 4.71 billion production triggers

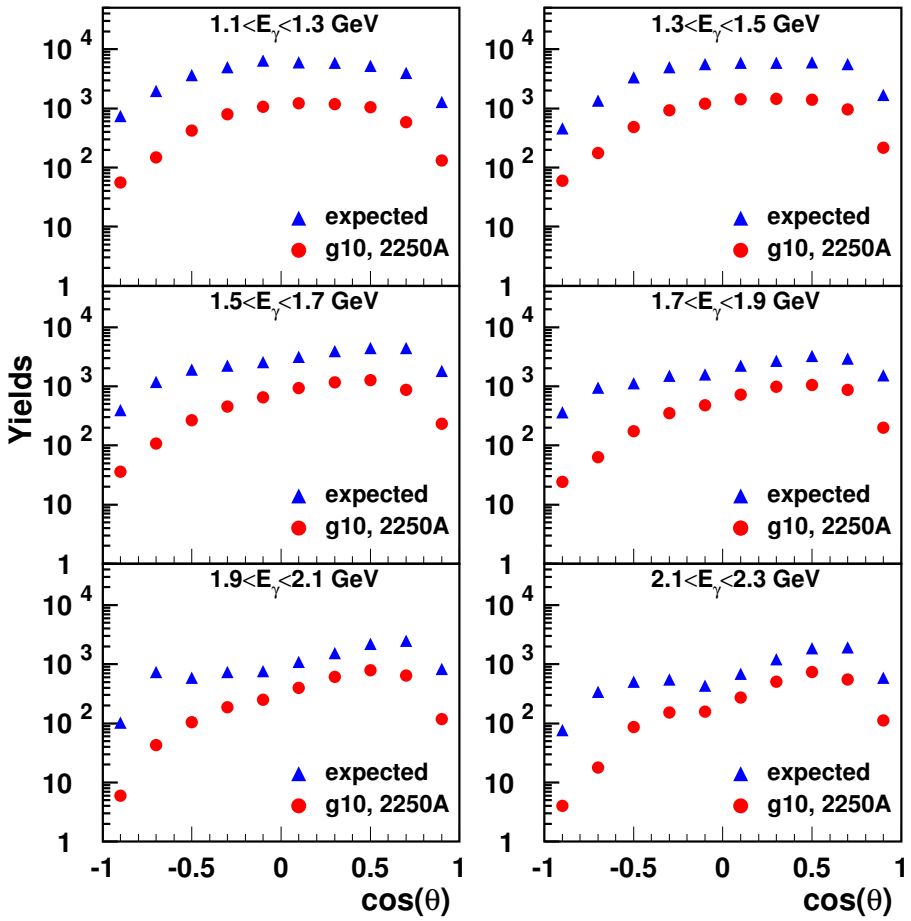

Figure 25: Predicted yields for the $\vec{\gamma}n \to K^0_s\Lambda$ channel, using circular photon polarization, shown as function of $cos(\theta^{cm}_K)$ and compared with g10 low-field data. Both correspond to 15 allocated beam days. The uncertainties in predictions for the two most backward bins are large at high E_γ, but the improvement in kinematic coverage is evident.

were collected, a significant fraction of which came from photons below the Λ threshold. By excluding tagger T-counters 42 through 61, we will thus significantly lower the dead time.

As shown in section 3.2, about 30,000 $K^0_s\Lambda$ and 20,000 $K^0_s\Sigma^0$ quasifree events were reconstructed using the g10 low-field data, before application of CLAS fiducial cuts. Only a small fraction of these came from photons with energies above 2.3 GeV (see Fig. 19).

In addition to the 2100 reconstructed $K^0_s\Lambda$ and 1400 $K^0_s\Sigma^0$ events per allocated beam

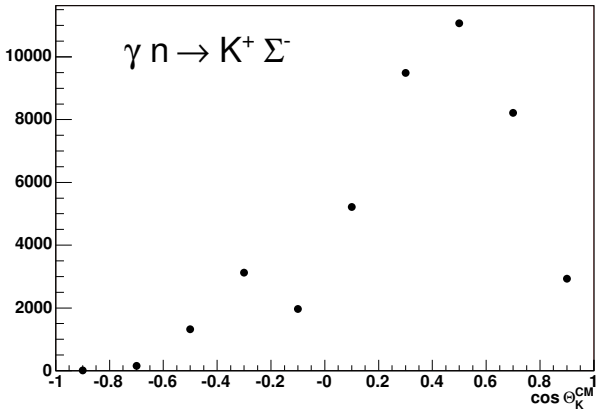

Figure 26: Preliminary g10 low-field yields for $\gamma n \to K^+\Sigma^-$ before background subtraction. With only fiducial and missing-momentum cuts applied, the background is about 50%.

day, rates for other g10 channels include close to 1000 $K^+\Sigma^-(1385)$ events per day. This comparatively high rate results mainly from the fact that only one K^0 out of three decays to $\pi^+\pi^-$ and that the acceptance is better for the K^+ than the K^0_s. Also, the rate for the three-particle final state of the $K^+\Sigma^-$ channel is comparable to those for $K^0_s\Lambda$ and $K^0_s\Sigma^0$, despite the fact that detection of a neutron is required. The challenge in this channel is to deal with the background, for instance from $\gamma n \to n\pi^+\pi^-$. This is in contrast to the Λ and Σ^0 channels, where the background is at the percent level. The final g2 analysis for the $K^+\Sigma^-$ channel also shows a small background [58]. Very preliminary results from an analysis by Rossi *et al.* [61] demonstrate the statistics in g10. However, no background subtraction has been made for the yields shown in Figure 26, where the background is at the 50% level. This may improve as cuts are refined.

The cross section is lower for rescattering than for quasifree reactions. But although it is small for low spectator momenta and high photon energies, it still makes up a significant fraction of the total cross section. In the $K^0_s\Lambda$ channel, at least 20% might be reasonable estimate.

E_γ (GeV)	g10	Circular polarization	Linear polarization
1.1 - 1.3	440	2680	11600
1.3 - 1.5	550	2730	13700
1.5 - 1.7	400	1740	9710
1.7 - 1.9	330	1210	7860
1.9 - 2.1	210	740	5320
2.1 - 2.3	170	540	4300
total	2100	9640	N/A

Table 7: Rates for the $\gamma n \to K^0_s\Lambda$ reaction (in events per allocated beam day) estimated from g10 data, corrected for the photon flux, target geometry, and the acceptance ratio for the two configurations. The last of these was based on a -1500 A (reversed polarity) main torus current. Only events that are correctly reconstructed in the CLAS are included. With linear photon polarization, each setting is run separately. The column for linear polarization does not include any data using an amorphous radiator.

4.3.5 Rates

Table 7 shows our model-independent event rate estimates for the $\vec{\gamma}n \to K^0_s\Lambda$ channel for each E_γ bin. The linearly polarized settings will be run separately. About 20% of the time an amorphous radiator will be used for normalization purposes. For the circular polarization, the abundance of events at low E_γ will compensate for the drop in circular photon polarization, and will be valuable for our rescattering studies. The most important improvement, will result from the fact that the acceptance will be much flatter in $\cos(\theta^{cm}_K)$ using the proposed main-torus current. This redistributes our statistical uncertainties in a more favorable way (see Figs. 30 and 31 below), which is very significant because our systematic uncertainties are relatively small. By extending the measurement to forward and backward angles, we will increase the effective number of data points measured in the experiment, and they will cover a wider kinematic range.

4.4 Determination of polarization observables and their statistical uncertainties from the experimental data

The extraction of polarization observables for quasifree KY production on the neutron from the experimental data is based on Eq. 12 [21]. For each $(E_\gamma, \cos(\theta_K^{cm}))$ bin, the normalized yield can be expressed as

$$\begin{aligned} \frac{4\pi}{N_0}\frac{dN}{d\varphi \sin\theta d\theta} &= \{1 - P_{lin}\Sigma\cos 2\varphi \\ &+P_{x'}\left(-P_{lin}O_{x'}\sin 2\varphi - P_\odot C_{x'}\right) \\ &-P_{y'}\left(-P + P_{lin}T\cos 2\varphi\right) \\ &-P_{z'}\left(P_{lin}O_{z'}\sin 2\varphi + P_\odot C_{z'}\right)\}, \end{aligned} \tag{12}$$

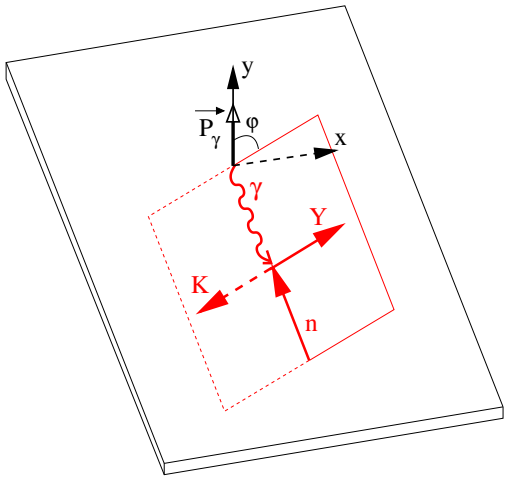

Figure 27: Definition of the φ angle. The primed coordinate system is shown in Figure 1. The z' axis points along the kaon momentum, the y' axis is perpendicular to the reaction plane and defined by $\vec{p_\gamma} \times \vec{p_K}$. The x' axis is in the reaction plane and completes a right-handed coordinate system.

where N is the number of events in a solid angle $d\varphi \sin\theta d\theta$, N_0 is the total number of events for the $(E_\gamma, \cos(\theta_K^{cm}))$ bin (the unpolarized rate), φ is the angle between the photon polarization vector and the reaction plane, as shown in Fig. 27, and $P_{x',y',z'} = \alpha \cos\theta_{p_{x',y',z'}}$.

Here, $\alpha = 0.642 \pm 0.013$ is the self-analyzing power of the Λ in its decay to $p\pi^-$. The asymmetries can be analyzed either by a fit to a distribution differential in φ and θ or to one that is integrated over one or both of them. The first approach is difficult without very large statistics, but both of the latter will be used in the final analysis since they have somewhat different systematic uncertainties. The value that is usually quoted as the statistical uncertainty for an asymmetry, corresponding to its value at zero, is independent of the choice of method. Strictly speaking, this is an upper limit, but the uncertainty is not significantly smaller even when the asymmetry is large. It will be derived here using integration over both angles. This approach is the most straightforward, and the one that is least sensitive to final-state interactions.

4.4.1 Determination of the beam-spin asymmetry Σ

For a linearly polarized photon beam, Eq. 12 becomes

$$\frac{2\pi}{N_0}\frac{dN}{d\varphi} = 1 - P_{lin}\Sigma\cos 2\varphi. \tag{13}$$

We define $N_1^{\parallel}$, $N_1^{\perp}$, $N_2^{\parallel}$, and $N_2^{\perp}$ according to Fig. 28.

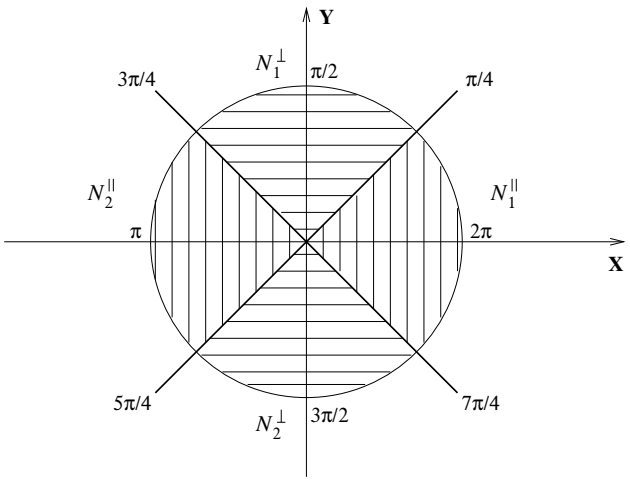

Figure 28: Definition of the four quadrants in φ, which is the angle between the reaction plane and the polarization vector of the photon, used in the extraction of Σ and T.

$$N_1^{\parallel} = N_0 \int_{\frac{7\pi}{4}}^{\frac{\pi}{4}} (1 - P_{lin}\Sigma \cos 2\varphi) d\varphi = N_0(\frac{\pi}{2} - P_{lin}\Sigma) \quad (14)$$

$$N_1^{\perp} = N_0 \int_{\frac{\pi}{4}}^{\frac{3\pi}{4}} (1 - P_{lin}\Sigma \cos 2\varphi) d\varphi = N_0(\frac{\pi}{2} + P_{lin}\Sigma) \quad (15)$$

$$N_2^{\parallel} = N_0 \int_{\frac{3\pi}{4}}^{\frac{5\pi}{4}} (1 - P_{lin}\Sigma \cos 2\varphi) d\varphi = N_0(\frac{\pi}{2} - P_{lin}\Sigma) \quad (16)$$

$$N_1^{\perp} = N_0 \int_{\frac{5\pi}{4}}^{\frac{7\pi}{4}} (1 - P_{lin}\Sigma \cos 2\varphi) d\varphi = N_0(\frac{\pi}{2} + P_{lin}\Sigma) \quad (17)$$

Thus

$$\begin{aligned} N^{\parallel} &= N_1^{\parallel} + N_2^{\parallel} = 2N_0(\frac{\pi}{2} - P_{lin}\Sigma), \quad (18) \\ N^{\perp} &= N_1^{\perp} + N_2^{\perp} = 2N_0(\frac{\pi}{2} + P_{lin}\Sigma). \end{aligned}$$

We can then construct the asymmetry

$$\frac{N^{\perp} - N^{\parallel}}{N^{\perp} + N^{\parallel}} = \frac{2P_{lin}\Sigma}{\pi}. \quad (19)$$

Therefore, Σ and its statistical uncertainty $\delta\Sigma$ are determined from

$$\Sigma = \frac{\pi}{2P_{lin}} \frac{N^{\perp} - N^{\parallel}}{N^{\perp} + N^{\parallel}}, \quad (20)$$

$$\delta\Sigma = \frac{\pi}{2P_{lin}} \frac{1}{\sqrt{N^{\perp} + N^{\parallel}}}, \quad (21)$$

where $N^{\perp} + N^{\parallel} = N_0$ is the total number of unpolarized events in a given kinematic bin $(E_\gamma, \cos(\theta_K^{cm}))$.

4.4.2 Determination of the recoil polarization P

The recoil polarization can be determined in an experiment either with a linearly or circularly polarized photon beam. We shall do both, but let us here consider the case of linearly

polarized photons, for which Eq. 12 becomes

$$\frac{4\pi}{N_0}\frac{dN}{d\varphi \sin\theta_{y'} d\theta_{y'}} = 1 - P_{lin}\Sigma\cos 2\varphi + \alpha\cos\theta_{y'}(P - P_{lin}T\cos 2\varphi), \quad (22)$$

where $\cos\theta_{y'}$ is the y-direction cosine of the 3-momentum vector of the decay proton in the rest frame of the Λ. We define N^+, N^- as

$$N^+ = \int_0^{2\pi}\int_0^{\frac{\pi}{2}} \frac{dN}{d\varphi \sin\theta_{y'} d\theta_{y'}} d\varphi \sin\theta_{y'} d\theta_{y'} = N_0(1 + \frac{\alpha P}{2}), \quad (23)$$

$$N^- = \int_0^{2\pi}\int_{\frac{\pi}{2}}^{\pi} \frac{dN}{d\varphi \sin\theta_{y'} d\theta_{y'}} d\varphi \sin\theta_{y'} d\theta_{y'} = N_0(1 - \frac{\alpha P}{2}). \quad (24)$$

We can then construct the asymmetry

$$\frac{N^+ - N^-}{N^+ + N^-} = \frac{\alpha P}{2}. \quad (25)$$

The recoil polarization P and its statistical uncertainty δP are thus determined

$$P = \frac{2}{\alpha}\frac{N^+ - N^-}{N^+ + N^-} \quad (26)$$

$$\delta P = \frac{2}{\alpha}\frac{1}{\sqrt{N^+ + N^-}}, \quad (27)$$

where $N^+ + N^- = N_0$ is the total number of unpolarized events in a given kinematic bin $(E_\gamma, \cos(\theta_K^{cm}))$.

4.4.3 Determination of the target asymmetry T

The target asymmetry T will be determined using linearly polarized photon beams. We use Eq. 22 and define $N^{\parallel +}$, $N^{\parallel -}$, $N^{\perp +}$, and $N^{\perp -}$ as

$$N^{\parallel +} = \int_{\frac{7\pi}{4}}^{\frac{\pi}{4}}\int_0^{\frac{\pi}{2}} \frac{dN}{d\varphi \sin\theta_{y'} d\theta_{y'}} d\varphi \sin\theta_{y'} d\theta_{y'} + \int_{\frac{3\pi}{4}}^{\frac{5\pi}{4}}\int_0^{\frac{\pi}{2}} \frac{dN}{d\varphi \sin\theta_{y'} d\theta_{y'}} d\varphi \sin\theta_{y'} d\theta_{y'} =$$

$$= \pi + \frac{\pi\alpha P}{2} - 2P_{lin}\Sigma - \frac{\alpha P_{lin} T}{2}, \tag{28}$$

$$N^{\parallel -} = \int_{\frac{7\pi}{4}}^{\frac{\pi}{4}} \int_{\frac{\pi}{2}}^{\pi} \frac{dN}{d\varphi \sin\theta_{y'} d\theta_{y'}} d\varphi \sin\theta_{y'} d\theta_{y'} + \int_{\frac{3\pi}{4}}^{\frac{5\pi}{4}} \int_{\frac{\pi}{2}}^{\pi} \frac{dN}{d\varphi \sin\theta_{y'} d\theta_{y'}} d\varphi \sin\theta_{y'} d\theta_{y'} =$$

$$= \pi - \frac{\pi\alpha P}{2} - 2P_{lin}\Sigma + \frac{\alpha P_{lin} T}{2}, \tag{29}$$

$$N^{\perp +} = \int_{\frac{\pi}{4}}^{\frac{3\pi}{4}} \int_{0}^{\frac{\pi}{2}} \frac{dN}{d\varphi \sin\theta_{y'} d\theta_{y'}} d\varphi \sin\theta_{y'} d\theta_{y'} + \int_{\frac{5\pi}{4}}^{\frac{7\pi}{4}} \int_{0}^{\frac{\pi}{2}} \frac{dN}{d\varphi \sin\theta_{y'} d\theta_{y'}} d\varphi \sin\theta_{y'} d\theta_{y'} =$$

$$= \pi + \frac{\pi\alpha P}{2} + 2P_{lin}\Sigma + \frac{\alpha P_{lin} T}{2}, \tag{30}$$

$$N^{\perp -} = \int_{\frac{\pi}{4}}^{\frac{3\pi}{4}} \int_{\frac{\pi}{2}}^{\pi} \frac{dN}{d\varphi \sin\theta_{y'} d\theta_{y'}} d\varphi \sin\theta_{y'} d\theta_{y'} + \int_{\frac{5\pi}{4}}^{\frac{7\pi}{4}} \int_{\frac{\pi}{2}}^{\pi} \frac{dN}{d\varphi \sin\theta_{y'} d\theta_{y'}} d\varphi \sin\theta_{y'} d\theta_{y'} =$$

$$= \pi - \frac{\pi\alpha P}{2} + 2P_{lin}\Sigma - \frac{\alpha P_{lin} T}{2}. \tag{31}$$

Therefore, T and its statistical uncertainty are determined from

$$T = \frac{2\pi}{\alpha P_{lin}} \frac{(N^{\perp +} + N^{\parallel -}) - (N^{\perp -} + N^{\parallel +})}{N^{\perp +} + N^{\parallel -} + N^{\perp -} + N^{\parallel +}}, \tag{32}$$

$$\delta T = \frac{2\pi}{\alpha P_{lin}} \frac{1}{\sqrt{N^{\perp +} + N^{\parallel -} + N^{\perp -} + N^{\parallel +}}}, \tag{33}$$

where $N^{\perp +} + N^{\parallel -} + N^{\perp -} + N^{\parallel +} = N_0$ is the total number of unpolarized events in a given kinematic bin $(E_\gamma, \cos(\theta_K^{cm}))$.

4.4.4 Determination of the double-polarization observables $O_{x'}$ and $O_{z'}$

Determination of these two observables requires linearly polarized photon beams. Let us first consider $O_{x'}$. Equation 12 then becomes

$$\frac{4\pi}{N_0} \frac{dN}{d\varphi \sin\theta_{x'} d\theta_{x'}} = 1 - P_{lin}\Sigma \cos 2\varphi - \alpha P_{lin} O_{x'} \sin 2\varphi \cos\theta_{x'}. \tag{34}$$

We define N^{L+}, N^{L-}, N^{R+}, and N^{R-} according to Fig. 29:

$$N^{R+} = \int_{0}^{\frac{\pi}{2}} \int_{0}^{\frac{\pi}{2}} \frac{dN}{d\varphi \sin\theta_{x'} d\theta_{x'}} d\varphi \sin\theta_{x'} d\theta_{x'} + \int_{\pi}^{\frac{3\pi}{2}} \int_{0}^{\frac{\pi}{2}} \frac{dN}{d\varphi \sin\theta_{x'} d\theta_{x'}} d\varphi \sin\theta_{x'} d\theta_{x'} =$$

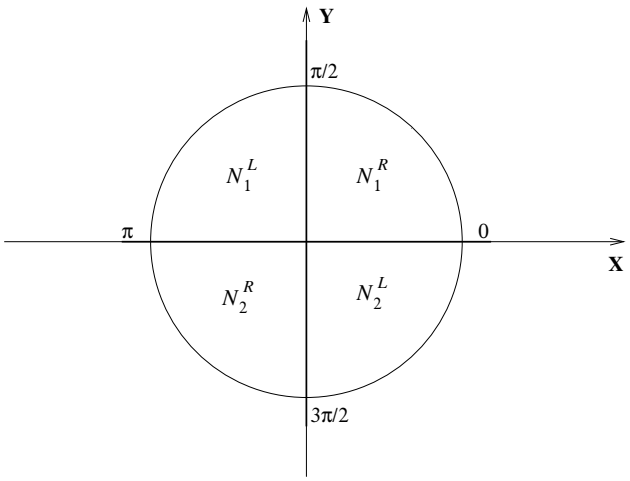

Figure 29: Definition of the four quadrants in φ, which is the angle between the polarization vector of the photon and the reaction plane, used in the extraction of $O_{x'}$ and $O_{z'}$.

$$= 2(\frac{\pi}{2} - \frac{\alpha P_{lin} O_{x'}}{2}), \tag{35}$$

$$N^{R-} = \int_0^{\frac{\pi}{2}} \int_{\frac{\pi}{2}}^{\pi} \frac{dN}{d\varphi \sin\theta_{x'} d\theta_{x'}} d\varphi \sin\theta_{x'} d\theta_{x'} + \int_{\pi}^{\frac{3\pi}{2}} \int_{\frac{\pi}{2}}^{\pi} \frac{dN}{d\varphi \sin\theta_{x'} d\theta_{x'}} d\varphi \sin\theta_{x'} d\theta_{x'} =$$

$$= 2(\frac{\pi}{2} + \frac{\alpha P_{lin} O_{x'}}{2}), \tag{36}$$

$$N^{L+} = \int_{\frac{\pi}{2}}^{\pi} \int_0^{\frac{\pi}{2}} \frac{dN}{d\varphi \sin\theta_{x'} d\theta_{x'}} d\varphi \sin\theta_{x'} d\theta_{x'} + \int_{\frac{3\pi}{2}}^{2\pi} \int_0^{\frac{\pi}{2}} \frac{dN}{d\varphi \sin\theta_{x'} d\theta_{x'}} d\varphi \sin\theta_{x'} d\theta_{x'} =$$

$$= 2(\frac{\pi}{2} + \frac{\alpha P_{lin} O_{x'}}{2}), \tag{37}$$

$$N^{L-} = \int_{\frac{\pi}{2}}^{\pi} \int_{\frac{\pi}{2}}^{\pi} \frac{dN}{d\varphi \sin\theta_{x'} d\theta_{x'}} d\varphi \sin\theta_{x'} d\theta_{x'} + \int_{\frac{3\pi}{2}}^{2\pi} \int_{\frac{\pi}{2}}^{\pi} \frac{dN}{d\varphi \sin\theta_{x'} d\theta_{x'}} d\varphi \sin\theta_{x'} d\theta_{x'} =$$

$$= (\frac{\pi}{2} - \frac{\alpha P_{lin} O_{x'}}{2}). \tag{38}$$

Thus, one can determine $O_{x'}$ and its statistical uncertainty $\delta O_{x'}$ from

$$O_{x'} = \frac{\pi}{\alpha P_{lin}} \frac{(N^{R-} + N^{L+}) - (N^{R+} + N^{L-})}{N^{R-} + N^{L+} + N^{R+} + N^{L-}}, \tag{39}$$

$$\delta O_{x'} = \frac{\pi}{\alpha P_{lin}} \frac{1}{\sqrt{N^{R-} + N^{L+} + N^{R+} + N^{L-}}}. \tag{40}$$

In a similar way one can determine $O_{z'}$ and $\delta O_{z'}$ from

$$O_{z'} = \frac{\pi}{\alpha P_{lin}} \frac{(N^{R-} + N^{L+}) - (N^{R+} + N^{L-})}{N^{R-} + N^{L+} + N^{R+} + N^{L-}}, \tag{41}$$

$$\delta O_{z'} = \frac{\pi}{\alpha P_{lin}} \frac{1}{\sqrt{N^{R-} + N^{L+} + N^{R+} + N^{L-}}}, \tag{42}$$

where the upper labels "-" and "+" correspond to integration over the negative and the positive intervals of $\cos\theta_{z'}$, respectively.

4.4.5 Determination of the double-polarization observables $C_{x'}$ and $C_{z'}$

Determination of these two observables requires circularly polarized photon beams. Let us first consider $C_{x'}$. Here, Eq. 12 becomes

$$\frac{2}{N_0}\frac{dN}{\sin\theta_{x'} d\theta_{x'}} = 1 - \alpha \cos\theta_{x'} P_\odot C_{x'}. \tag{43}$$

If we label with N^+ and N^- the number of events for a given range of $\cos\theta_{x'}$ corresponding to positive and negative beam helicity states, respectively, the observable $C_{x'}$ can be obtained from the asymmetry

$$C_{x'} = \frac{2}{\alpha P_\odot} \frac{(N^{+-} + N^{-+}) - (N^{++} + N^{--})}{N^{+-} + N^{-+} + N^{++} + N^{--}}, \tag{44}$$

where $N^{+-} + N^{-+} + N^{++} + N^{--} = N_0$ is the total number of unpolarized events for a given kinematic bin $(E_\gamma, \cos(\theta_K^{cm}))$. The first upper label in the above notation shows the helicity state of the circularly polarized photon beam, while the second upper label corresponds to the interval of $\cos\theta_{x'}$ over which the integration has been done ("+" labels integration over 0 to -1 and "-" labels integration over -1 to 0). The statistical uncertainty $\delta C_{x'}$ is determined from

$$\delta C_{x'} = \frac{2}{\alpha P_\odot} \frac{1}{\sqrt{N^{+-} + N^{-+} + N^{++} + N^{--}}}. \tag{45}$$

The double-polarization observable $C_{z'}$ and its statistical uncertainty $\delta C_{z'}$ can be calculated from analogous expressions, integrating over $\cos\theta_{z'}$.

4.5 Systematic uncertainties

A summary of systematic uncertainties for this experiment is given in Table 8.

Systematic uncertainty	Circular polarization	Linear polarization
α[1]	2%	2%
background subtraction[2]	$< 5\%$	$< 5\%$
beam polarization	2%	3-4%
total	6%	6-7%

Table 8: Systematic uncertainties: [1] not for Σ; [2] for the $K^0_s\Lambda$ and $K^0_s\Sigma^0$ channels only.

The following sources of systematic uncertainties are common to both the linearly and circularly polarized parts of the experiment:

- The uncertainty of the value of the self-analyzing power of the Λ hyperon α. In the PDG this value is listed as $\alpha = 0.642 \pm 0.013$, corresponding to an uncertainty of 2%.

- The uncertainty of the extracted quasifree $K\Lambda$ yields due to background contributions. There are two types of contributions which have to be considered:

  - the contributions from other physics channels. The yield extraction will be mainly based on the $K\Lambda$ missing-mass distribution, where the spectator-proton mass peak can be clearly identified. Background subtraction will be performed in order to remove events from the tail of the distribution. The systematic uncertainty of the yield extraction due to this background can be reduced, as discussed in section 3.2 and exemplified by our analysis of the g10 data. We estimate this uncertainty to

be 2%. With the proposed torus current of -1500 A, this uncertainty may increase somewhat due to the decreased momentum resolution.

- the contribution from non-quasifree events (FSI). As described in section 3.2, we select the quasifree channels by making a cut on the momentum distribution of the missing proton (see Fig. 15). Thus, our sample maight contain rescattering events. The contribution of rescattering events can be estimated ia various ways, which are also discussed in section 3.2. For a very conservative estimate, one can extrapolate the high-momentum tail of the missing-proton momentum distribution under the spectator-momentum peak. This can be done either by using a model or just assuming a linear dependence. The background contribution itself, estimated using the latter method , is at the level of 5%. This background can be subtracted from the yield in each kinematic bin, thus reducing the systematic uncertainty to the uncertainty in the subtraction. The subtraction will be optimized through our studies of the final-state interactions (see section 3.4).

  A very conservative estimate of the total systematic uncertainty due to background subtraction is thus less than 5%.

- The uncertainty due to bin centering will be small.

4.5.1 Linearly polarized photon beam

The following sources of systematic uncertainties pertain to the linearly polarized part of the experiment:

- Determination of the linear polarization of the photon beam $\frac{\delta P_{lin}}{P_{lin}}$. The linear polarization of the photons will be determined by fitting a model to the experimental energy distributions, as was done for g8b where this uncertainty was found to be 3 - 4%. We take this estimate as the expected uncertainty of the photon polarization for our proposed experiment.

- The CLAS acceptance. As discussed in section 4.4, we obtain our double-polarization observables by integrating yields over quadrants in φ (Lab System) and/or halves of the $\cos\theta_{p_{y'}}$ ranges in the Λ rest frame. Thus, any differences in the CLAS acceptance in these angular ranges can produce false asymmetries.

  Differences in φ acceptance will be studied with high statistics and corrected using the integrated $K\Lambda$ yields over these φ quadrants, and by rotating the linear polarization in the experiment by 90°. This should lead to results independent of the φ-acceptance. Therefore, we do not anticipate any significant systematic uncertainty from this source.

  This leaves only two observables, P and T, which can be dependent on the CLAS acceptance in terms of $\cos\theta_{p_{y'}}$. The latter would, however, only contribute to false asymmetries if, for each kinematic bin $(E_\gamma, \cos(\theta_K^{cm}))$, the CLAS acceptance for $\cos\theta_{p_{y'}} > 0$ differs from that for $\cos\theta_{p_{y'}} < 0$. This can happen only if the two halves of the cosine interval correspond to different kinematic coverage of $p_{p,LS}$ and $\theta_{p,LS}$. For unpolarized and circularly polarized beams, the reaction plane (to which the y'-axis is perpendicular) does not have a preferred φ-orientation, and in any statistically significant sample the condition is satisfied by symmetry. In order to make sure that it is also satisfied for the linearly polarized case, we use a realistic GSIM simulation of the $K_s^0\Lambda$ reaction, assuming an unpolarized Λ decay. For each of the 60 kinematics bins of interest, we constructed the asymmetry $\frac{N^+-N^-}{N^++N^-}$, which turned out to be consistent with zero. This is because the two halves of the $\cos\theta_{p_{y'}}$ interval correspond to exactly the same ranges in $p_{p,LS}$ and $\theta_{p,LS}$. Thus, we do not expect any significant systematic uncertainty due to the CLAS $\cos\theta_{p_{y'}}$ acceptance.

4.5.2 Circularly polarized photon beam

Circular polarization will be used to determine the observables $C_{x'}$, $C_{z'}$, and P. We anticipate the following sources of systematic uncertainties:

- Determination of the photon circular polarization $\frac{\delta P_\odot}{P_\odot}$. This uncertainty depends on the uncertainty of the polarization of electron beam δP_{e^-}, which will be determined using the Møller polarimeter in Hall B. Based on previous experiments requiring Møller measurements (such as g1c, g3, e1-6, and eg1b), we estimate this uncertainty to be around 2%.

- The CLAS acceptance. Since we are going to use an acceptance-independent method to determine $C_{x'}$ and $C_{z'}$, we will have no such systematic uncertainty.

- Instrumental asymmetries, beam position, and electron-beam charge asymmetry. These will be studied, and corrected for, using the total KY yields (integrated over all the angles of the proton from the Λ decay). For this case, the beam-helicity asymmetry $\frac{N^+ - N^-}{N^+ + N^-}$ must be zero. We expect these systematic uncertainties to be negligible.

4.6 Beam time

Our beam-time request is divided into two parts, one requiring a 5-GeV electron beam, and one with a longitudinally polarized 2.4-GeV electron beam. The former will use the coherent-bremsstrahlung facility in Hall B to produce linearly polarized photon beams. Beam time is requested for six settings, each covering 200 MeV of the $1.1 < E_\gamma < 2.3$ range. The latter will produce circularly polarized photons with a regular bremsstrahlung spectrum, covering energies from the Λ threshold up to 2.3 GeV. These are the assumptions used for the counting-rate estimates in Table 6 of section 4.2.

However, as noted in sections 4.1 and 4.2, there is considerable flexibility in the electron-beam energies and polarizations. For the part using circular polarization, energies of up to 3 GeV would be acceptable. For the linearly polarized case, although high beam energies are desirable, the lowest two points can be taken with a 3-GeV beam. This flexibility makes the experiment easy to schedule.

The requested beam time is based on the necessary limits on the statistical uncertainties for the polarization observables in the $\vec{\gamma}n \to K^0_s\Lambda$ channel. These are determined by the sensitivity of the observables, as exemplified by the CSI model predictions for the $D_{13}(1900)$ resonance (see also section 2.2). Both the uncertainties and predictions averaged over the corresponding E_γ bin are shown in Figs. 30 and 31. The uncertainties for the Σ channels, as well as for the Y^* and K^* final states, will be somewaht larger. The focus is mainly on Σ, $O_{x'}$, and $O_{z'}$ for the linearly polarized part and on $C_{x'}$ and $C_{z'}$ for the circularly polarized part. The recoil polarization P can be determined in both parts of the proposed experiment, and its statistical uncertainty can therefore be reduced by combining the data samples and propagating the corresponding systematic uncertainties. The actual value of δP will thus be better than shown in Fig. 30, which is based only on the linearly polarized data sample. We also want to have comparable uncertainties of a given observable over as wide a $\cos(\theta^{cm}_K)$ range as possible for each photon energy.

As can be seen in section 4.4, the statistical uncertainty of each polarization observable for a specific kinematic $(E_\gamma, \cos(\theta_K^{cm}))$ bin is inversely proportional to N_0 (the total number of unpolarized events in this kinematic bin). We know the latter from our rate estimates, based on actual g10 data, corrected for the differences in acceptance, target length, and incoming photon flux (see section 4.3).

In order to achieve the uncertainties shown in Figs. 30 and 31, we require 15 days with circular polarization and $5 + 4 + 5 + 6 + 6 + 7 = 33$ days with linear polarization. The subtotals refer to the six photon energy bins centered at 1.2, 1.4, 1.6, 1.8, 2.0, and 2.2 GeV.

4.6.1 Beam-time request

In terms of 24-hour days with uninterrupted beam time, we request 15 days using a highly polarized 2.4-GeV electron beam for the circularly polarized measurement and 33 days with a 5-GeV electron beam for the linearly polarized measurements.

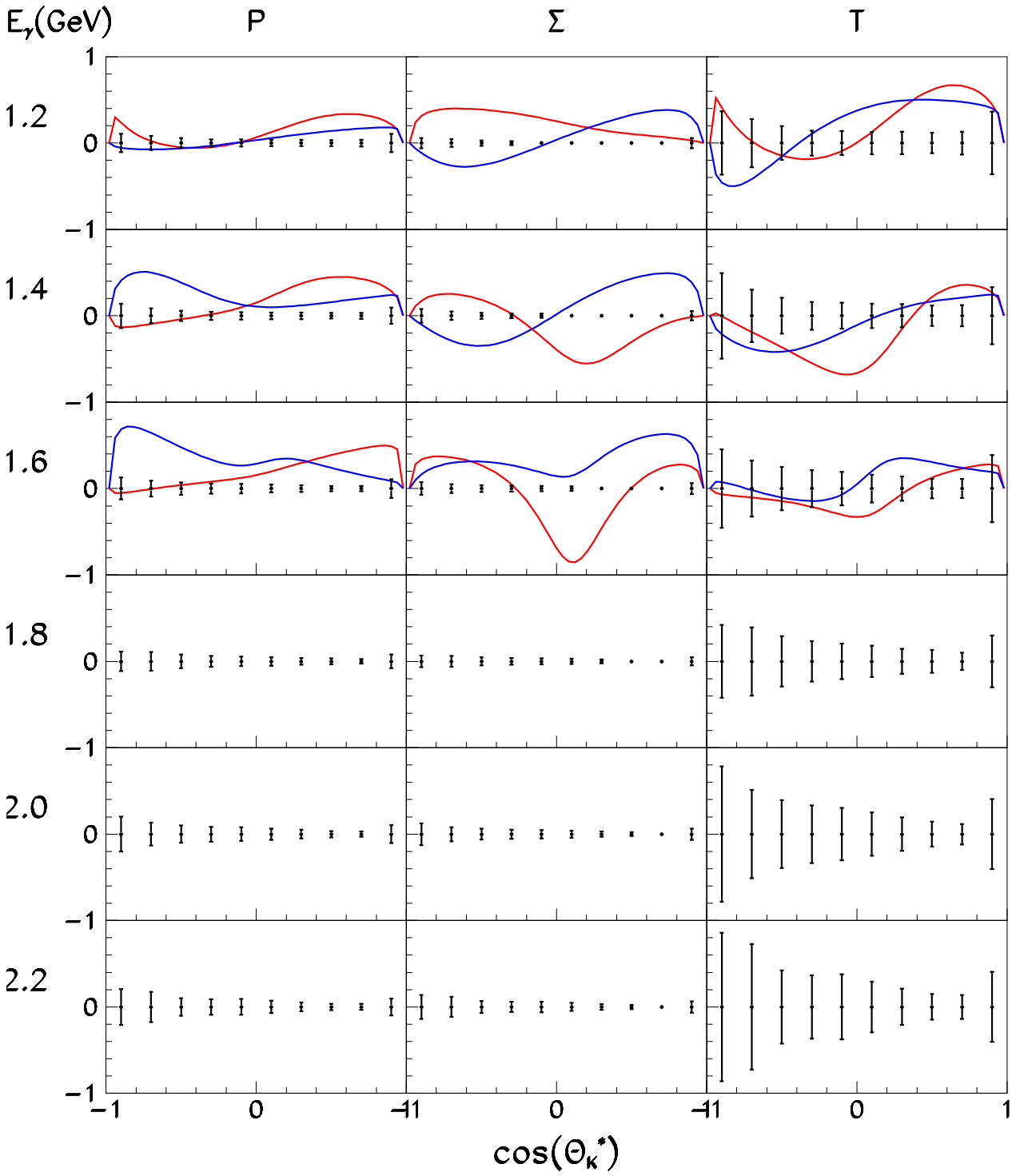

Figure 30: The statistical uncertainties for P, Σ, and T in the $\vec{\gamma}n \to K^0_s\Lambda$ channel with $5+4+5+6+6+7 = 33$ allocated beam days. The predictions of the CSI model (see section 2.2) with (red) and without (blue) the $D_{13}(1900)$ resonance are shown as well.

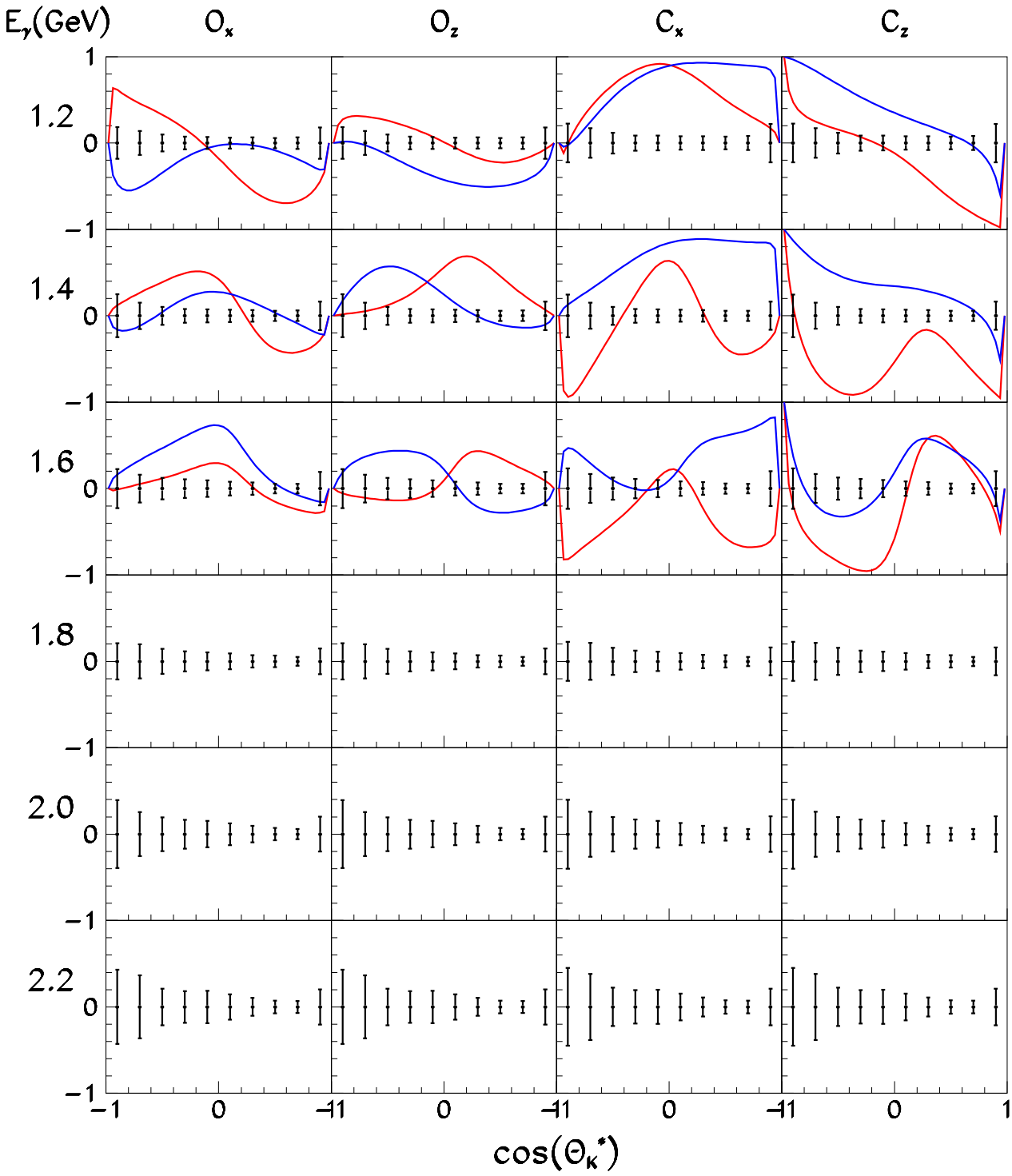

Figure 31: The statistical uncertainties in the $\vec{\gamma}n \to K_s^0\Lambda$ channel for 33 days with linear $(O_{x'}, O_{z'})$ and 15 days with circular polarization $(C_{x'}, C_{z'})$. The predictions of the CSI model (see section 2.2) with (red) and without (blue) the $D_{13}(1900)$ resonance are shown as well.

References

[1] S. Capstick, Phys. Rev. D **34**, 2809 (1986).

[2] R.E. Cutkosky and R.E. Hendrick, Phys. Rev. D **16**, 2902 (1977).

[3] G. Penner and U. Mosel, Phys. Rev. C **66**, 055212 (2002).

[4] G. Penner, Ph.D. thesis, Justus-Liebig University (2002).
http://theorie.physik.uni-giessen.de/html/dissertations.html

[5] V. Shklyar, H. Lenske, and U. Mosel, Phys. Rev. C **72**, 015210 (2005).

[6] A. Waluyo, Ph.D. thesis, The George Washington University, (2005).

[7] J.C. David, C. Fayard, G.H. Lamot, and B. Saghai, Phys. Rev. C **53**, 2613 (1996).

[8] H. Yamamura *et al.*, Phys. Rev. C **61**, 014001 (1999).

[9] T. Mart, C. Bennhold, H. Haberzettl, and L. Tiator, Kaon MAID 2000.
http://www.kph.uni-mainz.de/MAID/kaon/kaonmaid.html

[10] F.X. Lee, T. Mart, C. Bennhold, H. Haberzettl, and L.E. Wright,
Nucl. Phys. **A695**, 237 (2001).

[11] S. Janssen, J. Ryckebusch, W. Van Nespen, D. Debruyne, and T. Van Cauteren,
Eur. Phys. J. **A11**, 105 (2001).

[12] S. Janssen, J. Ryckebusch, D. Debruyne, and T. Van Cauteren,
Phys. Rev. C **65**, 015201 (2001).

[13] S. Janssen, J. Ryckebusch, D. Debruyne, and T. Van Cauteren,
Phys. Rev. C **66**, 035202 (2002).

[14] S. Janssen, Ph.D. thesis, University of Gent (2002).
http://inwpent5.ugent.be/phdthes.html

[15] R. Koniuk and N. Isgur, Phys. Rev. D **21**, 1868 (1980).

[16] S. Capstick, Phys. Rev. D **46**, 2864 (1992).

[17] S. Capstick and W. Roberts, Phys. Rev. D **58**, 074011 (1998).

[18] P. Nadel-Turoński *et al.*, Letter of Intent for Jefferson Lab PAC 29.
http://www.jlab.org/exp_prog/proposals/06/LOI-06-005.pdf

[19] I.S. Barker, A. Donnachie, and J.K. Storrow, Nucl. Phys. **B95**, 347 (1975).

[20] C.G. Fasano, F. Tabakin, and B. Saghai, Phys. Rev. C **46**, 2430 (1992).

[21] G. Knöchlein, D. Dreschsel, and L. Tiator, Z. Phys. **A352**, 327 (1995).

[22] T. Mart, C. Bennhold, and C.E. Hyde-Wright, Phys. Rev. C **51**, 1074(R) (1995).

[23] S. Eidelman *et al.*, Phys. Lett. **B592**, 1 (2004).

[24] M.Q. Tran, Phys. Lett. **B445**, 20 (1998).

[25] K.-H. Glander *et al.*, Eur. Phys. J. **A19**, 251 (2004).

[26] T. Mart and C. Bennhold, Phys. Rev. C **61**, 012201 (1999).

[27] C. Bennhold, A. Waluyo, H. Haberzettl, T. Mart, G. Penner, and U. Mosel, nucl-th/0008024 (2000).

[28] J.W.C. McNabb *et al.*, Phys. Rev. C **69**, 042201 (2004).

[29] R. Bradford *et al.*, Phys. Rev. C **73**, 035202 (2006).

[30] X. Li, L.E. Wright, and C. Bennhold, Phys. Rev. C **45**, 2011 (1992).

[31] O. Maxwell, Phys. Rev. C **69**, 034605 (2004).

[32] A. Salam and H. Arenhövel, Phys. Rev. C **70**, 044008 (2004).

[33] J.-M. Laget, Phys. Rev. C **73**, 044033 (2006).

[34] R. Davis, P. Nadel-Turoński, and B.L. Berman, NSTAR 2005 poster.

[35] K. Miyagawa, T. Mart, C. Bennhold, and W. Glöckle, Phys. Rev. C (accepted, 2006).

[36] R.A. Adelseck and B. Saghai, Phys. Rev. C **42**, 108 (1990).

[37] R. Bradford, Ph.D. thesis, Carnegie Mellon University, (2005), http://www.jlab.org/Hall-B/general/thesis/bradford/

[38] T. Feuster and U. Mosel, Phys. Rev. C textbf58, 457 (1998).

[39] V. Pascalutsa and J.A. Tjon, Phys. Rev. C **61**, 054003 (2000).

[40] R.M. Davidson and R. Workman, Phys. Rev. C **63**, 025210 (2001).

[41] M. Dugger *et al.*, Phys. Rev. Lett. **89**, 222002 (2002).

[42] J.W.C. McNabb, Ph.D. thesis, Carnegie Mellon University (2003). http://www.jlab.org/Hall-B/general/thesis/mcnabb/

[43] G.F. Chew, M.L. Goldberger, F.E. Low, and Y. Yambu, Phys. Rev. **106**, 1345 (1957).

[44] T.P. Vrana, S.A. Dytman, and T.S.H. Lee, Phys. Rep. **328**, 181 (2000).

[45] A. Tkabladze, http://www.jlab.org/~avto/soft/mcevent.html.

[46] D.G Ireland, S. Janssen, and J. Ryckebusch, Nucl. Phys. **A740**, 147 (2004).

[47] W.-T. Chiang, F. Tabakin, T.H.S. Lee, and B. Saghai, Phys. Lett. **B517**, 101 (2001).

[48] T. Corthals, J. Ryckebusch, and T. Van Cauteren, Phys. Rev. C **73**, 045207 (2006).

[49] M. Guidal, J.-M. Laget, and M. Vanderhaegen, Nucl .Phys. **A627**, 645 (1997).

[50] A. Usov and O. Scholten, Phys. Rev. C **72**, 025205 (2005).

[51] J.-M. Laget, Phys. Rep. **69**, 1 (1981).

[52] J.-M. Laget, nucl-th/0603009 (2005).

[53] J.-M. Laget, Phys. Lett. **B259**, 24 (1991).

[54] J.-M. Laget, J. Korean Phys. Soc. **26**, S244 (1993).

[55] B. Carnahan, Ph.D. thesis, Catholic University of Amercia (2003).
http://www.jlab.org/Hall-B/general/thesis/carnahan_thesis.ps

[56] B. Mecking *et al.*, JLab Hall B completed experiment E-89-045,
http://www.jlab.org/exp_prog/proposals/89/PR89-045.pdf

[57] J. Langheinrich, A. Lima, and B.L. Berman, Proc. NSTAR 2005;
CLAS Analysis Note submitted (2005).

[58] I. Niculescu, nucl-ex/0108013; CLAS Analysis Note submitted (2005),
http://www.jlab.org/Hall-B/secure/clas_hadron/analysis_reviews

[59] K. Hicks *et al.*, JLab Hall B completed experiment E-03-113,
http://www.jlab.org/exp_prog/proposals/03/PR03-113.ps

[60] P. Nadel-Turoński and B.L. Berman, g10 CLAS Approved Analysis CAA-HS06-01,
http://www.jlab.org/Hall-B/secure/hadron/proposals

[61] P. Rossi *et al.*, http://www.jlab.org/~rossi/KS.

[62] D. Husmann and W.J. Schwille, Phys. Bl. **44**, 40 (1988).

[63] T. Nakano *et al.*, Nucl. Phys. **A684**, 71c (2001).

[64] R.G.T. Zegers *et al.*, Phys. Rev. Lett. **91**, 092001 (2003).

[65] H. Kohri *et al.*, hep-ex/0602015 (2006).

[66] S. Stepanyan *et al.*, CLAS Note 2005-012.

[67] L. Guo, g11 analysis (2006).

[68] L. Guo and D. Weygand, Proc. NSTAR 2005, hep-ex/0601010 (2006).

[69] Y. Oh and H. Kim, hep-ph/0602112 (2006).

[70] Q. Zhao, J.S. Al-Khalili, and C. Bennhold, Phys. Rev. C **64**, 052201 (2001).

[71] P. Nadel-Turoński and B.L. Berman, Proc. NSTAR 2005.

[72] F.A. Natter *et al.*, Nucl. Intrum. Methods **B211**, 465 (2003).

[73] H. Olsen and L.C. Maximon, Phys. Rev. **114**, 887 (1959).

[74] M. Sumihama *et al.*, Phys. Rev. C **73**, 035214 (2006).

Appendix

Selected results from the coupled-channels calculations for the proton by Bennhold and Waluyo [6].

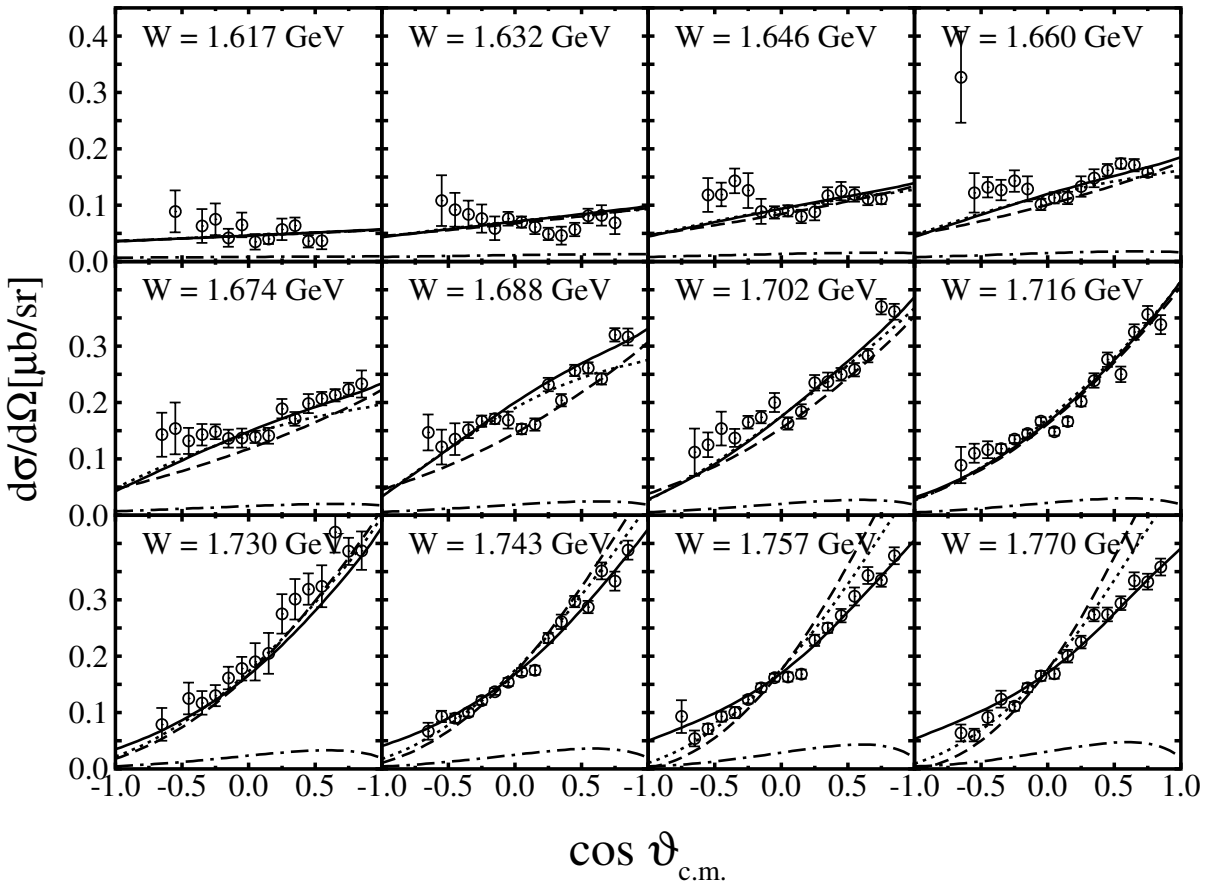

Figure 32: Differential cross sections for $\gamma p \to K^+\Lambda$ at low energies. The solid lines show the full calculation, while the dashed, dotted, and dot-dashed lines show calculations without the $D_{13}(1700)$, $P_{13}(1720)$, and Born contributions, respectively. Data are from Ref. [28].

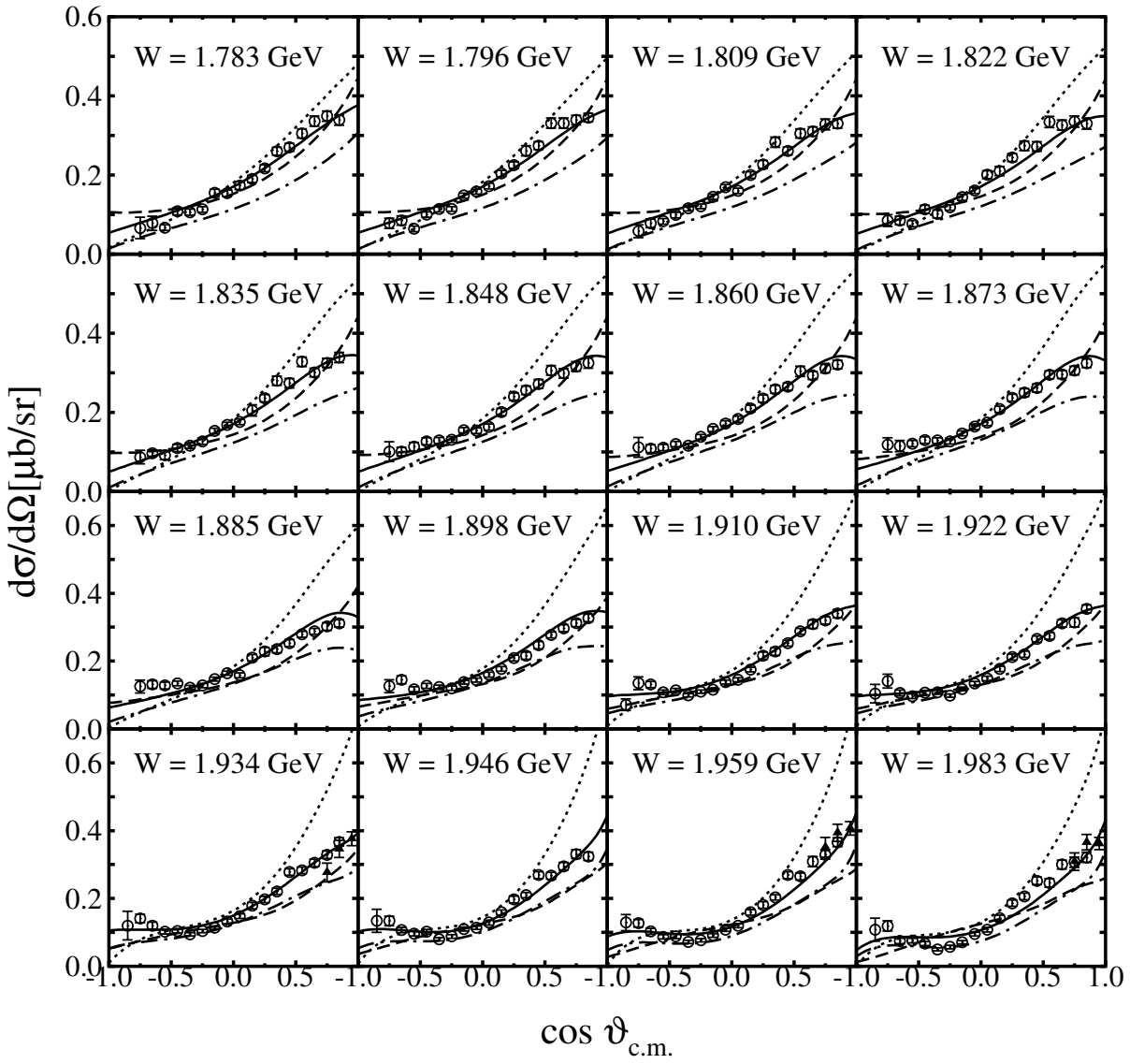

Figure 33: Differential cross sections for $\gamma p \to K^+\Lambda$ at high energies. The solid lines show the full calculation, while the dashed, dotted, and dot-dashed lines show calculations without the $D_{13}(1900)$, $P_{13}(1900)$, and K^* contributions, respectively. Data points marked by open circles are from Ref [28] and the triangles are from Ref. [74].

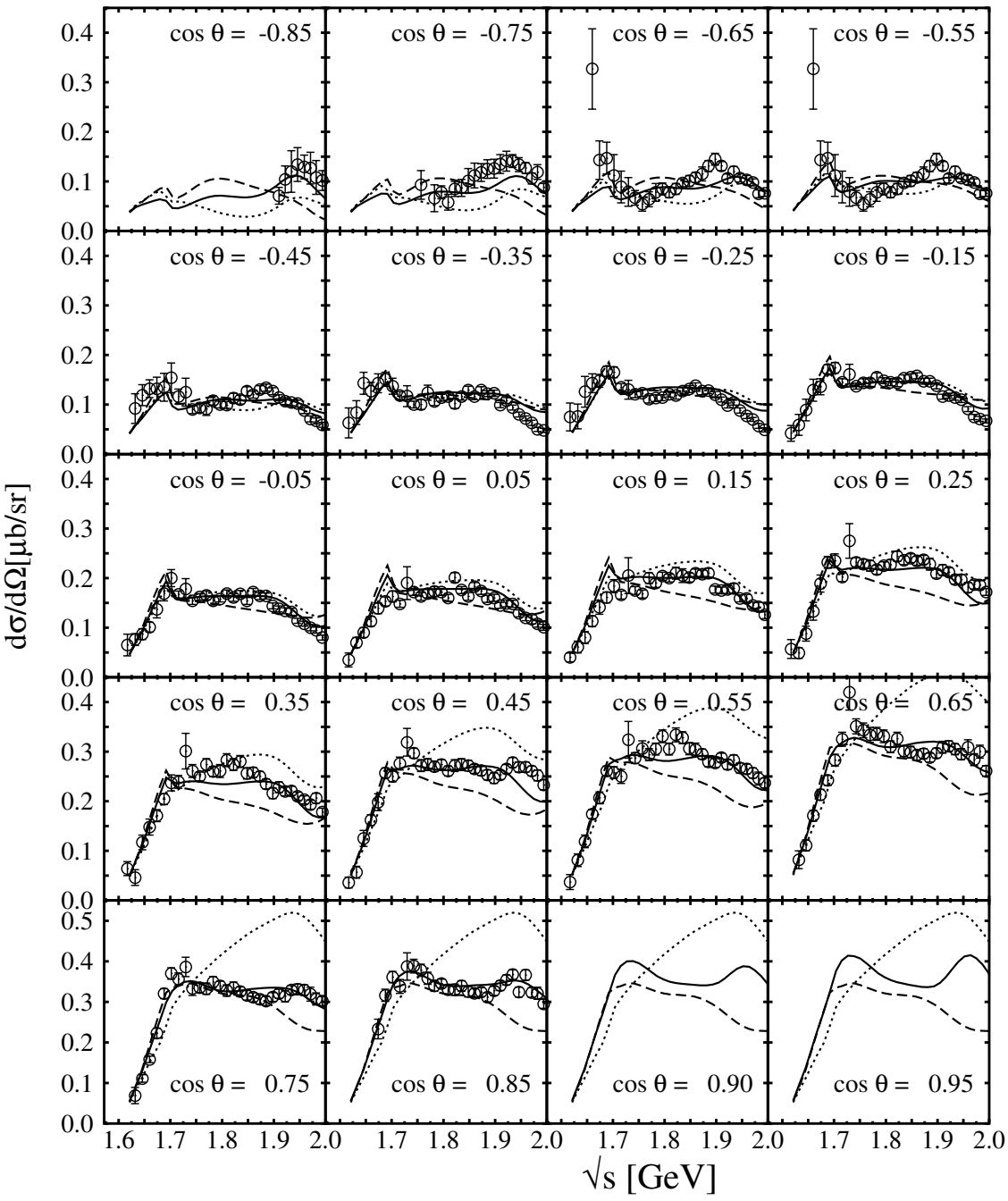

Figure 34: Energy distribution cross sections for $\gamma p \to K^+\Lambda$. The solid lines show the full calculation, while the dashed and dotted lines show calculations without the $D_{13}(1900)$ and $P_{13}(1900)$ respectively. Data are from Ref. [28].

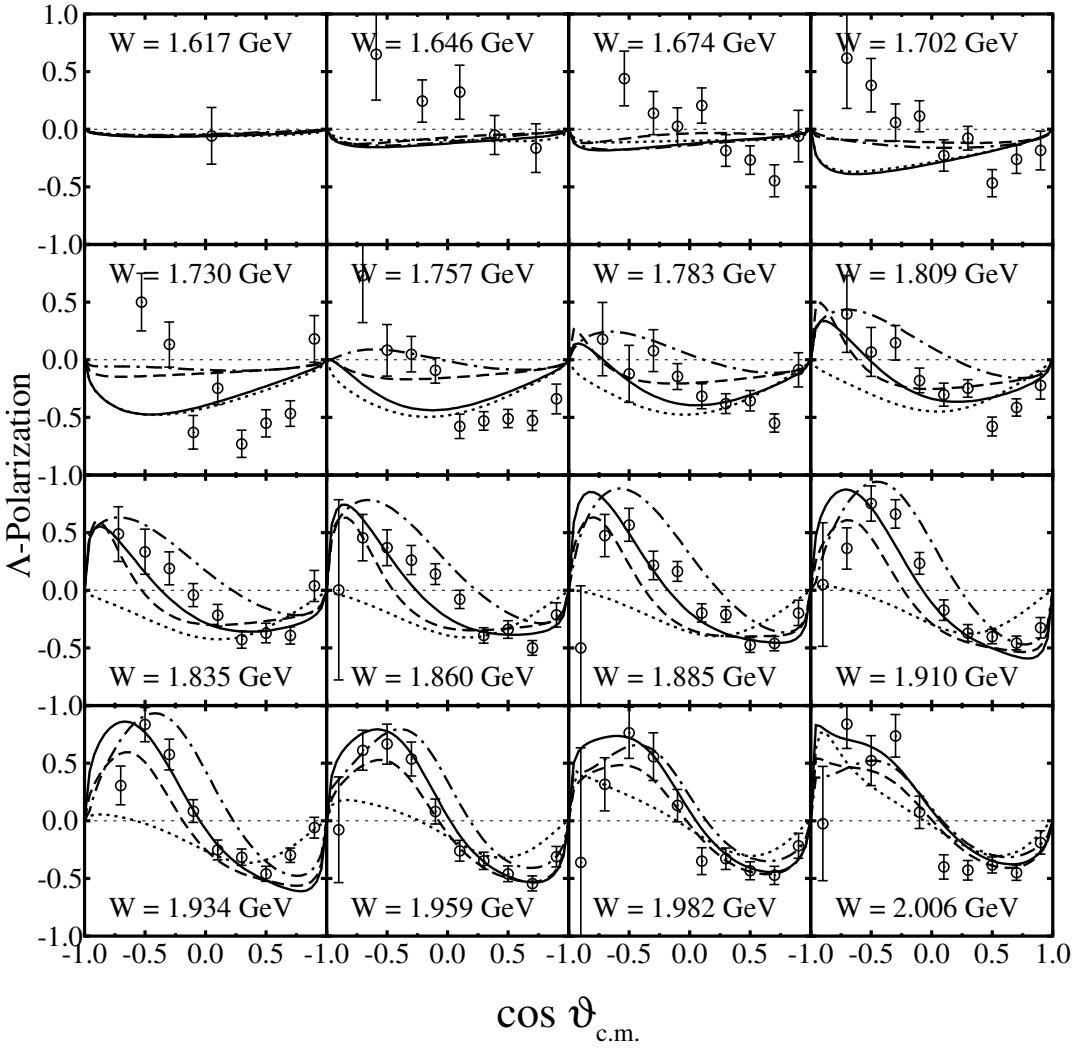

Figure 35: The recoil polarization P_y for $\gamma p \to K^+\Lambda$. The solid lines show the full calculation, while the dashed, dotted, and dot-dashed lines show the calculation without the $P_{13}(1720)$, $D_{13}(1900)$, and $P_{13}(1900)$ contributions. Data are from Ref. [28].

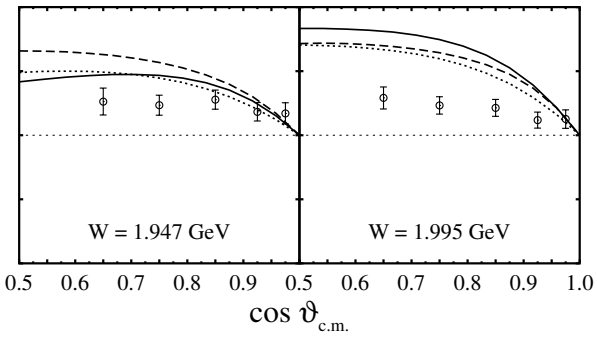

Figure 36: The photon beam asymmetry Σ for $\gamma p \to K^+\Lambda$. The solid lines show the full calculations, while the dashed and dotted lines show the calculation without the $D_{13}(1900)$ and $P_{13}(1900)$ contributions. Data are from Ref. [74].

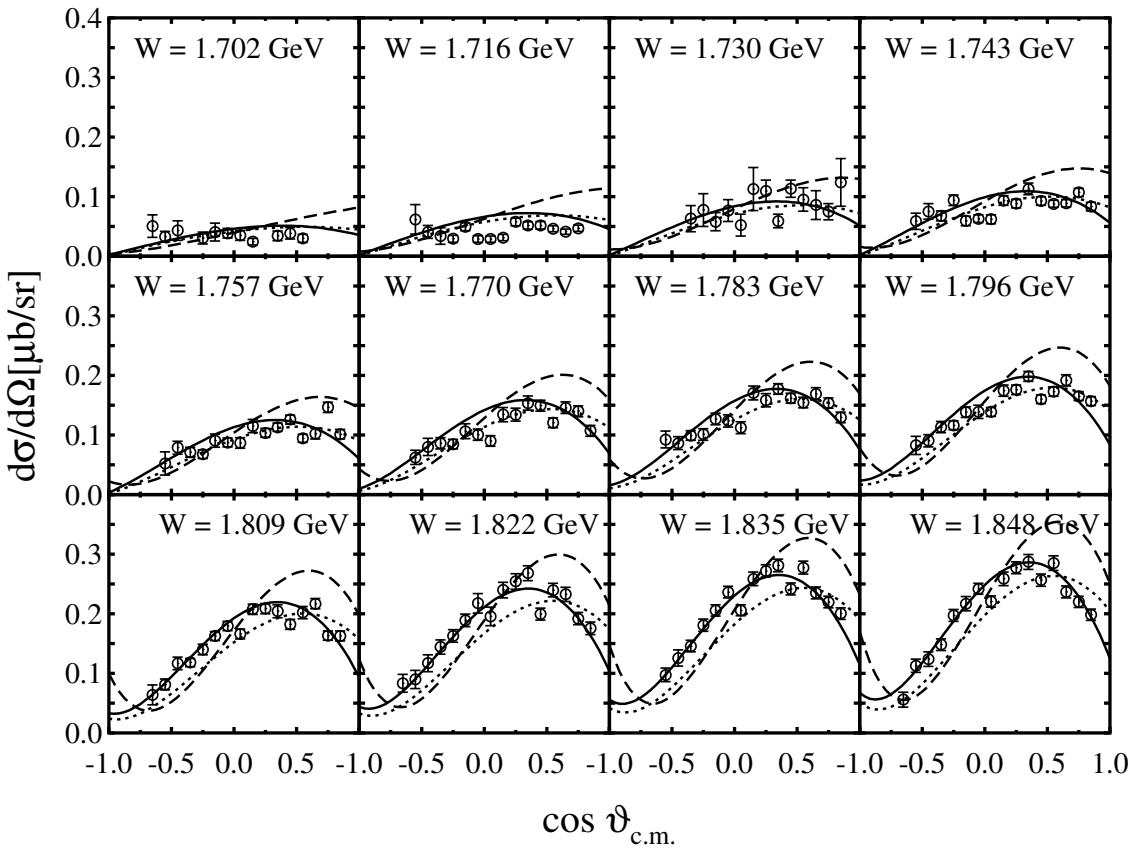

Figure 37: Differential cross sections for $\gamma p \to K^+\Sigma^0$ at low energies. The solid lines show the full calculation, while the dashed and dotted lines show calculations without the $D_{13}(1700)$ and $D_{33}(1700)$ contributions. Data are from Ref. [28].

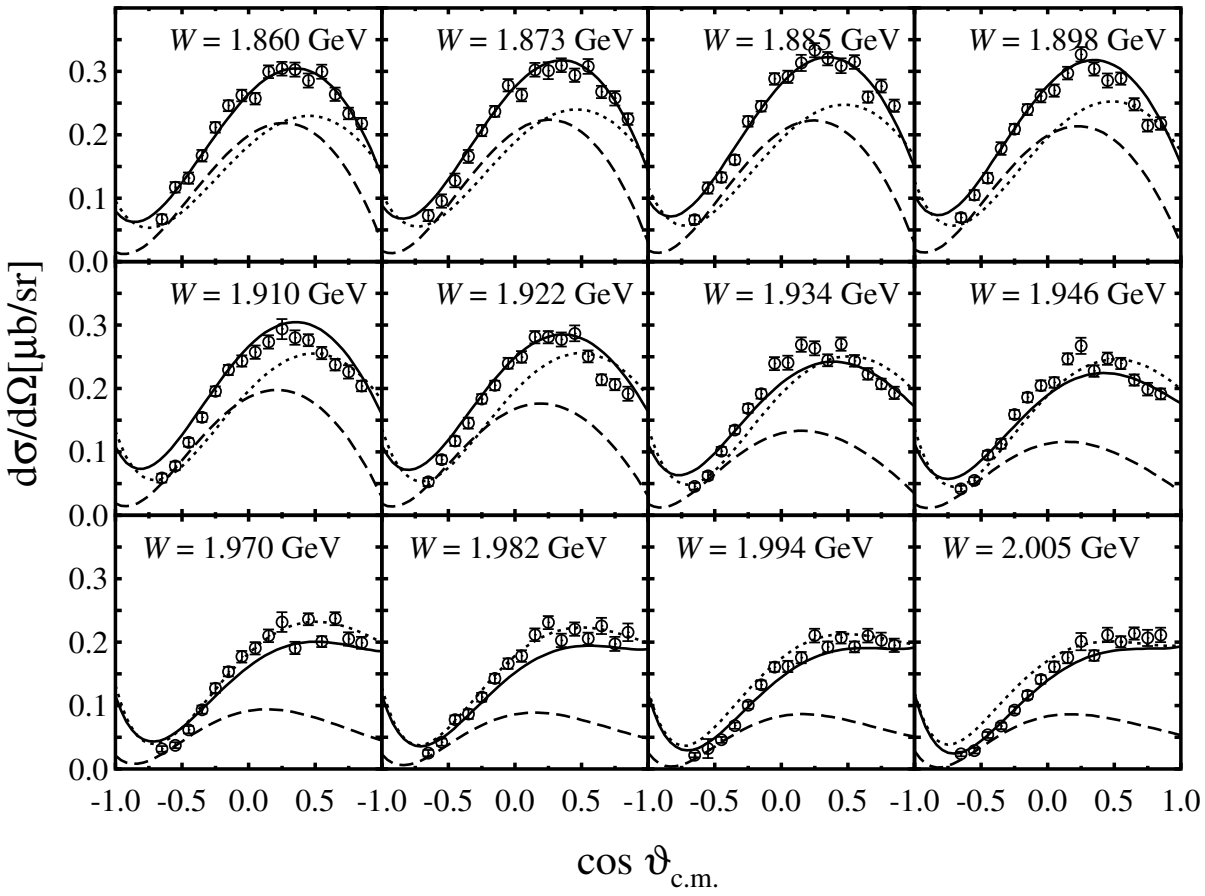

Figure 38: Differential cross sections for $\gamma p \to K^+\Sigma^0$ at higher energies. The solid lines show the full calculation, while the dashed and dotted lines show calculations without the $P_{31}(1900)$ and $P_{33}(1920)$ contributions. Data are from Ref. [28].

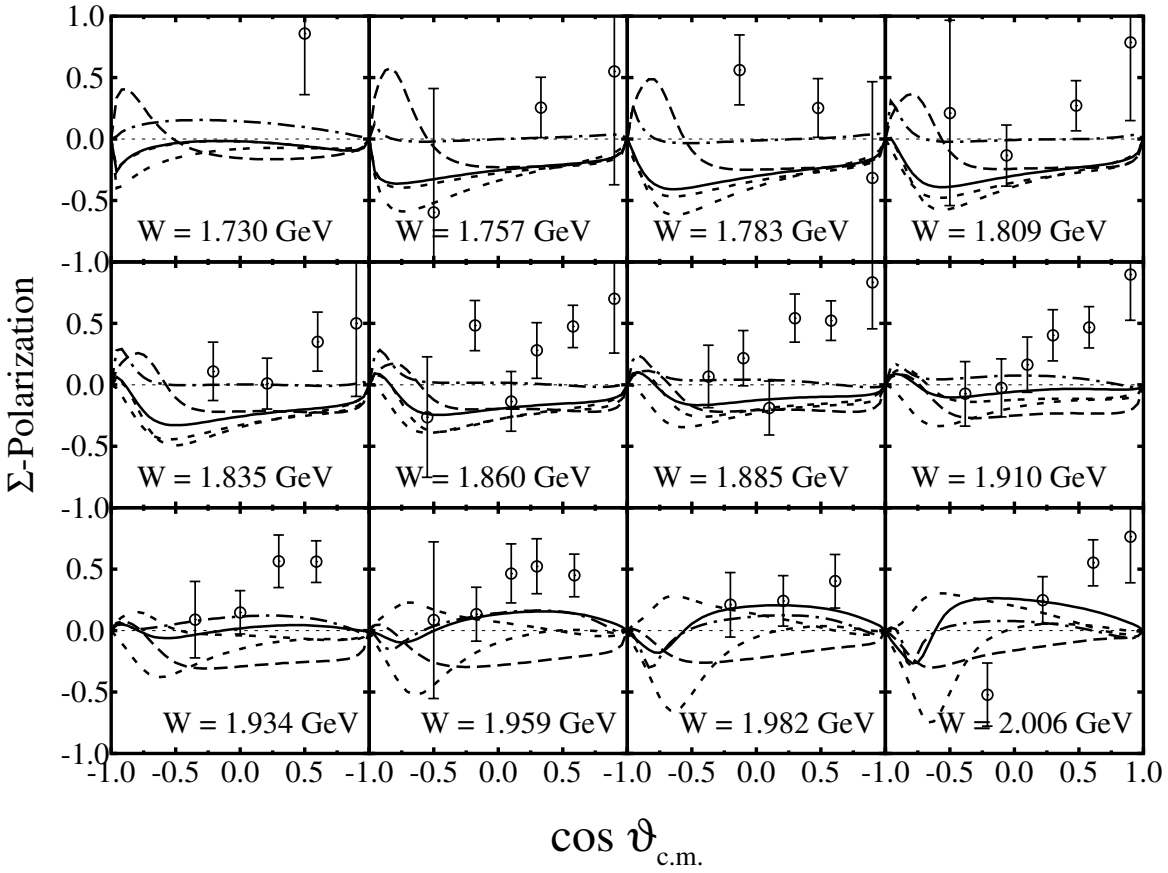

Figure 39: Σ^0 recoil polarization for $\gamma p \to K^+\Sigma^0$. The solid lines show the full calculation, while the dashed, dotted, dot-dashed, and double-dotted lines show calculations without the $D_{13}(1700)$, $S_{31}(1900)$, $P_{31}(1900)$, and $P_{33}(1920)$ contributions, respectively. Data are from Ref. [28].

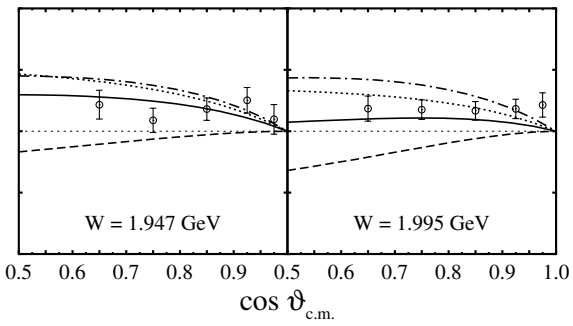

Figure 40: The photon beam asymmetry Σ for $\gamma p \to K^+\Sigma^0$. The solid lines show the full calculations, while the dashed, dotted, and dot-dashed lines show the calculation without the $D_{13}(1900)$, $P_{33}(1920)$, and $D_{35}(1930)$ contributions. Data are from Ref. [74].

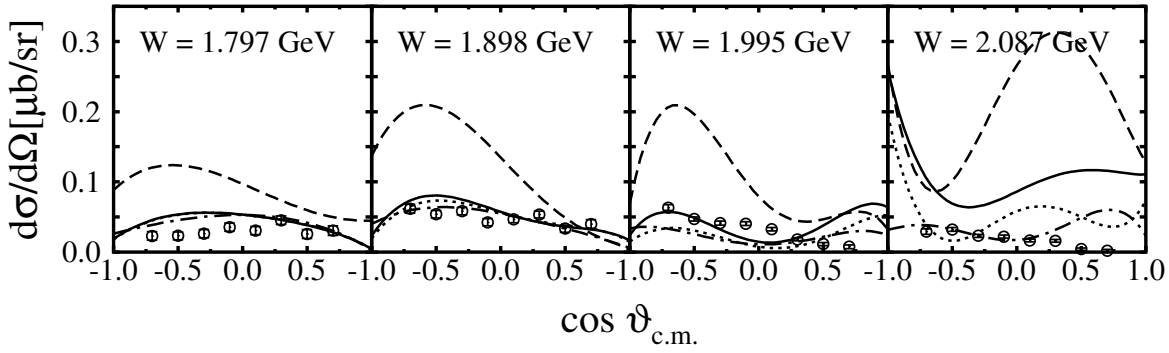

Figure 41: $\gamma p \to K^0\Sigma^+$ differential cross section at lower energies. The solid lines show the full calculation, while the dashed, dotted, and dot-dashed lines show the calculation without the $D_{13}(1700)$, $D_{35}(1900)$, and $D_{15}(2000)$ contributions. Data are from Ref. [55].

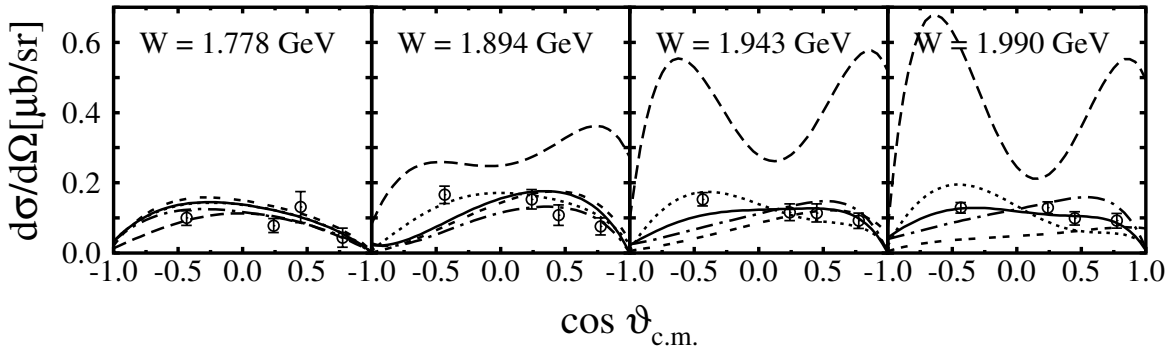

Figure 42: $\gamma n \to K^+\Sigma^-$ differential cross sections at higher energies [58]. The solid lines show the full calculations, while the dashed, dotted, dot-dashed, and double-dotted show the calculation without the $D_{13}(1700)$, $P_{31}(1900)$, $P_{33}(1920)$, and $D_{15}(2000)$ contributions.

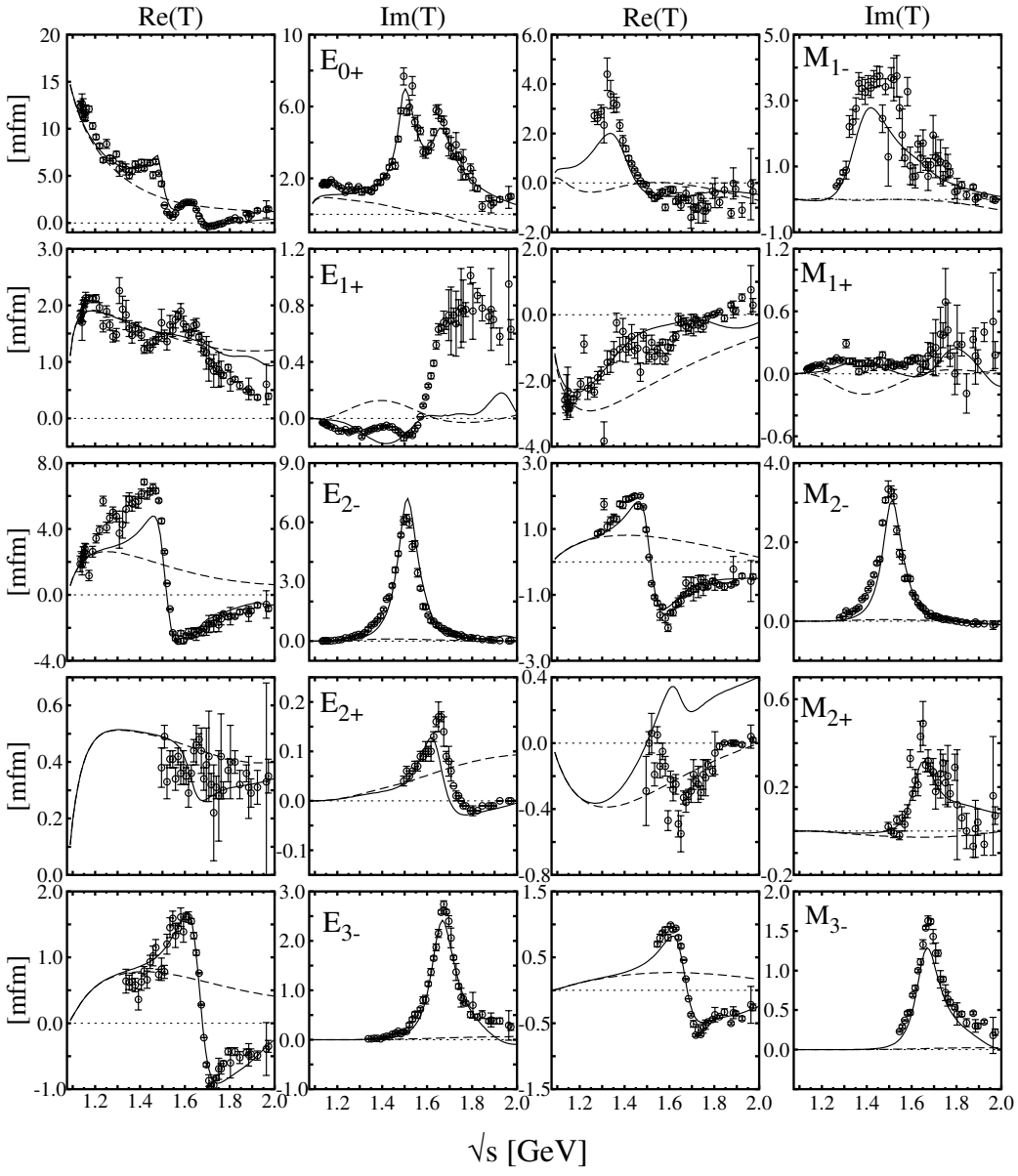

Figure 43: Pion photoproduction proton electric and magnetic multipoles resulting from global fits. Electric and magnetic multipole single-energy solutions are taken from GW-DAC. The solid lines show full solutions while the dashed lines show the background contribution.

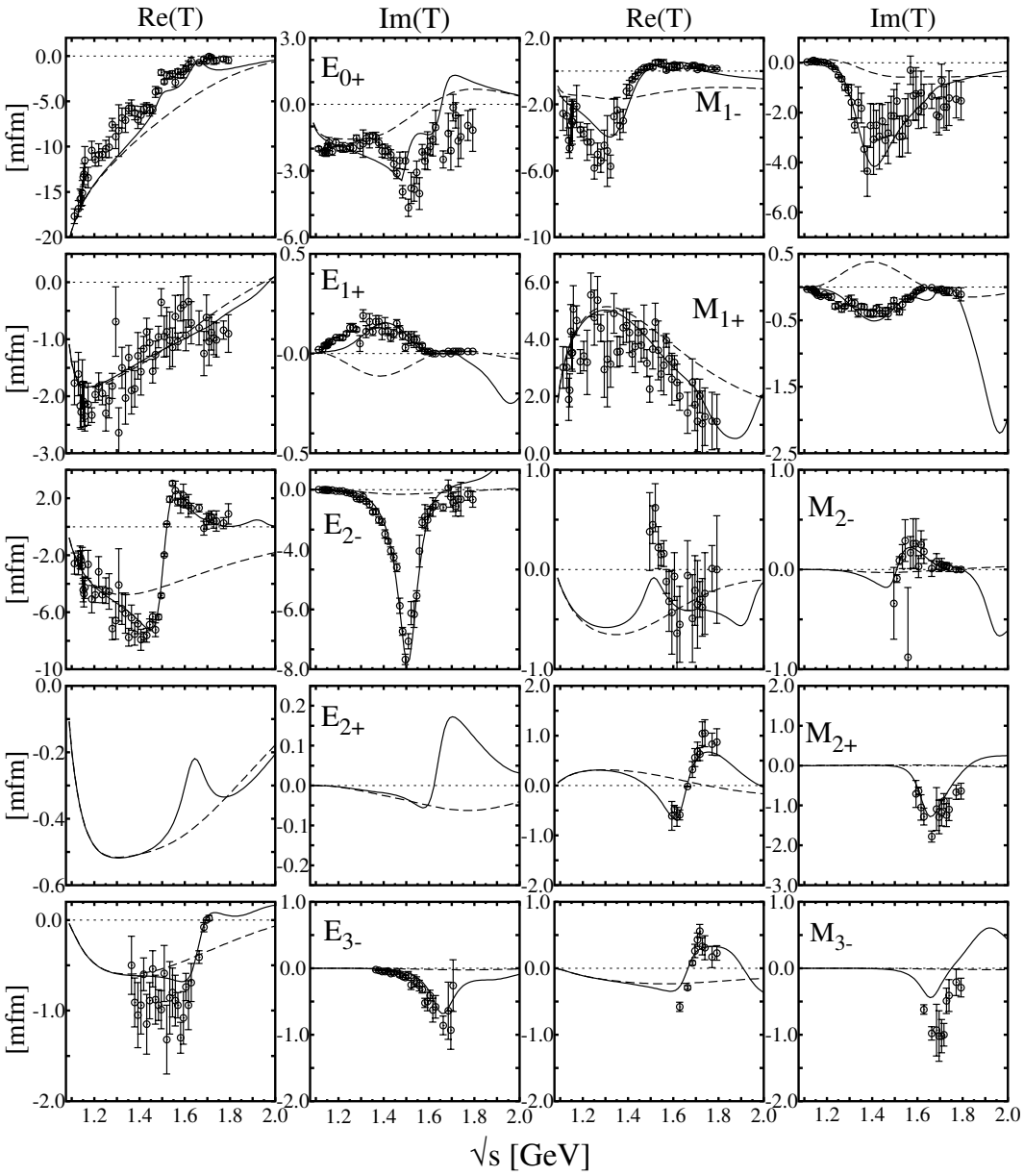

Figure 44: Pion photoproduction neutron electric and magnetic multipoles resulting from the global fits. The solid lines show full solutions while the dashed lines show the background contribution.